3-17-2023

Stellar Binaries and Post-Merger Evolution: A Framework for Stellar Evolution and Nucleosynthesis in R Coronae Borealis Stars

Bradley Munson
Louisiana State University and Agricultural and Mechanical College

STELLAR BINARIES AND POST-MERGER EVOLUTION: A FRAMEWORK FOR STELLAR EVOLUTION AND NUCLEOSYNTHESIS IN R CORONAE BOREALIS STARS

A Dissertation

Submitted to the Graduate Faculty of the
Louisiana State University and
Agricultural and Mechanical College
in partial fulfillment of the
requirements for the degree of
Doctor of Philosophy

in

The Department of Physics and Astronomy

by
Bradley Munson
B.S., North Central College, 2017
May 2023

ACKNOWLEDGMENTS

Contrary to what people outside the field may believe, science cannot be done in complete isolation and scientists will always perform at their best with supportive groups and collaborations.

That being said, I have a number of people I need to thank for being part of my supportive community. To start, a huge thank you to my committee members for attending my general exam and giving helpful feedback that furthered my research. A special thank you to my advisor, Manos Chatzopoulos, who also serves as a reminder that life does not consist of just schoolwork and research. Furthermore, a thank you to Juhan Frank and Geoff Clayton, who always seem to have valuable insight into the problem I am working on, whatever the problem may be. Catherine Diebel also deserves thanks for patiently explaining the nuclear physics aspects of my findings. Finally, I'd like to acknowledge the Department of Defense sponsored SMART program for funding most of my degree and guaranteeing a job out of graduate school.

Of course, my supportive community at school extends beyond just LSU professors. Thank you to Tyler Ellis, Robert Baker, Graeme Morgan, and Aaron Ryan for being friends early on while suffering core courses and organizing D&D nights. I will also always look fondly on bad movie nights with Alex Igl, nearly killing myself at the gym with Khang Pham, and being humiliated in chess with Arshag Danageozian. These friends helped me forget the less fun parts of graduate school and made me feel like it was (almost) a good time.

Before attending LSU for my graduate program, I had major influences that helped me get to where I am. Thank you to the entire physics department of North Central College which consisted of three professors: Paul Bloom, David Horner, and Stuart Wick. Paul Bloom, my undergraduate advisor, served as a seemingly bottomless pit of knowledge and assistance in my classes (even if he didn't teach them). I wouldn't have made it through some of the upper level physics classes without the companionship of Mike Maton, Alicia Casacchia, and Soja Enkhbat. We had some good late nights in the physics lab working on homework and eating tacos. Even before college, I was heavily influenced by my high school physics teacher, Paul Holder, who is probably the single biggest reason I even embarked on this journey. Our long conversations extended beyond just physics and he eventually became a friend to visit when I am in town.

I also have to thank my family who always seemed to know I'd get here even if I wasn't sure. Thank you to my mom for the support and helping me move out to Baton Rouge and hunt for apartments. Thank you to my dad for the weekly chess games and car advice (hopefully I won't need it with the new Honda...). Thank you to my brother for our occasional game nights that provided a distraction that was probably more necessary than you realize.

Finally, my biggest thank you to my wife, Lisa Munson. She has proofread all of my publications, including this one, despite not being in a science field! Frankly, she can probably explain my research as well as I can at this point. She also gives me endless support at home by dropping everything to help me through whatever struggle I may encounter. Her love for me is seconded only by her love for our cat, Luna, but I can't fault either of them for that.

TABLE OF CONTENTS

ABSTRACT

We have developed a framework for simulating binary stars through all three relevant timescales: the dynamical merger, thermal, and nuclear evolution. The framework begins by simulating a dynamical merger in a 3-dimensional hydrodynamics adaptive mesh refinement code, *Octo-Tiger*, and performing a spherical averaging calculation to map the post-merger remnant into the 1-dimensional stellar evolution code, *MESA*. In this work, we primarily utilize this framework for simulating double white dwarf mergers, which are believed to be the progenitor to R Coronae Borealis (RCB) stars. We evolve the post-merger in *MESA* and compare the computed surface abundances to those observed in RCB stars. We also post-process these models with *MPPNP* for heavy metal nucleosynthesis. Although we are not able to perfectly match observations with this framework, we are able to perform a parameter study by "engineering" a post-merger to perfectly reproduce the surface abundances of an RCB star. These models show that the large neutron density required for neutron capture reactions may actually be characteristic of the i-process rather than the s-process, which was thought to be active in RCB stars. We further extend the framework by simulating the merger of a giant and main sequence star, which is a possible progenitor for Betelgeuse. Although we are only able to reproduce the high rotation rate of Betelgeuse by suppressing angular momentum diffusion, we note that the extension of this framework represents a necessary step to perform holistic studies of mergers consisting of compact, main sequence and/or giant stars.

CHAPTER 1.
INTRODUCTION

1.1 Binary Systems

Astronomers have known about the existence of binary stars for over 300 years. In fact, the majority of stars in the night sky are actually systems with two or more stars. These systems are important as we can get insight into some properties that would not be easily attainable by single star systems. For instance, Kepler's laws allow us to use their orbital dynamics to estimate their masses, something that is not possible with a single star. In some cases, a binary system may lose angular momentum through stellar winds or gravitational radiation, causing a collision that creates phenomena that can be observed through their lightcurves or spectra.

In order to understand how these systems merge, it is important to understand some basic concepts involved in binary systems. The first concept to understand is the Roche potential shown in Equation 1.1.

$$\Phi(\vec{r}) = -\frac{GM_1}{|\vec{r} - \vec{r_1}|} - \frac{GM_2}{|\vec{r} - \vec{r_2}|} - \frac{1}{2}(\vec{\omega} \times \vec{r})^2 \tag{1.1}$$

This potential term is taken in the co-rotating frame which rotates at the orbital angular velocity $\vec{\omega}$. G is the gravitational constant, M_i is the mass of star i, and $\vec{r_i}$ is the position of star i. It is typical to refer to the accretor (the star gaining mass) as star 1 and the donor (the star losing mass) as star 2. In this frame, the two stars are static and thus the potential requires the extra centrifugal component seen in the last term of Equation 1.1.

An illustration of this equation is shown in Figure 1.1. In this figure, we can see the two sources of gravitational potential causing the potential wells in the middle. Those potential wells are due to the first two terms of Equation 1.1 and the downward curvature at the edges of the surface is due to the last term.

Another way to illustrate the Roche potential is with a contour plot with lines of equipotential. This is shown in Figure 1.2 with the same parameters used to create Figure 1.1.

Figure 1.2 more clearly shows the Roche lobe radius, R_L, with the bold figure eight line around stars 1 and 2. The Roche lobe radius is the average radius within which material will be bound to its star. Therefore, if a stellar radius were to expand beyond its Roche lobe radius, material would then either fall into the potential of the other star or become unbound from the system through the centrifugal force. Once the Roche lobe radius is smaller than the stellar radius, that star will begin to lose mass and decrease its Roche lobe radius even further. Depending on the response of the stellar radius to mass loss, this may result in a rapid and violent process of mass transfer.

1.2 Double White Dwarfs

When on the main sequence, stars generate their energy via nuclear fusion. This process begins by fusing hydrogen atoms into helium and, depending on the mass of the star, can progress to fusing heavier elements resulting in a dense core rich with metals. However, once

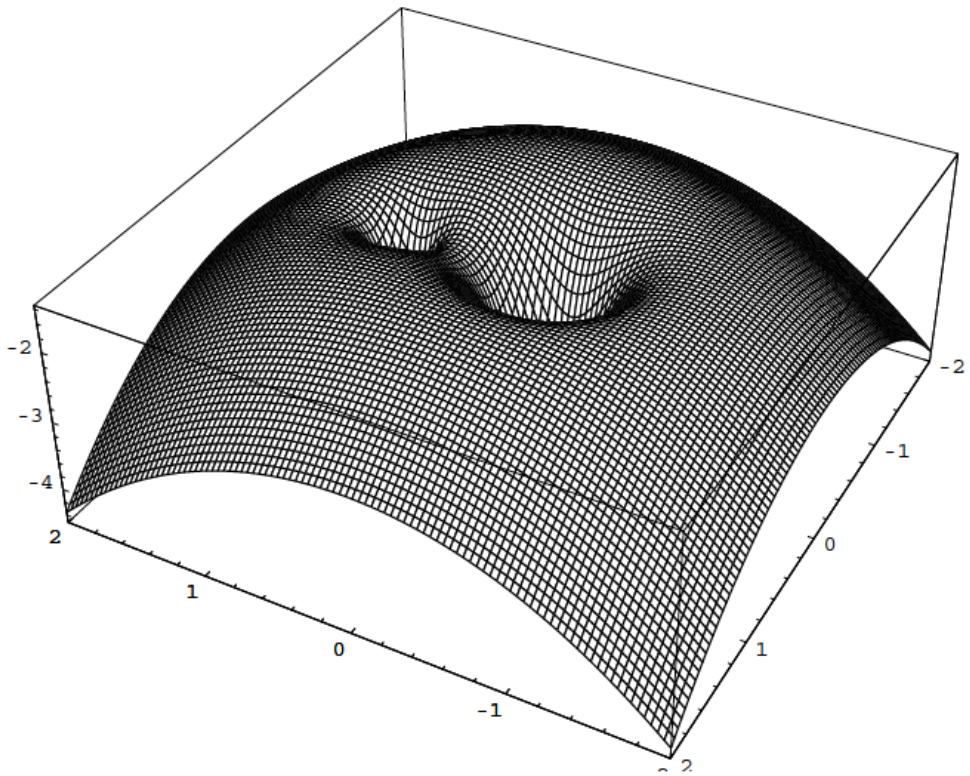

Figure 1.1. This figure shows a surface plot of the Roche potential (Equation 1.1) of a binary with a mass ratio ($q = \frac{M_2}{M_1}$) of 0.25. The two dips in the surface are due to the two stars with the larger dip corresponding to the more massive star. The downward curvature at the edges of the plot is due to the centrifugal term. This means a test mass far enough away from the stars will experience a net outward force. *Source*: Frank et al. (2002)

iron is formed in the core, nuclear fusion becomes endothermic (requiring more energy to fuse than is released) and nuclear fusion will cease. After nuclear fusion ceases in the core, the outer envelopes may be ejected via stellar winds or interaction with a companion in a binary system, leaving behind the dense inert core which is referred to as a white dwarf (WD).

For a binary system containing two main sequence stars, one likely outcome is the system comes into contact or becomes semi-detached. This happens because the more massive of the two stars evolves more quickly than its companion and fills its Roche-Lobe while expanding as a red giant, thus initiating mass transfer onto the less massive star. After losing much of its mass in the envelope, the original donor becomes a white dwarf leaving behind a system with a white dwarf and a main sequence star. Eventually, the main sequence star will also evolve as a red giant, fill its Roche-Lobe, and transfer mass onto the White Dwarf. This system is known as a cataclysmic variable (CV) and it can eventually evolve to a Double White Dwarf (DWD) system after the red giant sheds its envelope.

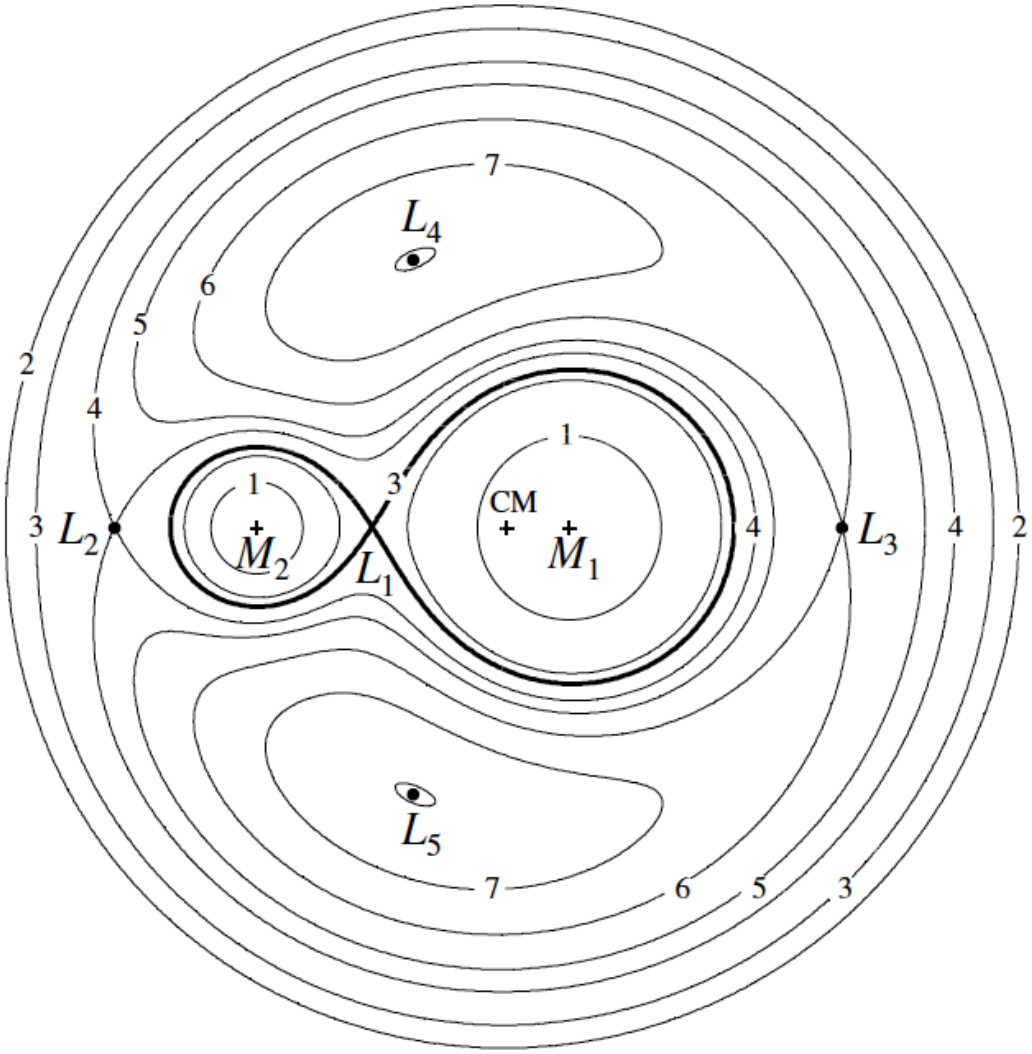

Figure 1.2. The parameters in this plot are the same as described in Figure 1.1. In this figure, the Lagrangian points are identified and lines of equipotential are numbered in order of increasing Roche potential. The bold line indicated by number 3 illustrate the Roche Lobes. *Source*: Frank et al. (2002)

Depending on the total mass and mass ratio, there can be a variety of different outcomes for the resulting DWD binary system, including explosive transient phenomena, single neutron stars, and giant stars. One specific outcome for such systems is the formation of an exotic class of stars called R Coronae Borealis stars.

1.3 RCB Stars

R Coronae Borealis (R CrB or RCB) is one of the first discovered and studied variable stars. This star is located in the constellation Coronae Borealis and was given the designation "R" to represent the first discovered variable star of the constellation. Pigott & Englefield (1797)

first started monitoring the brightness upon noticing the disappearance of RCB from the naked eye. This makes RCB (the namesake for the classification) one of the longest studied variable stars on record.

RCB stars are rare hydrogen-deficient, carbon-rich, yellow supergiants (Clayton, 2012, 1996). Their variability of up to 8 magnitudes was determined to be caused by thick irregular clouds of carbon dust obscuring our line of sight (Loreta, 1935; O'Keefe, 1939). There are currently about 150 observed RCB stars with more candidates that have yet to be verified. The surface abundances of RCB stars are not only extremely helium-rich and hydrogen-deficient, but also contain an enrichment in N, Al, Na, Si, S, Ni, and several s-process elements (Asplund et al., 2000). Furthermore, RCB stars show extraordinarily low $^{16}O/^{18}O$ (on the order of unity) and large $^{12}C/^{13}C$, which, along with the enrichment of s-process elements, are consistent with partial He-burning (Clayton et al., 2007). Finally, most RCB stars have a metallicity of about 0.1 $Z_{\odot}$ (Asplund et al., 2000).

There have been two main evolution channels proposed for the creation of RCB stars. First, the final Helium-shell flash model is proposed to be a late thermal pulse in a post-AGB[1] star (Fujimoto, 1977). Second, the double white dwarf (WD) merger scenario is a merger event between a lower mass Helium (He) WD and a higher mass carbon-oxygen (CO) WD (Webbink, 1984). In the final He-shell flash model, there is no predicted mechanism for producing a sufficient amount of ^{18}O to match the level of ^{16}O. However, in the double WD merger model, partial He-burning would allow for the necessary enhancement of ^{18}O (Clayton et al., 2007). Because this is an important feature for RCB stars, the double WD merger model is often considered the dominant channel for the formation of RCB stars, although it is possible they can be formed in more than one way.

Figure 1.3 shows a cartoon schematic illustrating the important phases of the formation process for RCB evolution. The first phase is the dynamical merger when the He-WD experiences Roche lobe overflow (RLOF) and becomes tidally disrupted. The result of this phase is a toroidal shaped post-merger object with a hot He-burning shell above the CO WD. The shape is due to the orbital angular momentum left over from the binary. The second phase is a viscous phase which should take a few hours to settle the post-merger object to a spherical geometry with a radius around a tenth of a solar radius. The third phase is a thermal expansion that takes place over thousands of years as the spherical post-merger object begins to expand up to a few hundred solar radii due to the input energy from the He burning shell and synthesized material from the shell is mixed throughout the envelope due to convective mixing. Finally, the object enters the RCB phase in which stellar winds push carbon dust that obscures our line of sight and causes the irregular declines of around 8 magnitudes.

RCB stars are suspected to be the result of a dynamically unstable double WD merger between a high mass CO WD (M_1) and a lower mass He-WD (M_2) (Webbink, 1984). Because the merger event must be dynamically unstable, there is a constraint on the mass ratio ($q = \frac{M_2}{M_1}$) for DWD binaries requiring it to be greater than 2/3 (the derivation can be found in Appendix 5.3).

There are, however, many more layers of complications to consider, such as mass loss from the entire system (which should be minimal), spin-orbit coupling, and the effects of M_2 either

[1]Asymptotic Giant Branch

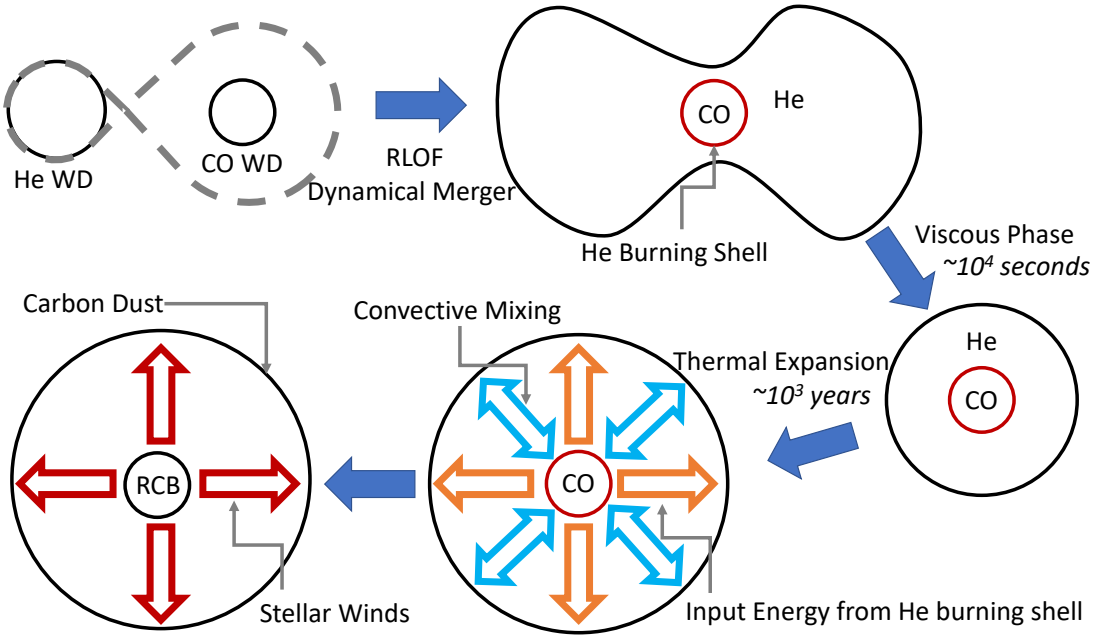

Figure 1.3. A simple schematic outlining the important evolutionary phases of the RCB progenitor. Note that the individual phases are not accurate to any length scale.

forming a disk structure around M_1 or the stream having a direct impact on the surface of M_1. These considerations will have dramatic effects on the change in orbital angular momentum and will therefore change the constraints required to make the merger dynamically unstable. Dan et al. (2011) resolve some of those complications with numerical models and illustrate which mass configurations will have a dynamically unstable mass transfer in Figure 1.4. When those additional considerations are made, the mass ratio can be pushed as low as 0.25 for certain mass configurations. For $q > 1$, M_2 would plunge into M_1 and would not become tidally disrupted before mass transfer had begun.

The second requirement in the formation process for RCB stars is the presence of a He-burning region. As mentioned in the beginning of this section, the surface abundance of RCB stars shows evidence of partial He-burning. Previous models have shown that increasing the total mass of the system and decreasing the mass ratio will increase the temperature of the He-burning region, which can also be referred to as the shell of fire (SoF) (Staff et al., 2012). This region will form after the merger event as the material from the He WD crashes onto the surface of the CO WD and becomes shock heated.

Most helium capture reactions, including the important neutron source $^{13}\mathrm{C}(\alpha, n)^{16}\mathrm{O}$, will be active above 100 MK (Käppeler et al., 2011). Neutron source reactions are important for the enhancement in s-process elements that are observed in RCB stars. Taking into account these constraints as well as the requirement for a dynamically unstable merger, we find that total masses and mass ratios of 0.7-1.0$M_\odot$ and 0.5-0.6 are sufficient, respectively. Furthermore, since the nucleosynthesis happens right above the interface of the CO and He WD, there needs to be some mechanism for mixing to get the synthesized material from the burning region to the surface within the time it takes the post-merger object to get to the RCB phase.

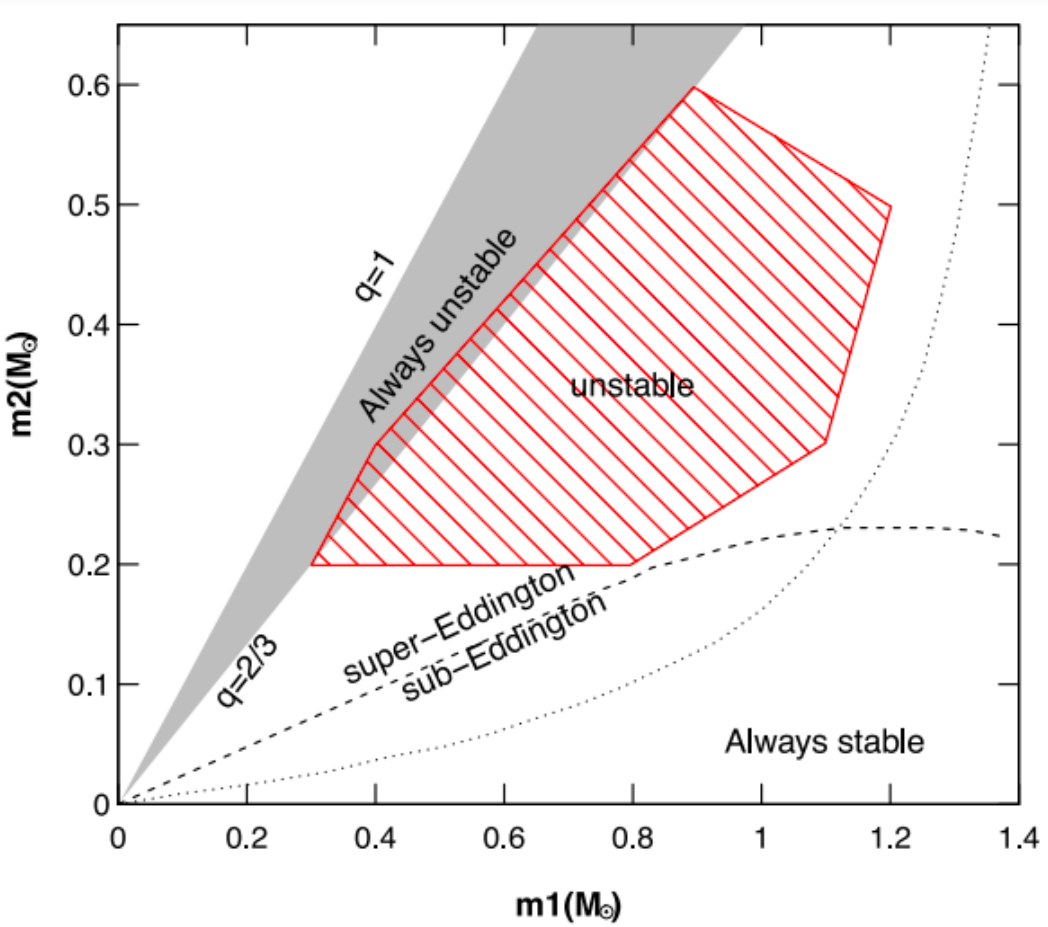

Figure 1.4. This plot shows for a space of mass configurations, M_1 and M_2, which will commence unstable mass transfer. The hatched region specifically comes from models in Dan et al. (2011). *Source*: Zhang et al. (2014)

1.4 Literature Review

In this section, we review the literature of previous modeling attempts for RCB stars. In general, previous models can be put in one of three different categories: modified He star evolution, stellar engineering, and 3D to 1D mapping. Each of these methods has advantages and disadvantages that will be discussed throughout this section. The first two methods attempt to mimic the post-merger structure through methods that are not necessarily related to the merger event. The structure is guided by previous 3D hydro methods (Staff et al., 2012) and should generally consist of a cool degenerate CO core, a hot He burning shell, and an envelope with a composition resulting from the He WD.

Some of the features of each model mentioned in this section are illustrated in Figure 1.5. In this figure, the upper left diagram shows the density profile, the upper right diagram shows the Hertzsprung Russel diagram (HR diagram or HRD), the lower left shows the temperature profile, and the lower right shows the temperature density profile as well as density and temperature requirements for He-burning, C-burning, and electron degeneracy.

In these panels, q is the normalized interior mass coordinate $\left(\frac{M_r}{M_{tot}}\right)$ which is a mass fraction that will be 1 at the surface (when all of the mass is interior to that coordinate) and 0 at the core (when all of the mass is exterior to that coordinate). M_r refers to the amount of mass interior to a shell of radius r.

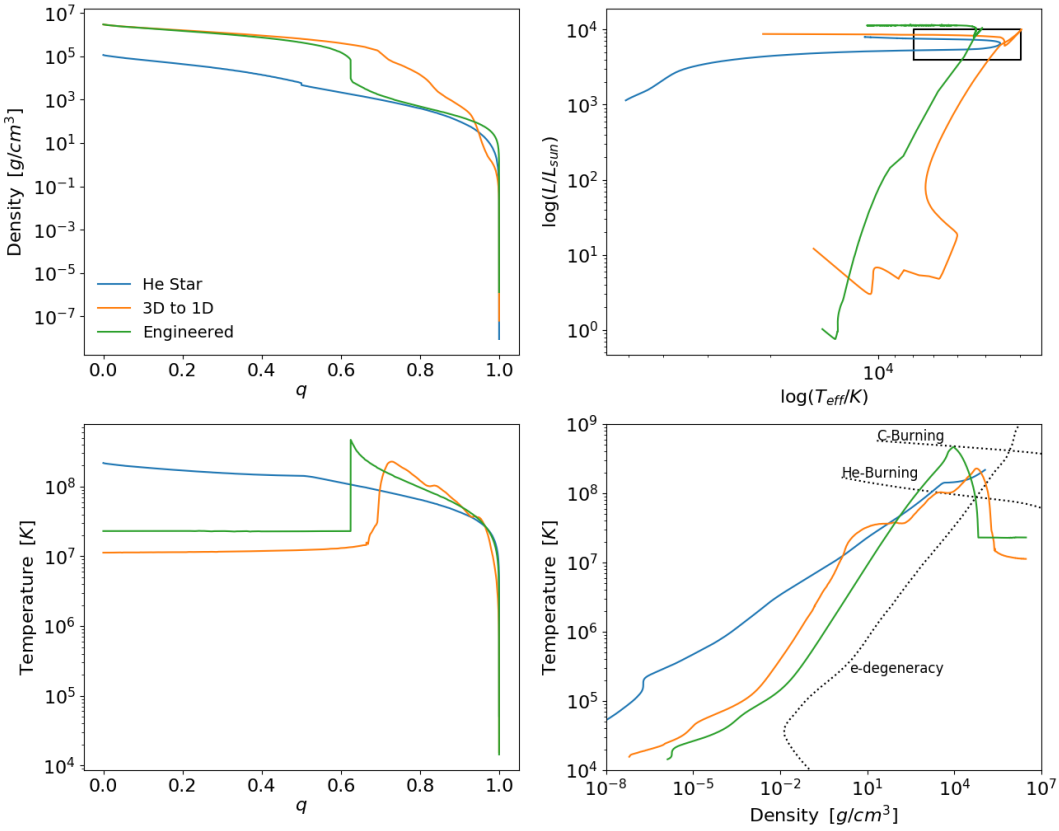

Figure 1.5. A four panel figure comparing the different models when He shell burning begins. The blue line refers to the modified helium star evolution ($0.53M_\odot$ CO + $0.37M_\odot$ He WD) (Menon et al., 2013), the orange line refers to the 3D models mapped into 1D ($0.53M_\odot$ CO + $0.27M_\odot$ He WD) (Munson et al., 2021), and the green line refers to the models created by stellar engineering ($0.55M_\odot$ CO + $0.33M_\odot$ He WD) (Lauer et al., 2019). The upper left panel shows the density profile, the upper right shows the HR Diagram, the lower left shows the temperature profile, and the lower right shows the temperature-density profile. The HR diagram on the upper right contains a black box representing the range of observed surface temperatures and luminosities of RCB stars.

The modified He star evolution model is employed in works such as Weiss (1987) and Menon et al. (2013, 2019). This method is a straightforward and fast way to create an RCB model. This model is initialized with a helium zero-age main-sequence (ZAMS) star

and after the envelope has shrunk to some predetermined mass, a user-defined composition motivated from progenitor models is imposed on the envelope. In Menon et al. (2013, 2019) the abundance profile is split into four separate zones. Those zones are the core, a buffer region to prevent dredge up from the core, the He-burning region, and the envelope. Initializing the He burning region separately from the envelope is a sophistication that allows one to consider the effects of burning during the dynamical merger. This model provides a CO core consistent with core He-burning underneath a He-burning shell and an envelope with the expected composition from the He-WD.

One disadvantage of this modeling approach is that the thermal state of the core is not in agreement with what would be realized in a WD merger scenario. This disagreement will have effects on the evolution and state of the envelope (Iben, 1990). In the WD merger scenario, one should expect the CO WD that would form the core of the RCB to be cooler and more degenerate than the CO core that would form from core He-burning. Instead, this model sees phases of H shell burning and expansion before the shell temperature can become high enough to begin He shell burning. Once He shell burning has begun, the envelope has already expanded a couple hundred times the size of the post-merger object. Therefore, the evolution of the RCB from that point looks significantly different than the other two methods as seen in the upper right panel of Figure 1.5. Also, because the star has already expanded by the time the shell is hot enough to commence He shell burning, the temperature gradient is not sufficient to cause convective mixing. Menon et al. (2013) see this in their models and instead require a secular mixing model be adopted to account for the required envelope mixing and justify that the additional mixing may be induced by rotation. However, because the surfaces of RCB stars show evidence of partial He-burning, this mixing profile must be ceased before the object reaches the RCB phase. This is done by creating a function for an additional diffusion coefficient dependent on the mass coordinate, density, temperature and stellar age.

Menon et al. (2013, 2019) conduct studies of solar and sub-solar metallicities, respectively. This is important as RCB stars are characteristically lower in metallicity and this will have an effect on the final surface abundances. These studies take extra care to analyze the nucleosynthesis responsible for the overabundance in ^{18}O and ^{19}F. They find that they are only able to reproduce the surface abundances with the secular mixing profile mentioned above. This must mix material not so fast as to destroy all of the ^{18}O but fast enough to bring ^{15}N to the burning region in order to form ^{19}F. Furthermore, this additional diffusion coefficient must halt before the RCB phase in order to maintain the surface ^{14}N abundance. Their study also uses post-processing with over 1000 isotopes and investigates s-process elements but finds only lower mass ratios (q=0.5) have a neutron number density high enough to produce s-process element enhancement.

Stellar engineering is a general term used to describe any ad-hoc change to the numerical model that is not implemented through a physical process in order to construct a stellar model that matches some expected initial structure. Zhang et al. (2014) utilize stellar engineering in Modules for Experiments in Stellar Astrophysics (*MESA*) (Paxton et al., 2011, 2013, 2015, 2018, 2019) to create an RCB by starting with a $3.0 M_{\odot}$ main-sequence star and letting it evolve to a CO WD. After the core reached a predetermined mass, the envelope was removed and a fast accretion phase was used to mimic a hot corona. Then, a slow accretion phase was used to mimic a cool Keplerian disc. The accreted material compositional fractions were

assumed to be 0.98 He and 0.02 metals where the metals distribution is obtained from a He WD model. However, *MESA* no longer supports fast and slow mass accretion so we do not explore this modeling procedure further.

Another way to use stellar engineering to create RCB stars is discussed in great detail in Lauer et al. (2019) and Crawford et al. (2020). In summary, first a CO and He WD are created from main-sequence stars in order to obtain a composition for the core and envelope of the RCB. Then, a post-merger object with a mass of two components combined is created and the core is allowed to cool until a degeneracy parameter is met. The CO WD composition is imposed up to a mass coordinate equal to the CO WD mass and the He WD composition is imposed on the remaining portion of the post-merger object. Finally, in order to get He shell burning temperatures, a process of entropy adjustment as described in Shen et al. (2012) is employed until a post-merger radius of about $0.1 R_{\odot}$ is reached. This is done by utilizing a *MESA* routine to add extra heat (Q) to the shells of the post-merger object at each timestep. The form of the added heat is the following:

$$Q(M_r) = \begin{cases} (S_{low} - S(M_r))\frac{T(M_r)}{t_{rel}}, & M_r \leq M_{core} \wedge \eta \leq \eta_{transition} \\ (T_{core} - T(M_r))\frac{S(M_r)}{t_{rel}}, & M_r \leq M_{core} \wedge \eta > \eta_{transition} \\ (S_{high} - S(M_r))\frac{T(M_r)}{t_{rel}}, & M_r > M_{core} \end{cases} \tag{1.2}$$

In this expression, S is the entropy, T is the temperature, t_{rel} is a user-defined timescale over which to add this heat, η is a degeneracy parameter, and M_r is the mass coordinate of a given shell. Using this function, one creates an entropy profile that looks like a step-function with a high entropy envelope and low entropy core while ensuring that the degenerate CO core remains isothermal. The result in terms of temperature can be seen in the lower two panels of Figure 1.5.

This initialization method creates a more physically motivated structure than the modified He star evolution method. The object is compact during He shell burning which allows for convective mixing throughout the envelope. However, as the envelope expands from the input energy from the He-burning shell, the mixing region breaks into two sections separated by a non-mixing shell and allows for only partially burned material to rise to the surface. Lauer et al. (2019) and Crawford et al. (2020) see a good match to observed RCB surface abundances without employing additional mixing coefficients and just allowing convection to be the primary mixing mechanism.

One shortcoming of these works is the simplistic initial abundance profile. Without having multiple zones similar to Menon et al. (2013), these models contain no mechanism to include results of nuclear burning during the merger phase. Instead, these models aim to create the spherical post-merger object directly from the compositions of the CO and He WD. Furthermore, authors who have utilized this method have not done an analysis of s-process nucleosynthesis. Lauer et al. (2019) and Crawford et al. (2020) use the `mesa_75` nuclear network, a co-processed nuclear network that contains the most important reactions for energy generation and includes elements up to ^{60}Zn. While this network does include neutrons, it does not include the heavy elements involved in the s-process and there is no analysis of the neutron number density being high enough for s-process nucleosynthesis.

Lauer et al. (2019) use models with solar metallicities, which do not match RCB observations, but they still obtain results that resemble RCB abundances. Crawford et al.

(2020) create models with both solar and sub-solar metallicities and see good agreement with RCB observations. They also perform a study of the surface abundance dependence on temperature by changing S_{high} in Equation 1.2. This will change the peak temperature in the He burning region which changes the nucleosynthesis and thus the surface abundance during the RCB phase. They observe that if the He burning temperature is too high, most of the ^{14}N and ^{18}O is destroyed and the surface abundances do not match observed RCB stars. However, if the temperature is too low, then not enough ^{18}O or ^{19}F is created and those elements do not match RCB surface abundances. Their study finds a shell burning temperature around 300 MK for these models is ideal for reproducing most of the observed abundances in RCB stars. These results are subject to change as modeling becomes more sophisticated in terms of the initial abundances or entropy profiles.

The final model to be discussed is perhaps the most physically representative of a merger event; the 3D hydrodynamics model mapped into 1D. One immediate concern with this method is the difference in equation of state (EoS) between differing codes. The EoS will determine the thermal properties of the star given a density, composition, and boundary conditions. However, given the same density profile in two different codes that use a different EoS, they will compute different temperature, pressure, and energy profiles. *MESA* uses a very sophisticated EoS table that takes into account the conditions of each zone and uses the best suited EoS or interpolates between two that are both well-suited. However, since 3D hydrodynamics models are already computationally expensive, it is typically more practical to use just one well suited EoS or a combination of two EoS's for the entire star.

Dan et al. (2011) create 3D models with a hybrid approach using the Smooth Particle Hydrodynamics (SPH) method for orbital evolution and the Adaptive Mesh Refinement (AMR) method for the evolution of the low density He material. Then, Schwab et al. (2012) use the models of Dan et al. (2011) to initialize a 2D model that simulates the viscous phase along the radial and polar directions. In their work, they find that the post-merger object becomes spherical on the order of a few hours with a simple prescription for shear viscosity. These models also include a basic five species nuclear network, a Helmholtz EoS (Timmes & Swesty, 2000) and a simple mechanism for mixing. Using the Helmholtz EoS provides the best match for the majority of regions in the post-merger object to the *MESA* EoS table. Finally, Schwab (2019) takes the spherical results from Schwab et al. (2012) and evolves the objects through the RCB phase in *MESA* and analyzes those models.

Schwab (2019) analyzes all three types of models, but notably sees a similar evolution to the 3D model we present in the HR diagram of Figure 1.5. That is, unlike the He star model, the post-merger object approaches the RCB phase from the bottom of the box instead of the left side. This is again because the post-merger object is much more compact when He burning is initiated and the envelope responds to this input energy with an initial thermal expansion and brightening phase. A strong aspect of the Schwab (2019) model is that it is not directly imported from 3D to 1D. Allowing the post-merger object to spherize in 2D using physical viscosity processes reduces any errors introduced by spherically averaging a non-spherical object into a 1D code like *MESA*.

Schwab (2019) does not focus on an analysis of the surface abundance or nuclear burning leading to the RCB phase. This is likely because of the insufficient nuclear network used in the 2D models, which is necessarily used to run the models in a practical amount of time. However, this work does stress the importance of an adjusted opacity table. The default

opacity tables used in *MESA* are not well suited for following the evolutionary tracks of RCB stars. This is because the default opacity table in *MESA* is calculated using GS98 (Grevesse & Sauval, 1998) solar scaled abundances. As noted earlier, the surfaces of RCB stars are extraordinarily hydrogen poor and He rich and also contain enhancements in C, N, O, F, and s-process elements. Although *MESA* does include opacity tables for carbon and oxygen-rich mixtures, referred to as "Type 2" tables, the lower temperature boundary for those tables is $\log(T/K) = 3.75$. This will not be consistent with RCB stars that develop cooler envelopes because the outer layers are hydrogen deficient and carbon and oxygen enhanced. This has an effect on the effective temperature and radius during the RCB phase, but does not appear to have a noticeable effect on surface composition.

Another study that directly utilized 3D hydro simulations is Longland et al. (2011). However, they did not actually simulate the evolution of the post-merger itself, but rather post-processed a 3D SPH model done in previous studies (Guerrero et al., 2004; Lorén-Aguilar et al., 2009, 2010) with a more sophisticated nuclear network in order to reproduce the unique surface abundances observed in RCB stars. The studies conducted on the 3D merger models had implemented a simple 14 isotope nuclear network to account for the energy generation; therefore, the post-processed nuclear network had only very minor differences in energy production. However, they do not expect to reproduce the enhanced s-process elements observed in RCB stars. Two different modes of mixing were explored in this study, shallow and deep mixing, where the former only extends partially from the surface into the He-rich envelope and the latter extends throughout the entire envelope. Each mode of mixing is analyzed with both an initial solar and sub-solar metallicity. In this study, they were able to reproduce an overabundance of ^{19}F, but not as high as observations suggest it should be. They were also able to produce a $^{16}O/^{18}O$ of 19, which is significantly lower than solar values, but not quite as low as is observed in RCBs. Overall, this study reproduces the surface abundance of most low to intermediate mass range elements on an order of magnitude. However, it is limited to a post-processing study of the nucleosynthesis after the post-merger event and does not actually evolve the post-merger object. Therefore, details such as the evolution of the mixing profile, rotation, and expansion of the envelope are not analyzed over the thermal or nuclear timescales.

1.5 This Work

The difficulty in simulating RCB stars is mostly due to the important processes spanning all of the relevant stellar timescales. The merger event happens on the dynamical timescale (minutes to hours) and must be simulated in a 3D hydrodynamics code (Zhang et al., 2014). This work has been done in the past either with Smooth Particle Hydrodynamics (SPH) codes (Staff et al., 2012, 2018) or AMR codes (Dan et al., 2011). The expansion of the He envelope happens on the thermal timescale (thousands of years). Finally, the steady He-burning shell and remaining evolution of the RCB star happens on the stellar nuclear timescale (100,000-1,000,000 years). Because the thermal and nuclear timescales are much longer than the dynamical timescale, they need to be simulated in a separate 1D stellar evolution code such as *MESA*. Doing 1D evolution allows us to simulate over much longer timescales and utilize important reactions on a larger nucleosynthesis grid. Finally, after the evolution of the RCB star, we are also utilizing the NuGrid post-processing code, *MPPNP*

(Herwig et al., 2008). *MPPNP* uses a more complete nuclear network with 1093 species and over 14,000 reactions to post-process nucleosynthesis calculations for every zone at every timestep. The post-processing is important as the *MESA* nuclear network is inefficient and becomes too slow with a larger number of isotopes while *MPPNP* can efficiently compute the nucleosynthesis of a much larger grid while following the stellar computations done by *MESA*.

In the following chapters, we simulate RCB stars two ways. First, we use the 3D to 1D mapping method to simulate the dynamical merger in *Octo-Tiger*, a 3D AMR hydrodynamics code used in this work to simulate merger events (Marcello et al., 2016), and simulate the post-merger evolution in *MESA*. The second method we use is stellar engineering, which does not contain direct information about the dynamical merger, but allows for more freedom in exploring the parameter space of the SOF, mass distribution, and entropy profile. This larger freedom will allow us to constrain the requirements of a dynamical merger with the knowledge of what combination of parameters produce abundances in agreement with observations. Finally, in order to extend the 3D to 1D mapping framework beyond white dwarf mergers, we also attempt to model a merger and post-merger evolution of a giant and main sequence star which is thought to be a possible progenitor for Betelgeuse (Wheeler et al., 2017).

CHAPTER 2.
METHODS: MAKING AN RCB PROGENITOR

2.1 Creating the RCB Progenitor

Our post-merger simulations build on previous work done using "stellar engineering" in *MESA* (Lauer et al., 2019). In the previous approach, a post-merger structure was constructed in order to mimic a thermal and chemical structure consistent with that found in past 3D hydrodynamics merger simulations. The effects of rotation were included by assuming solid body rotation with 20% break-up velocity. Then, the post-merger evolution is followed to the RCB phase using the MESA 75-isotope nuclear network, `mesa_75`. The surface abundances, surface rotation rates, and the time spent in different phases were computed for several models with differing mass parameters.

In this chapter, we present two methods to create an RCB model. The first is using *Octo-Tiger* to simulate the dynamical merger and then map the post-merger object into *MESA*. This procedure involved taking a weighted spherical average of the density and internal energy and cylindrical average of the angular momentum from the 3D *Octo-Tiger* grid and importing it into the 1D spherical grid of *MESA*. This has the obvious advantage of using the thermal structure directly computed as a result of a merger event. The second method is an improved stellar engineering procedure from that presented in Crawford et al. (2020) and Lauer et al. (2019). The advantage of this method is more freedom in changing thermodynamic variables in order to perform a more extensive parameter study.

2.1.1 Mapping 3D to 1D

The method presented here uses one 3D hydrodynamics model that has either a solar or sub-solar metallicity composition imposed onto the post-merger object. In each choice of metallicity, the evolution of the post-merger object is followed through the RCB phase and back to the WD state. The initial conditions of each model are summarized in Table 2.1.

The first step in RCB evolution is a CO+He WD merger event. There are two important constraints on the close-binary WD system. Those constraints are that the merger be dynamically unstable and that the post-merger object has a hot enough shell to commence He-burning. The necessity for a He-burning shell and an unstable dynamical merger constrain the total mass and mass ratio to 0.7-1.0$M_\odot$ and 0.5-0.7, respectively. More details on these contraints can be found in Section 1.3 and Appendix 5.3.

Our 3D hydrodynamics simulation, *Octo-tiger*, is initialized with a 0.53$M_\odot$ CO WD and a 0.32$M_\odot$ He WD. *Octo-tiger* uses a simple zero-temperature WD (ZTWD) and ideal gas EoS. The ZTWD EoS assumes a zero temperature electron gas with a mean molecular weight per free electron of 2 atomic units. The mean molecular weight for ions and electrons used

Sections 2.1.1 and 2.2 were previously published as *R Coronae Borealis Star Evolution: Simulating 3D Merger Events to 1D Stellar Evolution Including Large-scale Nucleosynthesis* by Bradley Munson, Emmanouil Chatzopoulos, Juhan Frank, Geoffrey C. Clayton, Courtney L. Crawford, Pavel A. Denissenkov, and Falk Herwig in The Astrophysical Journal, 911:103 (DOI: 10.3847/1538-4357/abeb6c). Sections 2.1.2 and 2.3 were previously published as *Improved Models of R Coronae Borealis Stars* by Bradley Munson, Emmanouil Chatzopoulos, and Pavel A. Denissenkov in The Astrophysical Journal, 939:45 (DOI: 10.3847/1538-4357/ac9476).

Table 2.1. Initial conditions of all 32 3D to 1D mapped models. "`overshoot_f`" is the extension beyond the convective zone boundary in fractional scale heights. Initial ^{1}H refers to the initial mass fraction of ^{1}H present in the helium envelope. The asterisk denotes models that were post-processed with the *MPPNP* code.

Model	$M_{tot}(M_\odot)$	$M_{CO}(M_\odot)$	Metallicity	`overshoot_f`	Initial ^{1}H
1	0.8	0.53	Solar	0	2.86×10^{-5}
2	0.8	0.53	Solar	0	10^{-99}
3	0.8	0.53	Solar	0	10^{-20}
4	0.8	0.53	Solar	0	10^{-10}
5	0.8	0.53	Solar	0	10^{-6}
6	0.8	0.53	Solar	0	10^{-4}
7	0.8	0.53	Solar	0	10^{-3}
8	0.8	0.53	Solar	0.014	2.86×10^{-5}
9	0.8	0.53	Solar	0.02	2.86×10^{-5}
10	0.8	0.53	Solar	0.03	2.86×10^{-5}
11	0.8	0.53	Solar	0.05	2.86×10^{-5}
12	0.8	0.53	Solar	0.055	2.86×10^{-5}
13	0.8	0.53	Solar	0.06	2.86×10^{-5}
14	0.8	0.53	Solar	0.065	2.86×10^{-5}
15	0.8	0.53	Solar	0.068	2.86×10^{-5}
16	0.8	0.53	Solar	0.07	2.86×10^{-5}
17	0.8	0.53	Solar	0.073	2.86×10^{-5}
18	0.8	0.53	Solar	0.075	2.86×10^{-5}
19	0.8	0.53	Solar	0.1	2.86×10^{-5}
20	0.8	0.53	Solar	0.14	2.86×10^{-5}
21*	0.8	0.53	Solar	0.073	2.86×10^{-5}
22	0.8	0.53	Sub-Solar	0	7.20×10^{-5}
23	0.8	0.53	Sub-Solar	0	10^{-99}
24	0.8	0.53	Sub-Solar	0	10^{-20}
25	0.8	0.53	Sub-Solar	0	10^{-10}
26	0.8	0.53	Sub-Solar	0.06	10^{-99}
27	0.8	0.53	Sub-Solar	0.065	10^{-99}
28	0.8	0.53	Sub-Solar	0.068	10^{-99}
29	0.8	0.53	Sub-Solar	0.07	10^{-99}
30	0.8	0.53	Sub-Solar	0.073	10^{-99}
31	0.8	0.53	Sub-Solar	0.068	10^{-10}
32*	0.8	0.53	Sub-Solar	0.068	10^{-10}

in the ideal gas EoS is calculated for fully ionized He for the secondary (4/3 atomic units) and an equal mixture of fully ionized C and O by mass for the primary (1.75 atomic units).

The pressure and energy equations used for the ZTWD EoS are shown in Benz et al. (1990) and are shown below in a slightly different form.

$$P_{deg} = A\left[\left(x(2x^2-3)(x^2+1)^{\frac{1}{2}} + 3\sinh^{-1}x\right)\right] \tag{2.3}$$

$$E_{deg} = A\left[8x^3\left((x^2+1)^{\frac{1}{2}}-1\right) - \left(x(2x^2-3)(x^2+1)^{\frac{1}{2}} + 3\sinh^{-1}x\right)\right] \tag{2.4}$$

Where

$$x = \left(\frac{\rho}{B}\right)^{\frac{1}{3}} \tag{2.5}$$

$$\begin{aligned} A &= \frac{\pi m_e^4 c^5}{3h^3}, \\ B &= \frac{8\pi m_p \mu_e}{3}\left(\frac{m_e c}{h}\right)^3 \end{aligned} \tag{2.6}$$

While the primary and secondary stars are tracked as fluids, *Octo-tiger* does not trace abundances and therefore we cannot directly obtain a composition profile from this simulation. More details of the composition initialization are discussed later in this Section. The initial orbital period of the binary is 149 seconds and the initial grid is 24,000 sub-grids with up to seven levels of refinement. The refinement criterion is based solely on the density. Because *Octo-tiger* does not handle gravitational radiation nor magnetic fields, angular momentum is removed from the system at a user-defined rate. For this system, the dynamically unstable merger event initiates after about an hour. After 3.3 hours of evolution in *Octo-tiger*, we spherically average the grid to be mapped into *MESA*. Equatorial and polar slices of the density and temperature are shown in Figures 2.1, 2.2, 2.3, and 2.4. In Figures 2.3 and 2.4, a hot shell is clearly visible and has a peak temperature of about 285 MK, which is notably lower than the models in Lauer et al. (2019), but still high enough to initiate He-burning as seen in Figure 2.5.

In order to compute the spherically averaged parameters, the following procedure was implemented. First, the center of mass was found by finding the 3D grid cell with maximum density; then, all positions are translated so that the center of mass is at the origin. Next, we create roughly 350 spherical shells (or cylindrical shells for angular momentum averaging) centered on the origin with radius r and thickness dr such that $\log\frac{dr}{r}$ is constant. This binning in log-space and resolution helps to ensure that we get good resolution near the He-burning region and in the outer layers of the star. For each shell, we sum the product of a parameter X_i and cell volume dV_i for all cells in between a radius r and $r+dr$ and divide by the volume of the shell to get the spherically averaged parameter X_r at radius r (shown in Equation 2.7). Additionally, we compute the total energy of each shell as the sum of the spherically averaged bulk kinetic energy and a calculated potential energy (Equation 2.8). The radius of the spherical post-merger object is then taken to be the outer radius where the material is bound. For this system, we obtain a radius of $0.50R_\odot$ and a total bound mass of $0.80M_\odot$. We note that the difference between the bound mass and the initial masses of the

progenitors indicates a mass loss of $0.05 M_{\odot}$, which is likely overestimated by the spherical averaging procedure.

$$X_r = \frac{\sum X_i dV_i}{\sum dV_i} \tag{2.7}$$

$$\Phi(r) = -\frac{GM_r}{r} - 4\pi G \int_r^{\infty} r' \rho(r') dr' \tag{2.8}$$

One concern with taking the spherical average at this point in the hydrodynamics simulation is that the post-merger object is clearly not spherical in Figure 2.2. However, Schwab et al. (2012) find that these systems tend towards spherical states on the time-scale of a few hours. We attribute the toroidal shape of our system to the fact that *Octo-tiger* does not have a prescription for viscosity and thus, other than numerical diffusion, there is no physical mechanism to diffuse angular momentum. We find that spherically averaging this system reduces the He-burning region temperature by a factor of two, which is likely due to the non-spherical state of the system "smearing" the peak temperature over the polar angle. It is important to note here that due to the high sensitivity that nuclear reactions have on temperature, these small factors could result in large changes in composition during post-merger evolution.

After evolving the WD binary system to a merger event and spherically averaging the post-merger object, the post-merger must be evolved on a nuclear timescale. This evolution is done by mapping our spherically averaged post-merger object into *MESA* using the *MESA* built-in relaxation algorithms. A discussion of how *MESA* relaxes models can be found in Section B of the Appendix in Paxton et al. (2018). In order to map this object into *MESA*, three profiles are required: composition, specific angular momentum, and entropy. Assumptions and methods used to obtain those profiles are outlined in the remainder of this subsection.

Assuming both components of the post-merger object are well mixed, we impose two different uniform compositions for the CO- and He-WD. The composition is obtained by running the *MESA* test suite problems `make_co_wd` and `make_he_wd` for the solar and sub-solar metallicities. The metallicity fractions used in these models were the *MESA* default options from Grevesse & Sauval (1998). We then impose the CO WD composition on the post-merger object up to the mass coordinate corresponding to the original mass of the CO WD ($0.53 M_{\odot}$ in our system). Next, we impose the He WD composition from the mass coordinate of CO WD to the surface. An illustration of this composition can be found for some key elements in Figure 2.6. This assumes that any mass lost in the system is only lost by the He WD, which is a good assumption since the He WD experienced a tidal disruption while the CO WD remained mostly inert and intact. Because *Octo-tiger* does track the components as fluids, one could in principle use the component fractions in each cell to calculate an abundance, assuming the WDs were well mixed and had a homogeneous composition. However, these AMR simulations tend to overestimate the amount of material dredged up from the primary compared to other hydro simulations (Staff et al., 2012, 2018). Staff et al. (2018) claim that mixing during the dynamical merger phase has important effects on the surface abundance. In particular, it is important to avoid dredging up too much material from the primary as it could create an overabundance of ^{16}O and make it

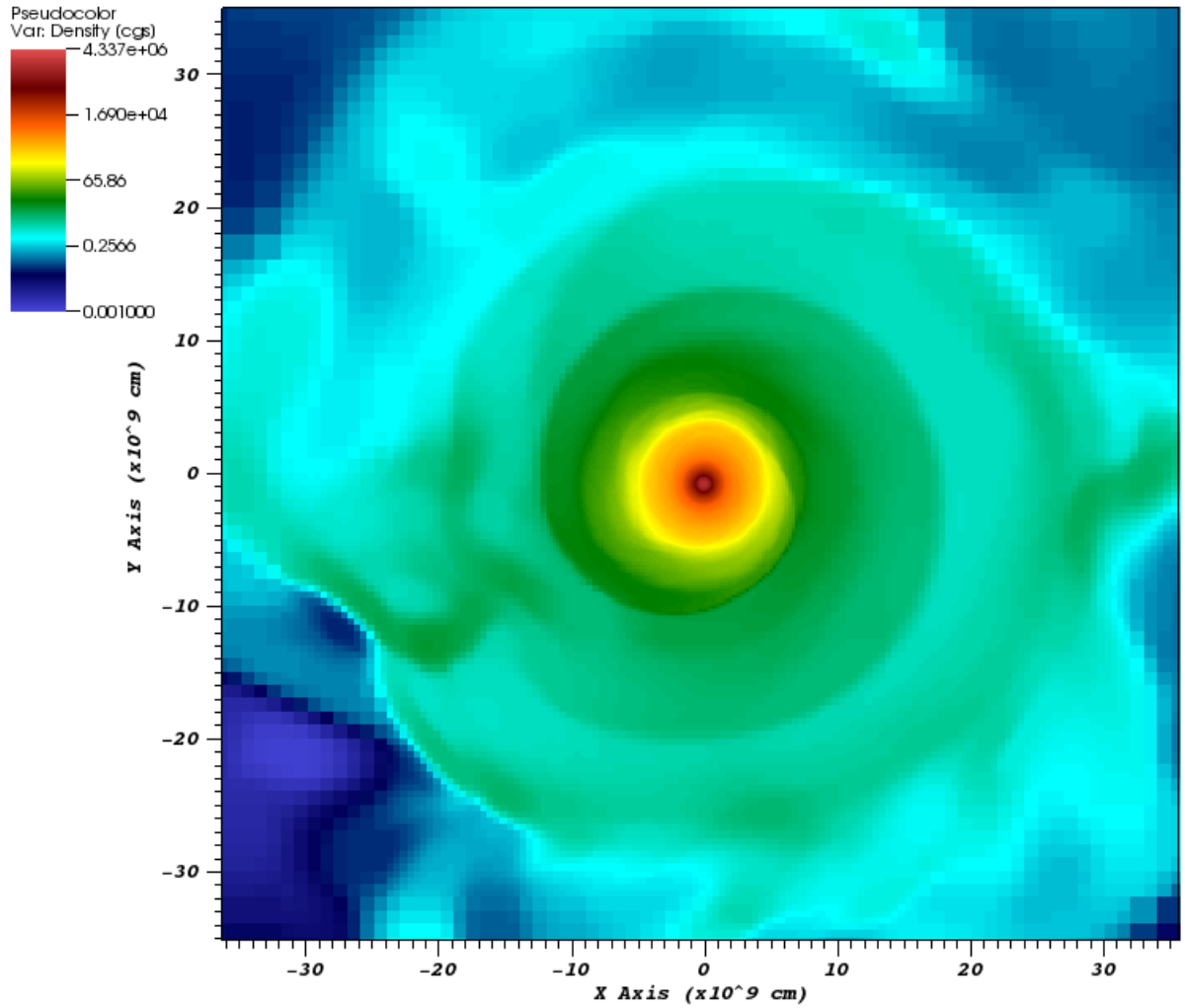

Figure 2.1. Pseudocolor plot of the density in a slice of the equatorial plane after 3.3 hours of evolution time. This is from the simulation of a $0.53M_{\odot}$ CO + $0.32M_{\odot}$ He WD merger.

difficult to produce a sufficient amount of ^{18}O in order to obtain the isotopic ratio of order unity. Therefore, we find the method of imposing a composition based on mass coordinate to be more reliable.

The angular momentum comes directly from the 3D hydrodynamics grid by computing the axially symmetric angular momentum from the linear momentum and the radius as seen in Equation 2.9. After computing the specific angular momentum for each cell, it is averaged using Equation 2.7 with cylindrical shells.

$$\vec{j} = \vec{r} \times \vec{p} = xp_y - yp_x \tag{2.9}$$

The immediate problem with obtaining the entropy profile from *Octo-tiger* is that the entropy is not an evolved variable and uses a much simpler EoS than *MESA*. The zero temperature WD and ideal gas EoS of *Octo-tiger* will not match the EoS tables used by *MESA*, especially in extreme regions of high density and high temperature. Figure 50 of

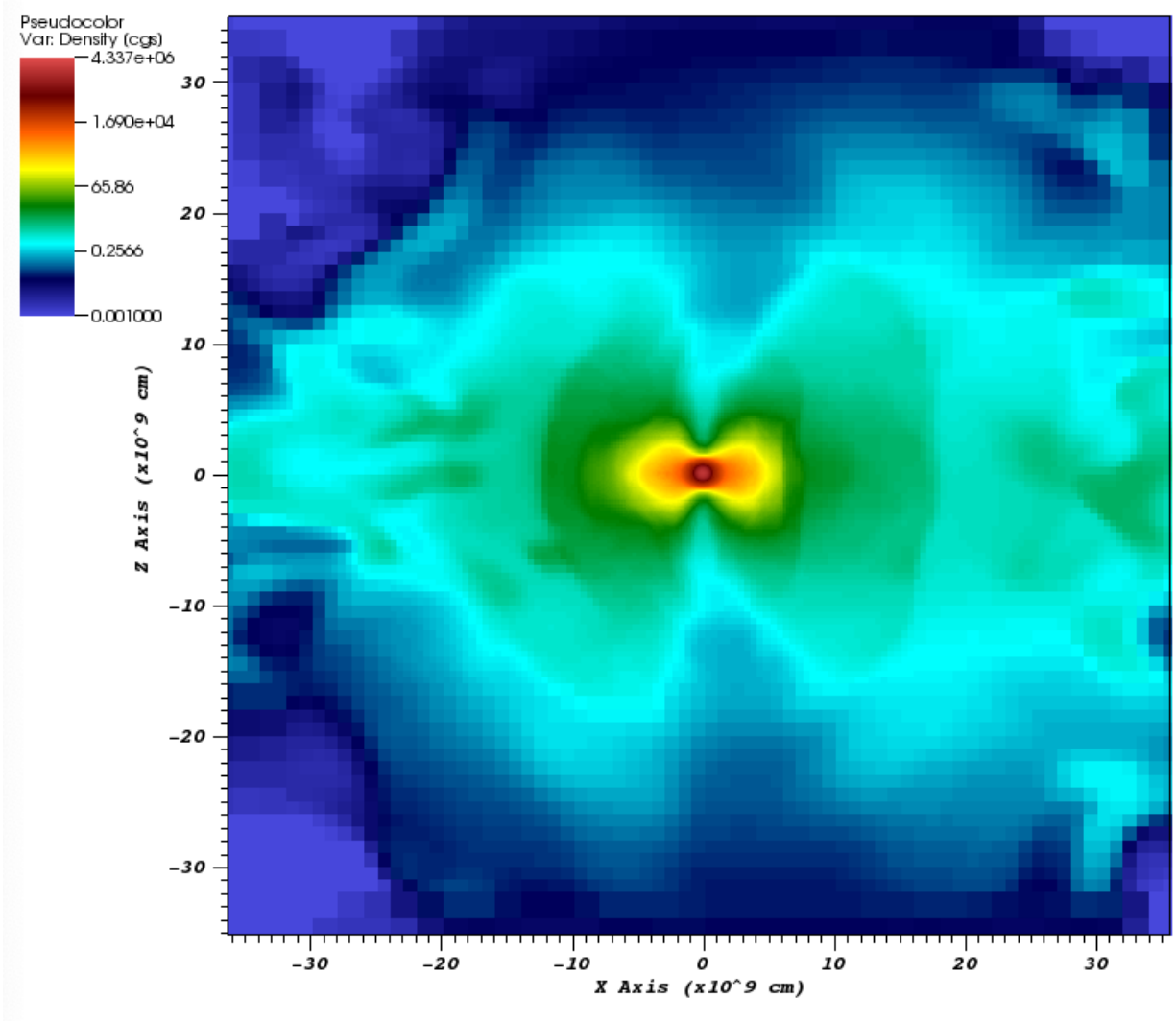

Figure 2.2. Pseudocolor plot of the density in a slice of the polar plane after 3.3 hours of evolution time. Details of the merger are described in Figure 2.1.

Paxton et al. (2019) shows the density-temperature coverage of the EoS used in *MESA*. Rather than directly relax an entropy profile, *MESA* can compute an entropy profile by relaxing a density and temperature profile. This is the method we implement because it allows us to compare density and temperature profiles to the previous work in Lauer et al. (2019) and we can produce an informed temperature structure of the CO core. The density profile is simply spherically averaged from *Octo-tiger*, but the temperature profile needs to be computed using the evolved internal energy density. Using the *Octo-tiger* internal energy density and the composition profile we imposed on the post-merger object, we compute a temperature profile using the Helmholtz EoS (Timmes & Swesty, 2000). Because *Octo-tiger* assumes a zero temperature WD EoS in the highly dense CO core, we floor this temperature to a constant value of 10 MK. The density and temperature profiles are then combined for relaxation in *MESA*.

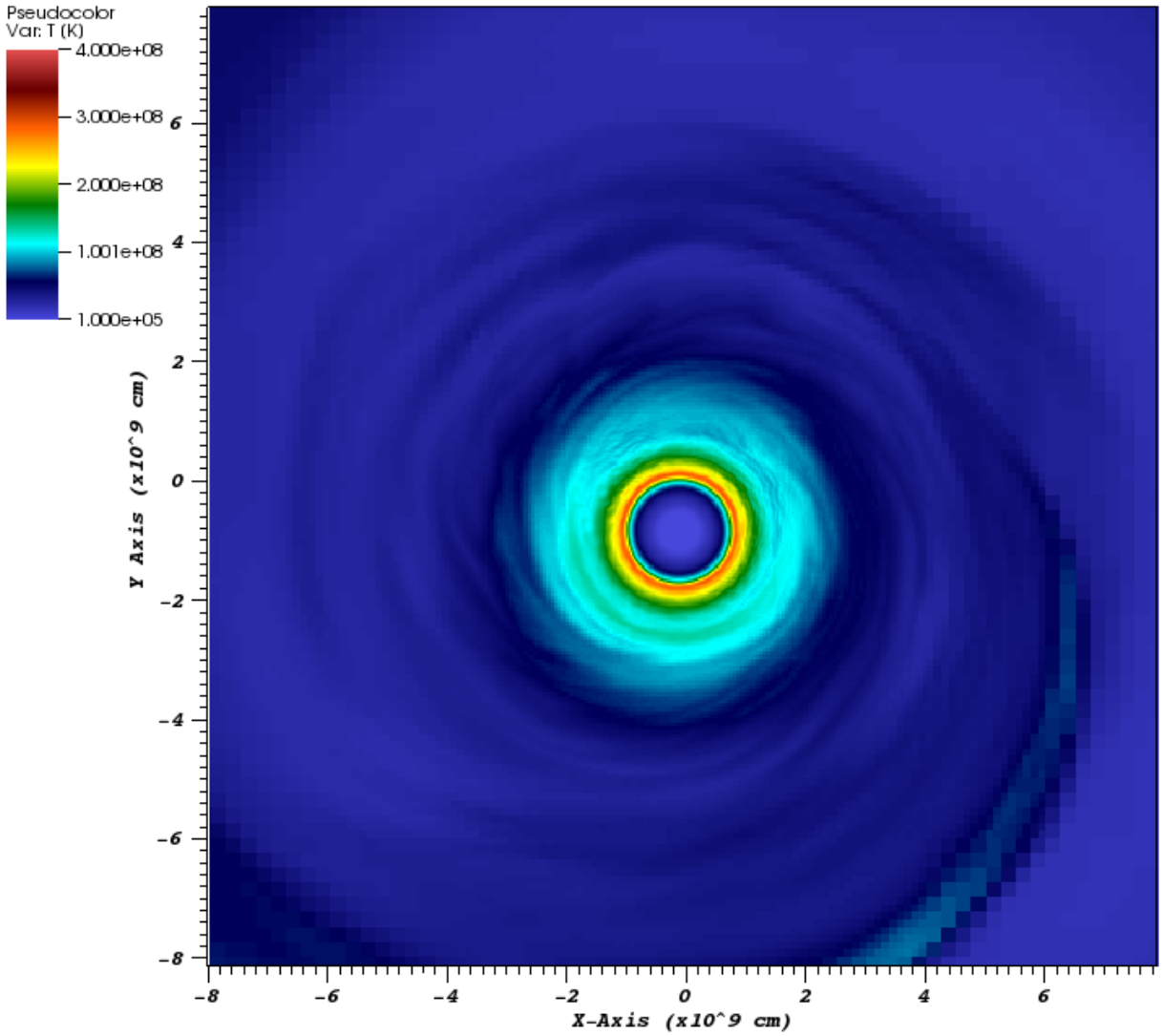

Figure 2.3. Pseudocolor plot of the temperature in a slice of the equatorial plane after 3.3 hours of evolution time. The He-burning region is apparent around the CO core. Since temperature is not an evolved variable in *Octo-tiger*, a simple calculation using the internal energy density, mass density, and the mean molecular weight of fully ionized helium (4/3) is done for the purposes of this illustration. A more rigorous calculation is done for the spherically averaged model. Details of the merger are described in Figure 2.1.

After computing the necessary three profiles, the *MESA* relaxation routine is implemented. Figure 2.5 shows some of the profiles of the spherically averaged *Octo-tiger* output and the relaxed *MESA* model for comparison. Figure 2.5 also shows a density-temperature profile for the *Octo-tiger* output and the *MESA* relaxed model with the He-burning and C-burning regions illustrated. Of these profiles, the only parameter that has a significant difference between the *Octo-tiger* value and *MESA* relaxed value is the temperature (in which the peak relaxed temperature is a factor of 1.5 higher than the peak *Octo-tiger* temperature). We attribute this to the conversion of the *Octo-tiger* internal energy not being

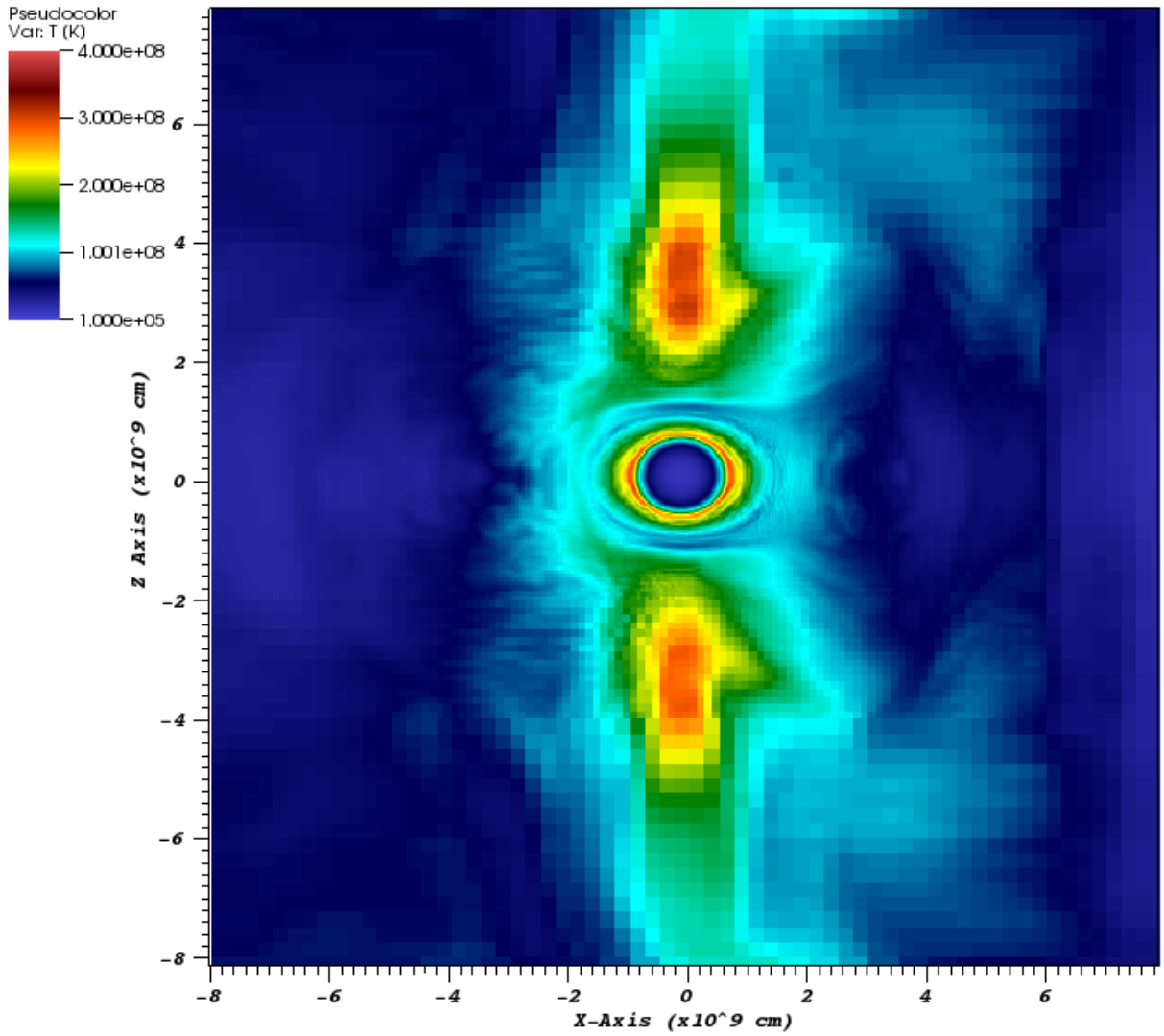

Figure 2.4. Pseudocolor plot of the temperature in a slice of the polar plane after 3.3 hours of evolution time. The He-burning region is apparent around the CO core. Details of the merger are described in Figure 2.1.

hydrodynamically stable with the density profile in *MESA*. However, the peak temperature is still high enough to commence He-burning, a necessary ingredient to obtain the surface abundances observed in RCB stars. It should be noted, however, that even a small range of peak temperature values may significantly change the outcome of the surface abundances during the RCB phase. Crawford et al. (2020) analyze the effect of peak temperature on surface abundance during the RCB phase.

2.1.2 Stellar Engineering

The other approach we implement to create a post-merger object in *MESA* is stellar engineering. We use a method similar to Lauer et al. (2019) and Crawford et al. (2020) with

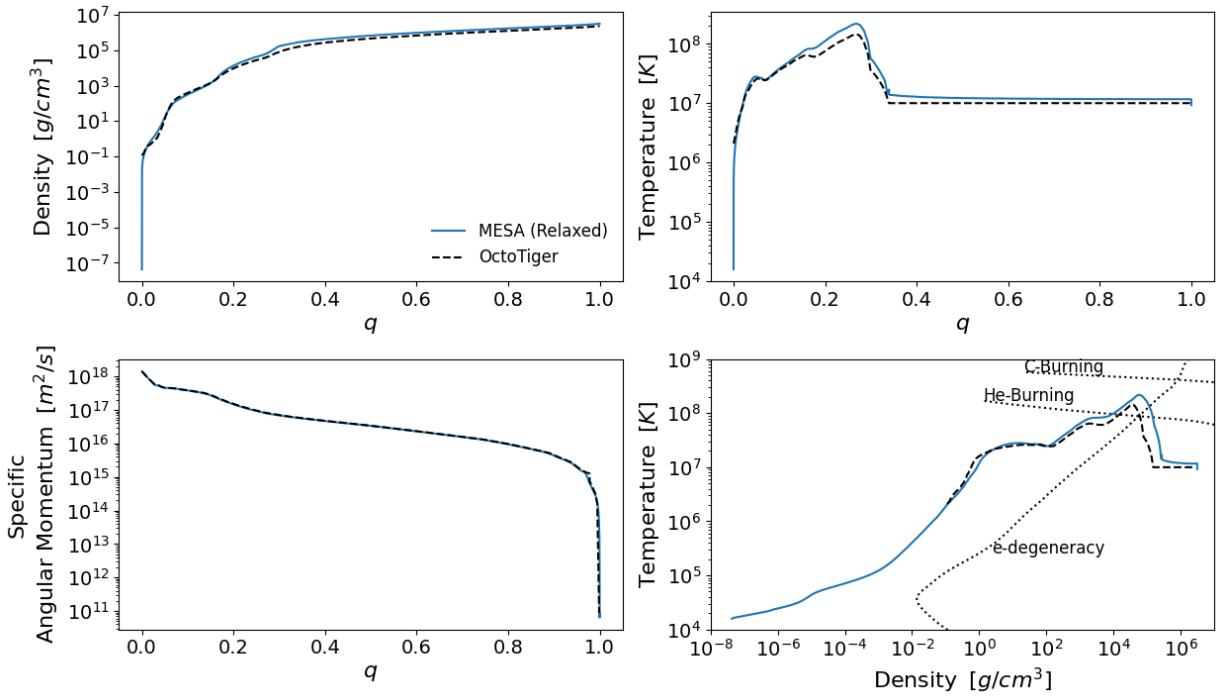

Figure 2.5. A comparison of the spherically averaged final *Octo-tiger* output (dashed) to the *MESA* relaxed output (solid). q is the normalized exterior mass coordinate ($q = 1 - \frac{M_r}{M_{tot}}$)

some slight improvements on the composition initialization. The two properties of the post-merger we must reproduce in our initial model are the thermal profile and the composition. In order to recreate a structure representative of the 3D hydrodynamics results, we first create a ZAMS model with a mass of the progenitor CO- and He-WDs, but the effects of burning and mixing are turned off. The model is then cooled until the core becomes electron degenerate (defined as when the electron chemical potential reaches $5k_BT$).

When the core has reached a degenerate state, a new composition of a CO core and He envelope can be imposed on the model. For this procedure, we attempt a similar approach to the work presented in Menon et al. (2013). The three zones we produce are the core, SOF, and envelope. We find that including a buffer zone in our models is unnecessary as our thermal structure is different from those in Menon et al. (2013) and our mixing does not require it. The core and the envelope of the post-merger are both initialized from CO- and He-WD models evolved separately in *MESA*. After those WD models are complete, we take the composition from the CO- and He- WDs and mass average each isotope for a uniform composition. The results for the CO- and He-WD are then imposed on the core and envelope, respectively.

The SOF region of the post-merger is the result of any nucleosynthesis that occurs during the dynamical merger. As such, we must first process this zone with a short timescale single zone nucleosynthesis simulation. We utilize the `one_zone_burn` module included in *MESA* in order to synthesize a composition calculated by combining a fraction of the CO core and He envelope compositions. The fraction of the CO core material used for each model's SOF can

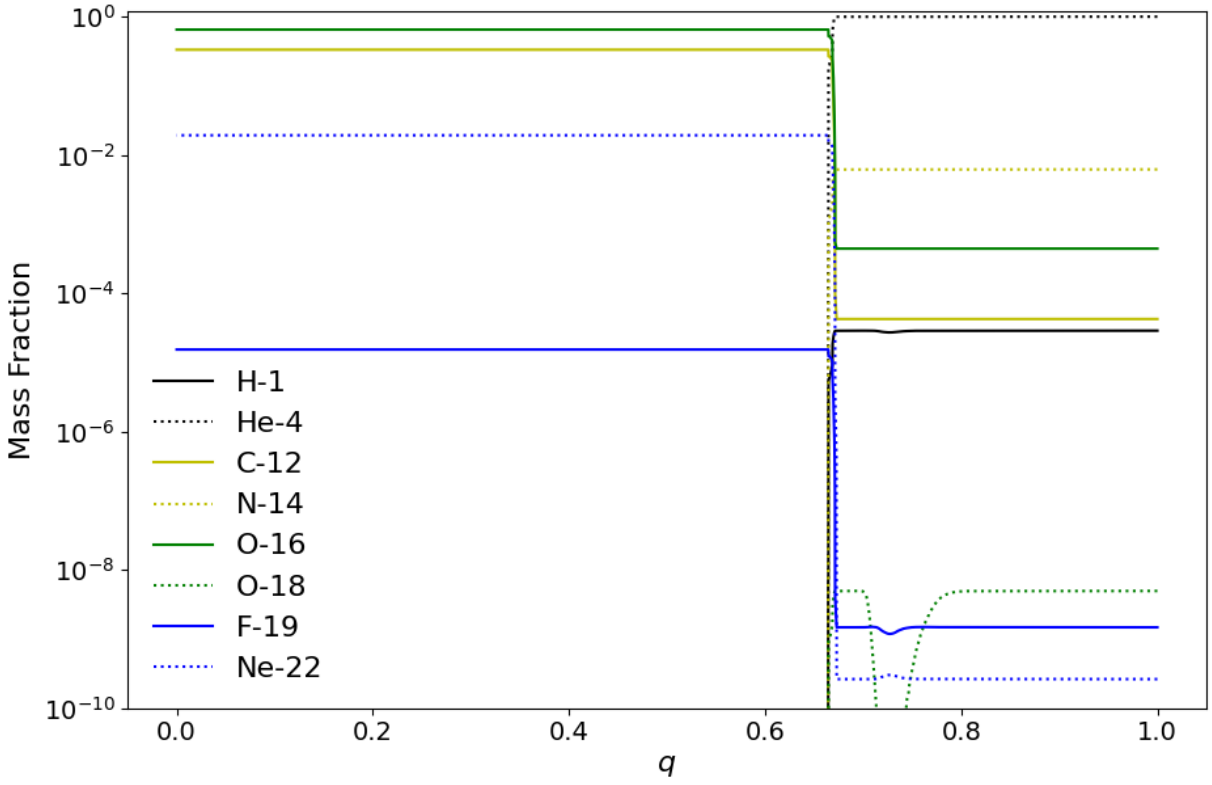

Figure 2.6. Abundance profiles for key species in Model 1 from Table 2.1. The effects of nuclear burning in the hot He shell (or SOF) that has taken place up to that phase can be seen around $q \sim 0.7$-0.8.

be found in Table 2.2. We process this initial composition for one hour at a constant density (roughly $4200\frac{g}{cm^3}$) and initial temperature ($125MK - 250MK$), which is informed by the 3D merger model discussed in the previous subsection. The constant density was taken from the average SOF shell density at the end of the 3D simulation. We note that the density in the SOF ranges from $1700\frac{g}{cm^3}$ to $5100\frac{g}{cm^3}$ and the resulting abundance pattern can vary by an order of magnitude within that range for some key species. However, because most of the SOF has a density on the higher end of that range, our average value is reasonably close to the density of most of the zones in the SOF. A more accurate study could be performed here by implementing a small nuclear network into the 3D merger model in order to retrieve an initial abundance pattern. The temperature is given a range of values to explore due to the uncertainty from the simple EoS used in the 3D model. We utilize a custom nuclear network that includes 40 isotopes ranging from ^{1}H to ^{26}Mg including neutrons. The core fraction included in the SOF is not informed from the 3D model because the effects of dredge up are likely overestimated due to the effects of resolution and instantaneous diffusion in the AMR grid. Staff et al. (2018) suggest that AMR studies may overestimate the material dredged up while SPH based codes may underestimate the dredge up. Further studies of dredge up at the CO/He interface are required to limit this variable. The three zones and their compositions for some key isotopes can be seen in Figure 2.7. We note that while we do not

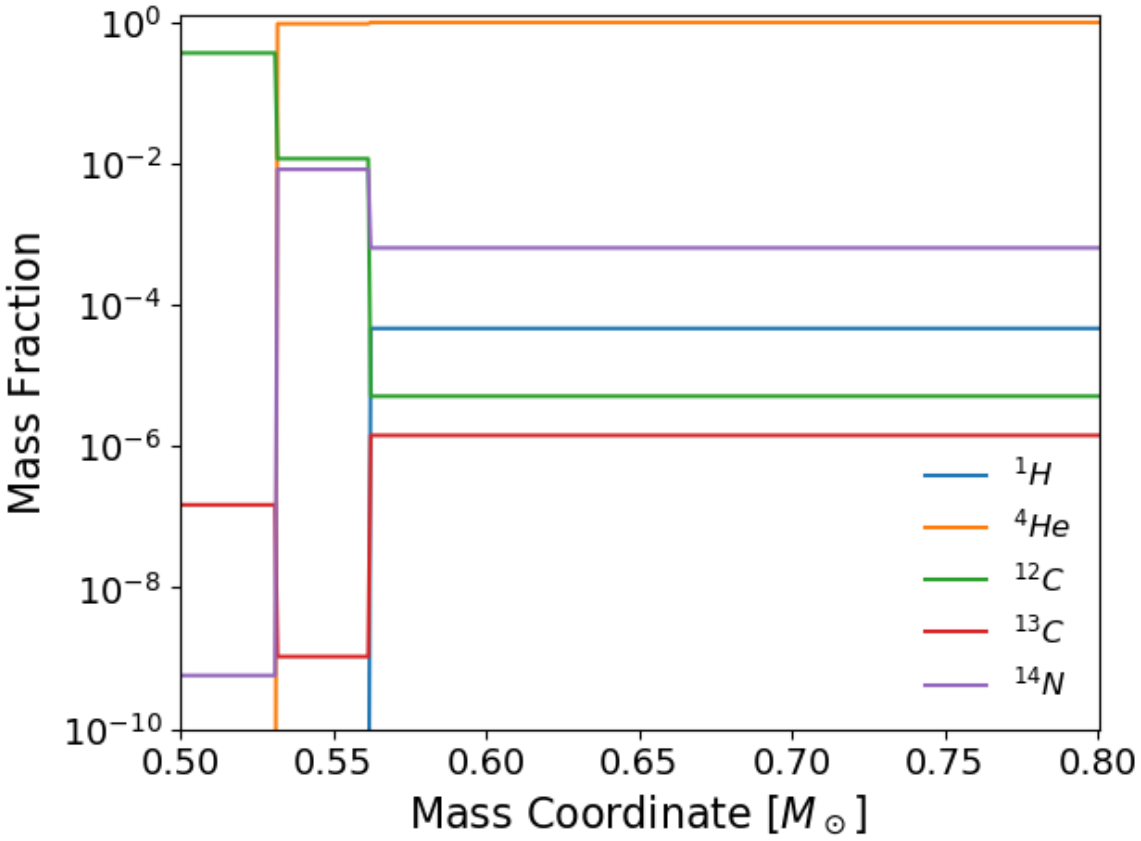

Figure 2.7. An example of the initial composition before mass averaging. This illustrates the core, SOF, and envelope regions individually. The core ends at a mass coordinate of $\simeq 0.53 M_\odot$, the SOF ends at a mass coordinate of $\simeq 0.56 M_\odot$, and the envelope extends through the remainder of the star. This specific composition is from Model A2 of Table 2.2.

change the abundance pattern of the core and envelope resulting from the progenitor CO- and He-WD, respectively, the change in the CO core fraction in the SOF has a significant impact on the resulting envelope abundance and therefore the final results.

A 2-dimensional viscous simulation performed in Schwab et al. (2012) shows that after the merger occurs, the region above the CO-core is fully convective. Because of this convection, we combine the composition of the SOF and envelope by mass averaging the two compositions assuming the SOF is roughly 10% of the envelope mass as is the case in the *Octo-Tiger* model. We now have a two zone composition similar to the models of Lauer et al. (2019) and Crawford et al. (2020); however, the envelope includes a slight enhancement of elements due to the nucleosynthesis during the merger in the SOF. Once this composition is imposed on our model, the core is then allowed to cool to a nearly isothermal state with a temperature of 8MK.

The final step in reproducing the post-merger object is to heat the base of the envelope to He-burning temperatures. Similar to Lauer et al. (2019) and Crawford et al. (2020), we do this by adding heat to the model such that we have a low entropy isothermal core and a

Table 2.2. The results of the parameter study performed on engineered models. $M_{transition}$ represents the mass coordinate of the outer surface of the entropy transition region, T_{peak} represents the maximum temperature in the SOF, `overshoot_f` is the overshooting parameter used in the Mixing Length Theory (MLT) prescription during the MESA evolution, and $M_{CO,SOF}/M_{SOF}$ is the fraction of the accretor material included in the SOF for nucleosynthesis during the merger. All models are based on the hydrodynamics result from the *Octo-Tiger* model in Section 2.1.1 and have an initial total mass of $0.8M_{\odot}$ and a CO core mass of $\simeq 0.53M_{\odot}$.

Model	$M_{transition}$ ($M_{\odot}$)	T_{peak} (MK)	`overshoot_f`	$M_{CO,SOF}/M_{SOF}$
A1	0.53	253	0	0.04
A2	0.55	253	0	0.04
A2 MPPNP	0.55	253	0	0.04
A3	0.57	253	0	0.04
A4	0.6	253	0	0.04
B1	0.55	181	0	0.04
B2	0.55	213	0	0.04
B3	0.55	305	0	0.04
C1	0.55	253	0.04	0.04
C2	0.55	253	0.07	0.04
C3	0.55	253	0.1	0.04
D1	0.55	262	0	0.08
D1 MPPNP	0.55	262	0	0.08

high entropy envelope. However, rather than having an immediate transition at the chemical interface, we use a smoother linear transition with a user-adjusted width. The target profile for entropy looks like the following:

$$S(M_r) = \begin{cases} S_{low}, & M_r < M_{core} \\ S_{transition}, & M_{core} \leq M_r \leq M_{transition} \\ S_{high}, & M_r > M_{transition} \end{cases} \tag{2.10}$$

Where $S_{transition}$ is:

$$S_{low} + \frac{S_{high} - S_{low}}{M_{transition} - M_{core}}[M_r - M_{core}] \tag{2.11}$$

In this equation, S_{low} and S_{high} are the low and high entropy values of the core and envelope, respectively. S_{low} is not a constant value, but rather a function of the mass coordinate such that the core has a constant temperature of about 30MK. M_{core} and $M_{transition}$ are the outer edge mass coordinates of the core (where the mass fraction of He drops 1% of the constant envelope value) and entropy transition region (user defined parameter). Using a smoother entropy transition creates a smooth and wide peak temperature rather than the sharp and narrow peak observed in the engineered models of Lauer et al. (2019) and Crawford et al. (2020). This transition is also more representative of a post-merger object seen in 3D hydrodynamics models (Schwab, 2021). The effects of varying $M_{transition}$ are shown in

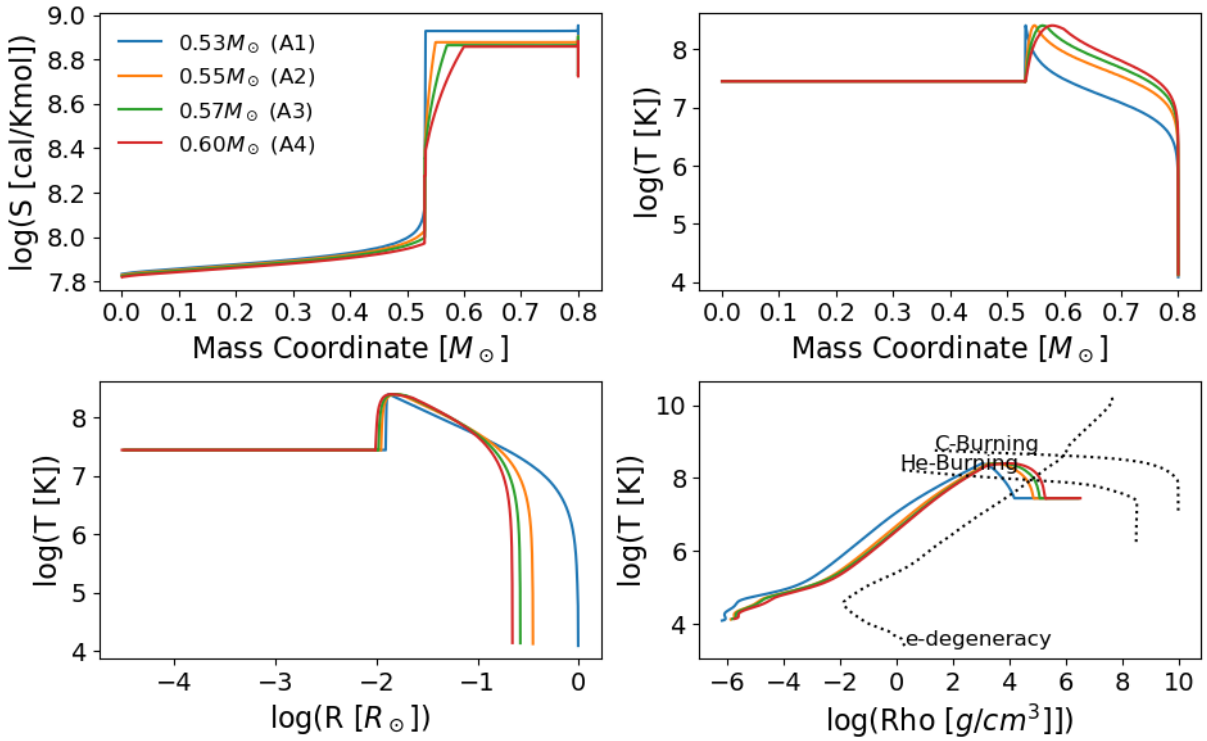

Figure 2.8. Initial structure for models with varying $M_{transition}$ coordinates. The $0.53M_\odot$ model has an instantaneous change from low to high entropy at the CO/He interface similar to the models of Lauer et al. (2019) or Crawford et al. (2020).

Figure 2.8. Similarly, while holding $M_{transition}$ constant and varying S_{high}, one can change the peak temperature in the He-burning region as shown in Figure 2.9.

2.2 RCB Evolution

After creating a post-merger object either by averaging and mapping the 3D post-merger object or stellar engineering, we allow the star to evolve with nuclear burning and mixing turned on. The analysis of surface composition is done at the RCB phase, which is the point at which the star ceases thermal expansion in the envelope. This occurs when the star reaches peak surface brightness and minimum effective temperature on the HRD. We report surface composition of our model using the usual Equation 2.12. In this equation, X is the average mass fraction of the zones with an optical depth less than 1 for a given element, μ_X is the mean atomic mass of the element, and $\log \epsilon(X)_\odot$ is the solar surface value of the element which is taken from Lodders (2003).

$$[X] = \log X - \log \mu_X + 12.15 - \log \epsilon(X)_\odot \tag{2.12}$$

The stellar evolution done in *MESA* uses co-processed nucleosynthesis to track the isotopes through the steady He-burning phase of evolution. The 3D to 1D mapped models utilize the *MESA* built-in `mesa_75` nuclear network, containing a range of isotopes from ^{1}H

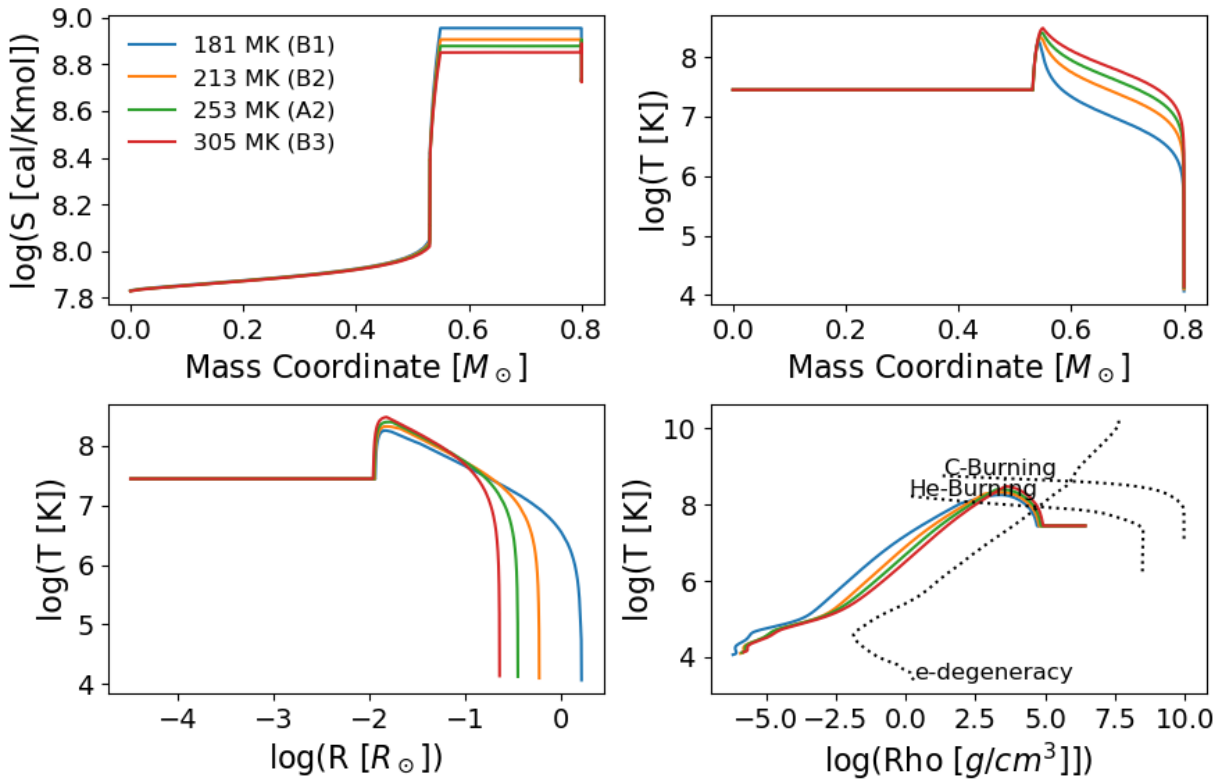

Figure 2.9. Initial structure for models with varying S_{low} which is utilized for control of the He-burning temperature.

to ^{60}Zn including neutrons. This network was used by previous studies that used stellar engineered models to evolve RCB stars (Crawford et al., 2020; Lauer et al., 2019). However, it is not necessary to track many of these higher mass elements with co-processing as their energy generation will be minimal at these He-burning temperatures and their changes can be tracked in post-processing. Therefore, for our stellar engineered models, we create a custom nuclear network that includes 40 isotopes including neutrons. This has the advantage of faster run time and includes important intermediate mass isotopes such as ^{11}B and ^{14}C that `mesa_75` does not include.

2.3 Nucleosynthesis Post-Processing

The last step in the RCB simulation is to post-process the data with a much larger scale nuclear network using the *NuGrid MPPNP* code (Herwig et al., 2008). Since *MPPNP* is a post-processing code, it does not change the evolution of the star, but it performs nucleosynthesis for every zone at every timestep given the parameters calculated in the *MESA* simulation. The *MPPNP* nuclear network we utilize contains 1093 isotopes and over 14,000 relevant reactions - including those involved in the s-process. This builds in the assumption that the energy produced from the high mass nucleosynthesis does not contribute to the stellar structure and the co-processed nuclear networks account for almost all of the

nuclear energy generation. The post-processing code also mixes the species after each time step in accordance with the *MESA* simulation.

Because it would take a significant time to post-process all of the RCB models we have presented, we compute the neutron exposure in order to determine which models are most likely to have enhanced s-process nucleosynthesis. This is done by using Equation 2.13 where n_n is the neutron number density and ν_T is the thermal velocity and their product is the neutron flux.

$$\tau = \int_0^t n_n \nu_T dt' \tag{2.13}$$

Since we are only interested in the abundances on the surface during the RCB phase, we only integrate during the time that there is continuous convective mixing from the burning region to the surface before the RCB phase. After that time, material synthesized in the He-burning shell would no longer be mixed to the surface where we could observe it. According to Herwig et al. (2003), observations of enhanced s-process elements in solar metallicity AGB stars are reproduced at $\tau \simeq 0.4$ mbarn^{-1}.

Any models that reasonably match to the surface abundances of observations and have sufficiently high neutron exposures are post-processed in *MPPNP*.

CHAPTER 3.
RESULTS: ANALYSIS OF RCB EVOLUTION

The following Chapter describes the results of the two methods used to model the evolution of an RCB progenitor. Section 3.1 describes the results of the model that was initialized from the 3D *Octo-Tiger* merger model and then mapped into *MESA*. Using a single *Octo-Tiger* model, we explore a parameter space of overshooting, initial hydrogen abundance, and the robustness of the mapping procedure. Section 3.2 describes the results of the stellar engineered model. This type of model allows us to explore a parameter space that changes the initial thermal profile.

3.1 3D to 1D Mapping

In this section, we discuss the results from our evolutionary models mapped from *Octo-Tiger*. We start by discussing our initial models for solar and sub-solar metallicities. Next, we discuss variations of those cases as we implement varying degrees of overshooting and change the initial abundance of hydrogen in the RCB envelope. Finally, we use the models that best match observations from the solar and sub-solar cases and post-process them with the *NuGrid MPPNP* code for analysis of s-process elements.

3.1.1 Initial 3D to 1D *MESA* models

This section discusses the results from our base solar and sub-solar models that contain no overshooting and no initial hydrogen adjustment (Model 1 and Model 22 from Tables 2.1 and 3.1) for comparison against the engineered models of Lauer et al. (2019). Specifically, we focus on the early stages of evolution following the merger and the mixing that takes place. Then, we discuss how changes in overshooting or initial hydrogen abundance affect the results.

3.1.1.1 Early Stage Evolution

The primary goal of this study is to obtain results similar to observations and compare to those obtained by the stellar engineering procedure of Lauer et al. (2019). In their study, they explore a parameter space consisting of initial radius, total mass, mass ratio, rotation, and initial hydrogen abundance. Of those initial parameters, their model A7 is most similar to our initial conditions in terms of total mass, mass ratio, and initial hydrogen ratio. The major differences in our model are that the initial rotational profile, thermal profile, and radius of the post-merger object are calculated based on the *Octo-tiger* grid. This is also markedly different from other models discussed in Section 1.4 such as those described in

Section 3.1 was previously published as *R Coronae Borealis Star Evolution: Simulating 3D Merger Events to 1D Stellar Evolution Including Large-scale Nucleosynthesis* by Bradley Munson, Emmanouil Chatzopoulos, Juhan Frank, Geoffrey C. Clayton, Courtney L. Crawford, Pavel A. Denissenkov, and Falk Herwig in The Astrophysical Journal, 911:103 (DOI: 10.3847/1538-4357/abeb6c). Section 3.2 was previously published as *Improved Models of R Coronae Borealis Stars* by Bradley Munson, Emmanouil Chatzopoulos, and Pavel A. Denissenkov in The Astrophysical Journal, 939:45 (DOI: 10.3847/1538-4357/ac9476).

Zhang et al. (2014) or Menon et al. (2013). After mapping the 3D merger object from *Octo-tiger* into *MESA* using the procedure outlined in Section 2.1.1, we let it evolve and obtain an HRD track shown in Figure 3.1.

The HRD tracks in this study are similar to those of Lauer et al. (2019) and Schwab (2019) with an early brightening phase leading the model into the RCB box (the observed range of effective temperatures and luminosities of RCB stars) from the bottom. This is different than the models of Weiss (1987) or Menon et al. (2013, 2019) which see a small brightening and cooling phase causing the models to enter the box from the left. This is the result of the 3D merger and engineered models starting off with more compact and cooler cores. The envelope then expands as a result of the energy released from the steady He-burning shell. There is a short period of thermal adjustment in the envelope as the He-burning shell reaches a steady state, after which the solar and sub-solar models have identical tracks in the HRD. This thermal adjustment lasts around 500 years and expands the envelope until $\log(L/L_{\odot})$ reaches 2.5-2.7. Schwab (2019) also sees this thermal readjustment phase in their multidimensional model (ZP4) mapped into *MESA* with similar lifetimes (though that model starts off much brighter than ours). The time it takes for the solar and sub-solar models to enter the RCB phase (minimum effective temperature) are 1600 years and 1300 years, respectively. This is in agreement with the lifetimes reported in Lauer et al. (2019) and the higher He-burning temperature models of Crawford et al. (2020).

3.1.1.2 Surface Abundance and Mixing

While Lauer et al. (2019) do not report surface abundances from model A7, they do report surface $^{16}O/^{18}O$ of about 35 and C/O of about 4.6. This differs from our values of 3.05 and 75.56 significantly. Our $^{16}O/^{18}O$ ratio is in better agreement with observations (Clayton et al., 2007), but our C/O is significantly higher than the observed values ($\sim$1). The reason for this is predominantly due to the difference in early evolution. In our models, the temperature profile of the He envelope evolves rapidly during the thermal adjustment phase, causing differences in the early mixing of elements by convection and the peak temperature getting as high as 400 MK for a brief time, which is illustrated in Figure 3.2. Within the first year of evolution, two distinct convective regions form in the He envelope of the star separated by a temperature inversion. The inner convective region reaches from the He-burning region to the temperature inversion and the outer reaches from the top of the temperature inversion to the surface. This temperature inversion appears to evolve from bumps in the temperature profile which are likely caused by the initial spiral structure of the merger seen in Figure 2.3. This temperature inversion is present and evolves similarly across all models presented in this section. We also note that because this first convective gap is eventually bridged in all of our models, its importance to the surface abundance during the RCB phase is minimal. Lauer et al. (2019) and Schwab (2019) show temperature-density profile plots for engineered models which are much smoother and do not have this temperature inversion present. However, Schwab (2019) does not focus on nucleosynthesis and hence mixing is not as important in their study, and Lauer et al. (2019) do not perform a detailed analysis of their mixing profile.

A clearer presentation of how this affects the mixing is shown in the context of a Kippenhahn diagram in Figure 3.3. The first convective gap caused by the spiral structure can

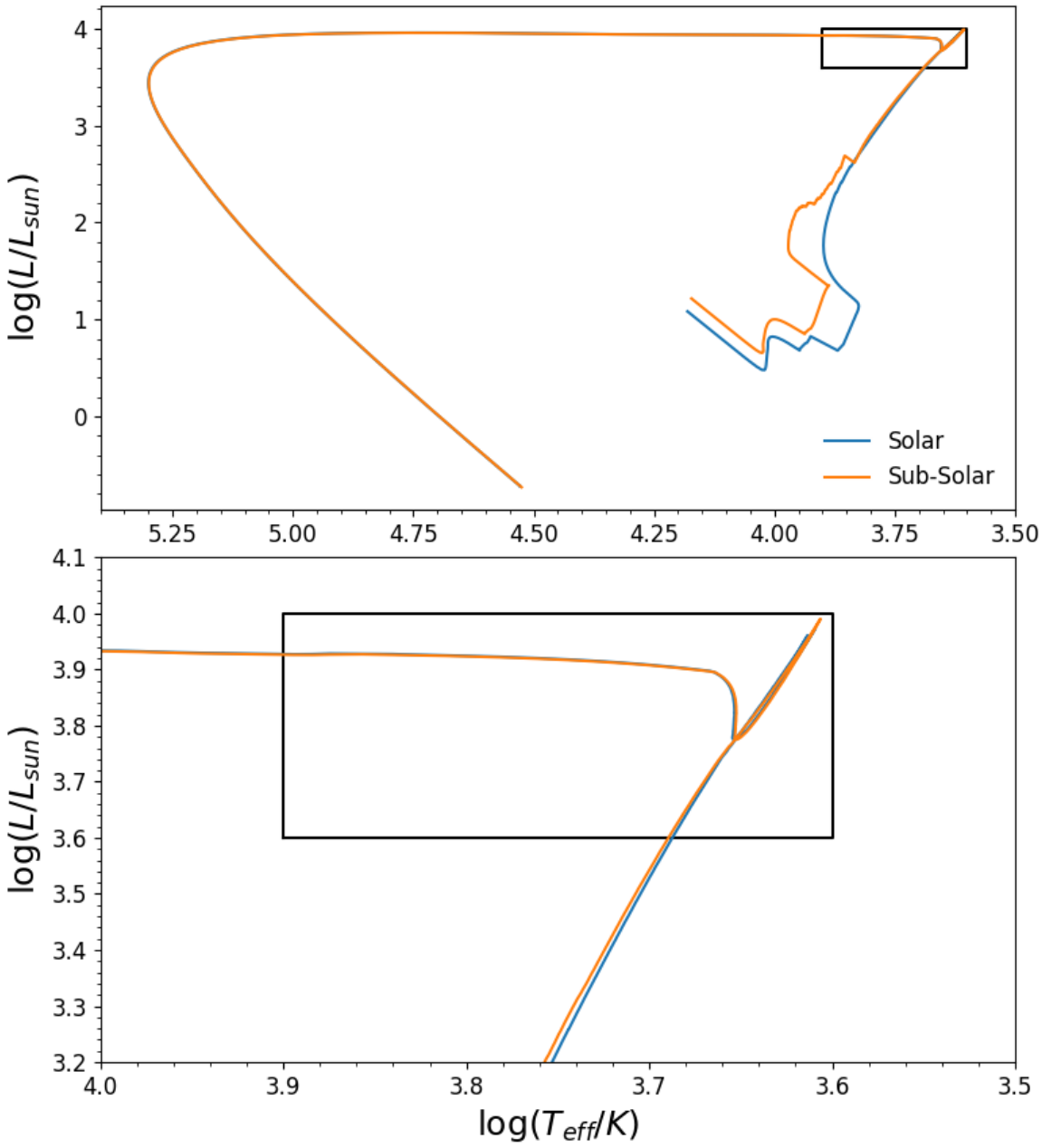

Figure 3.1. The HRD track for solar and sub-solar metallicity RCB stars (Models 1 and 22 from Table 2.1, respectively). The black box represents the range of effective temperatures and luminosities of observed RCB stars.

be seen around $0.77 M_{\odot}$ for the first 40-50 years of evolution. Furthermore, we note that the mixing region between the surface and He-burning shell becomes disconnected after about 30 years, which explains why we see evidence of partial He-burning in RCB stars. The second convective gap is also a feature of the stellar engineered models of Crawford et al. (2020). Because this second convective gap disconnects the surface from the burning region, the surface abundances become set and remain static after that point. This means that the

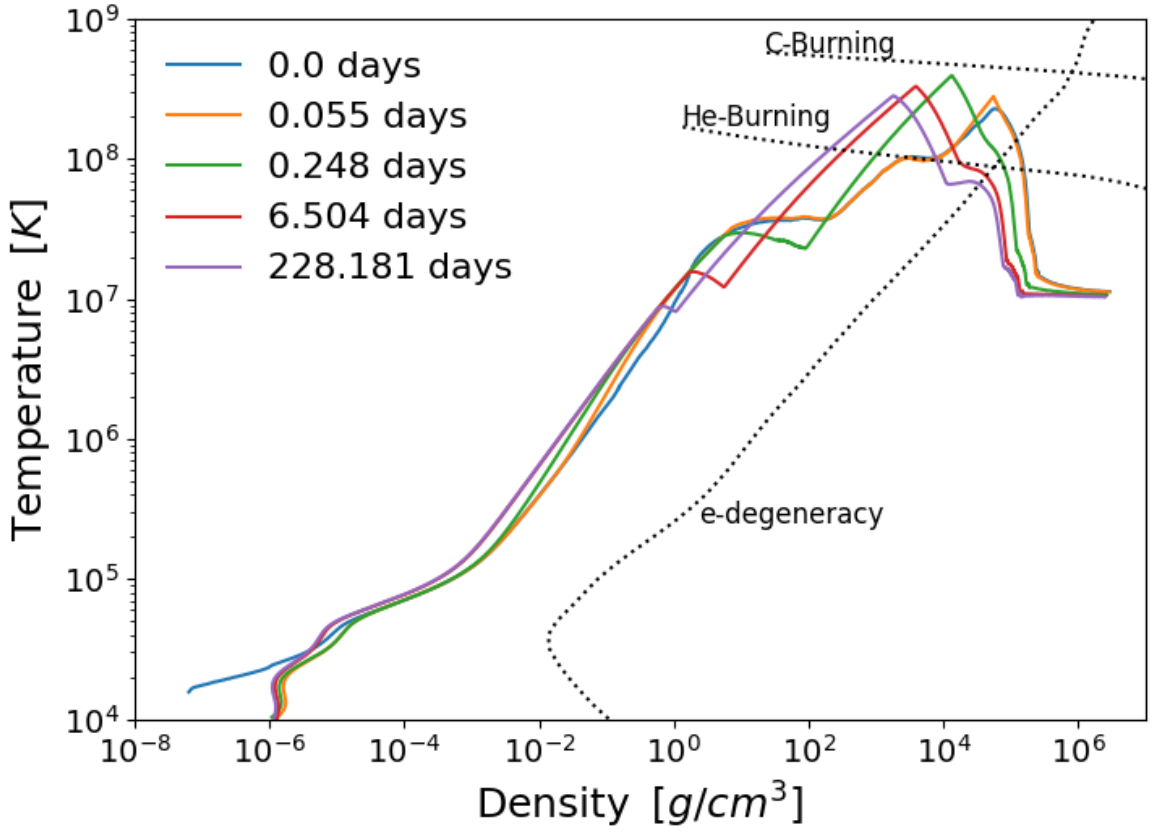

Figure 3.2. This figure demonstrates the first year of evolution of the Temperature-Density profile.

surface abundances are solely dependent on the burning that happens in the first 30 years in our models.

3.1.1.3 Robustness of Convective Solution

Convection is an important feature which brings the partially synthesized material from the burning region to the surface. In order to ensure that convection is a robust feature in our models, we made three test cases with different initial conditions in order to test whether or not convection persists in the envelope. Two of these test cases use a different averaging procedure described in Endal & Sofia (1976), which averages cells on equipotentials (including the effects of rotation) instead of radial shells. One of the equipotential averaged models uses mass weights during the averaging procedure (replacing dV_i with dm_i in Equation 2.7) and the other uses volume weights. The third model uses the density profile obtained by the equipotential averaging procedure with volume weights in order to find a temperature profile in Hydrostatic Equilibrium (HSE). This is done by using the equation for HSE (Equation

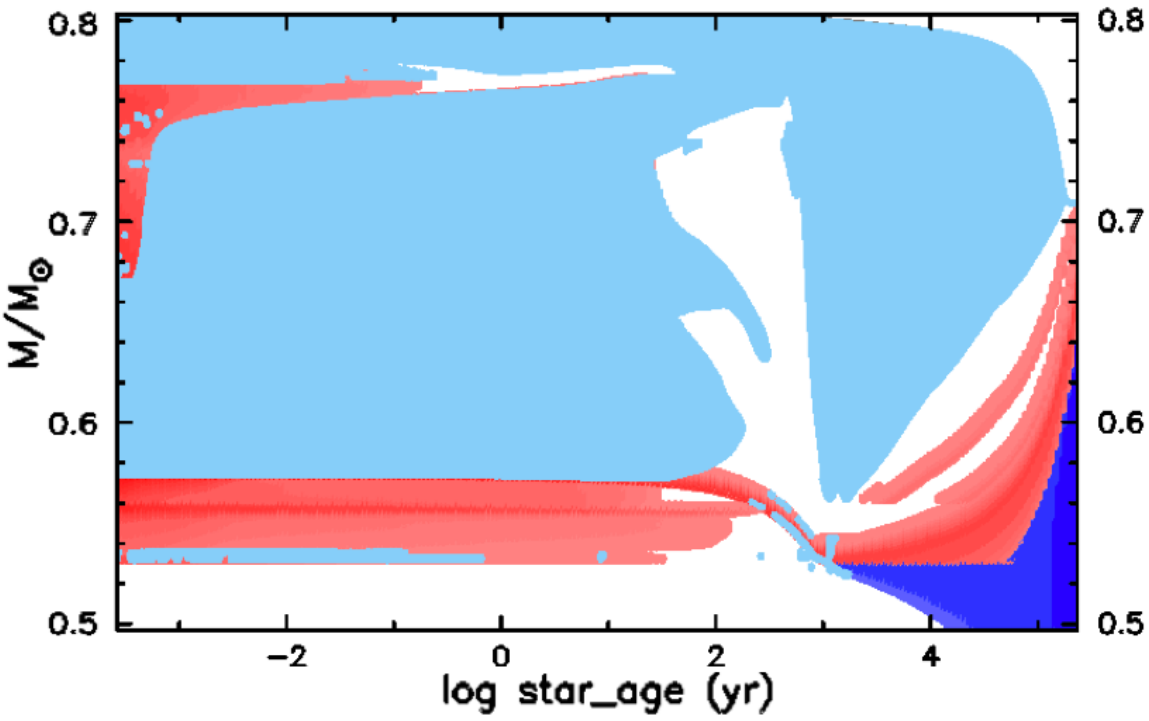

Figure 3.3. Kippenhahn diagram for Model 1. The vertical axis is the mass coordinate and the horizontal axis is the logarithm of the star age. The blue regions indicate mixing and the red regions indicate nuclear energy generation (darker red being more energy generation). The lighter red region at the top of the envelope and behind the blue region is due to beta decay. The RCB phase occurs at 1600 years.

3.14, where Ψ is the effective potential) and the calculated density profile in order to calculate a pressure profile.

$$\frac{dP}{dr} = -\rho \nabla \Psi \tag{3.14}$$

Then, we use the Helmholtz EoS to calculate a temperature given a pressure and density and apply the same procedure outlined in Section 2.1.1 in order to insert the degenerate CO core. Figures 3.5 and 3.6 show the profiles of Model 1 and the HSE model at key phases during their evolution, respectively.

The purpose of these models is simply to demonstrate that the convective instability persists in the envelope independent of the initial averaging procedure we used. Therefore, it is important to note here that these test models are simplistic in terms of the nuclear network and initial composition. The nucleosynthesis in these models may be unreliable and we therefore choose not to analyze the surface abundances during the RCB phase.

These test cases show that despite starting with a different averaging procedure and therefore a different initial thermal profile, these models converge to similar solutions on the order of 10-100 years. All three test models show the same behavior of two distinct convective regions separated by an initial convective gap that eventually merge and a second convective gap forming around the same time causing only partially synthesized material to

mix at the surface of the star. We illustrate this in Figures 3.5 and 3.6 for Model 1 and the HSE test model, respectively. In the top panels, we see the initial convective (left) and temperature (right) profiles as well as the initial composition (labeled in the legend). The middle panels show the profiles right after two distinct convective regions form separated by the temperature inversion discussed earlier. The bottom panels show the moment right after the convective gap closes and synthesized material is allowed to mix to the surface. At this time, the convective region has already receded from the burning region as the star expands and material at the surface will not be synthesized further. This behavior is observed in all of our models regardless of the averaging procedure and demonstrates the robustness of our convective solution. There are, however, fairly large differences in the age of the star at which the first convective gap closes (bottom panel) which would result in differences in nucleosynthesis and therefore surface abundances.

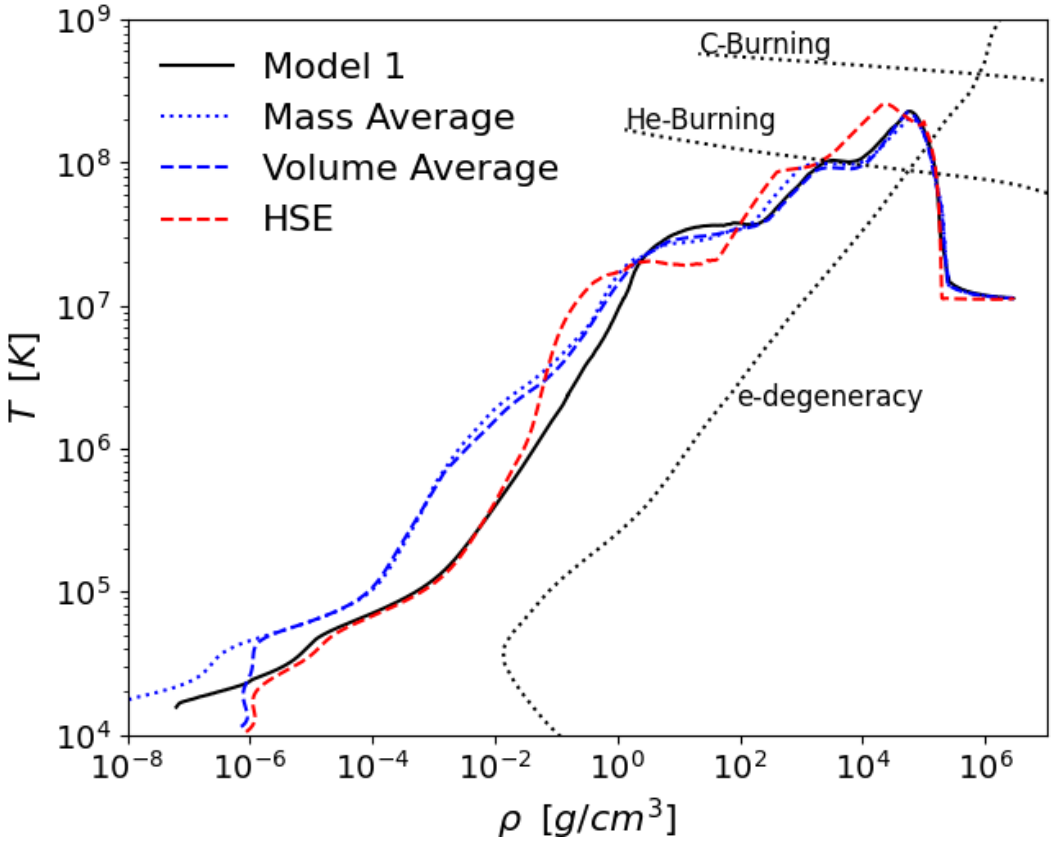

Figure 3.4. A temperature-density profile comparing the three test cases and Model 1 from Table 2.1. The solid black line is Model 1, the blue dotted and dashed lines are mass and volume averaged equipotential models, respectively, and the red dashed line is the model that demands HSE for the averaged density profile.

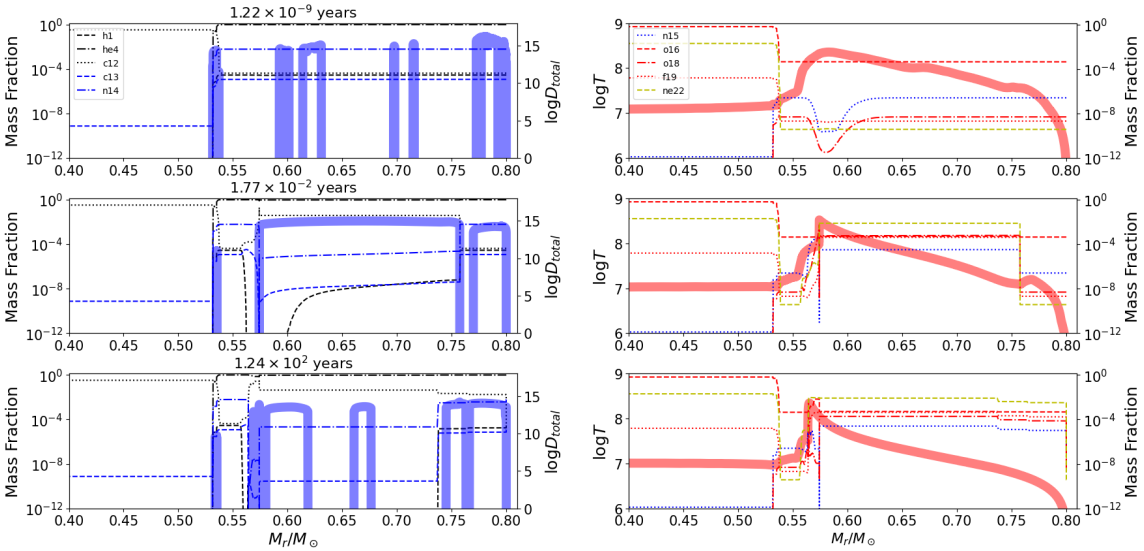

Figure 3.5. The three panels in this image show the profile of Model 1 at three important phases: the initial relaxed phase, after the two distinct convective regions form, and after the first convective gap closes and the synthesized material is brought to the surface. The surface abundances do not change significantly between that last panel and the RCB phase. The wide red line in the right panels indicates temperature and the wide blue line in the left panels indicates the mixing coefficient.

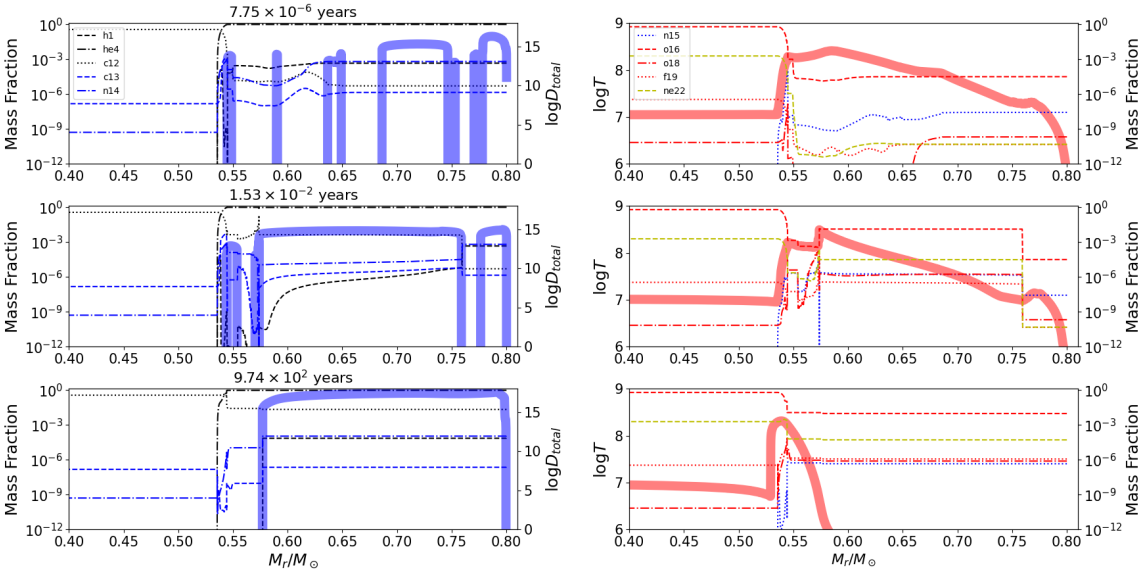

Figure 3.6. The three panels in this image show the profile of a test model which demands HSE be satisfied for our given density profile. The three phases are described in Figure 3.5, but they occur at different times in this model.

3.1.2 Overshooting

In this section, we vary the strength of overshooting, which refers to the ability to diffuse material beyond a convective boundary, and analyze its effects on the surface composition. *MESA* version r12115 contains many parameters for overshooting which change the depth into the convective region (`overshoot_f0`) and the decay length scale outside of the convective region (`overshoot_f`) in fractional pressure scale heights. For both overshooting options, there are 12 parameters associated with different regions of the star (non-burning core, non-burning shell (above and below), H-burning core, H-burning shell (above and below), etc). In this study, we vary all `overshoot_f` parameters and maintain a constant `overshoot_f0` parameter of 0.004. Previous RCB studies have not considered overshooting, but it is an expected physical phenomenon that should be included as one considers more physically motivated models. We maintain overshooting parameters within a reasonable range as discussed in Stancliffe et al. (2015). The results of this study can be found in Figures 3.7 and 3.8 as well as Table 3.1.

In these results, we see a monotonic decrease in the surface abundance of N with increasing overshooting parameter as seen in Figure 3.8. Crawford et al. (2020) varied the He-burning shell temperature and observe a decreasing N abundance with an increasing He-burning region temperature. In both cases, $^{14}\mathrm{N}(\alpha,\gamma)^{18}\mathrm{F}(\beta^+)^{18}\mathrm{O}$ is being enhanced, thus decreasing the amount of N at the surface. This is consistent with the increase in O seen in Figure 3.8 while $^{16}\mathrm{O}/^{18}\mathrm{O}$ remains constant up to an overshooting parameter of 0.07, meaning there is an enhancement in the production of $^{18}\mathrm{O}$ at the same rate as $^{16}\mathrm{O}$. Beyond an overshooting parameter of 0.07, $^{16}\mathrm{O}$ is dramatically enhanced by dredging up material from the CO core. The $^{14}\mathrm{N}(\alpha,\gamma)^{18}\mathrm{F}(\beta^+)^{18}\mathrm{O}$ reaction is paramount in the creation of $^{18}\mathrm{O}$ at the levels seen in observations and is discussed in great detail by Clayton et al. (2007) and Menon et al. (2013). Lastly, as the overshooting parameter increases, we also see a slight increase in Ne. This happens as $^{18}\mathrm{O}$ undergoes α-capture and $^{22}\mathrm{Ne}$ is created, thus increasing $^{16}\mathrm{O}/^{18}\mathrm{O}$ even more. Crawford et al. (2020) also note these key reactions and show that the sum of N, $^{18}\mathrm{O}$, and Ne is effectively constant as a function of He-burning temperature. This indicates that these isotopes are almost exclusively affected by just the $^{14}\mathrm{N}(\alpha,\gamma)^{18}\mathrm{F}(\beta^+)^{18}\mathrm{O}(\alpha,\gamma)^{22}\mathrm{Ne}$ reaction chain.

In this study, we cannot change the He-burning temperature of different models due to the fact that it is self-consistently calculated within the 3D hydrodynamics merger simulation. However, by introducing stronger amounts of overshooting, we are more efficiently bridging the second mixing gap seen in Figure 3.3. This allows for more time for isotopes to synthesize in the He-burning region and mix to the surface before the convective region breaks from the stellar surface. As the strength of overshooting increases beyond a `overshoot_f` value of 0.1, the overshooting beneath the He-burning shell begins to bring up material from the CO core at an overwhelming rate. Since the primary isotopes in the core are $^{12}\mathrm{C}$ and $^{16}\mathrm{O}$ at a 1:2 ratio, $^{16}\mathrm{O}/^{18}\mathrm{O}$ increases dramatically while C/O decreases to the order of unity.

The same study is done with sub-solar models for a subset of the overshooting parameters in this study. The results are shown in Table 3.1, Models 26-30, and we see similar results in the trend of C/O and $^{16}\mathrm{O}/^{18}\mathrm{O}$.

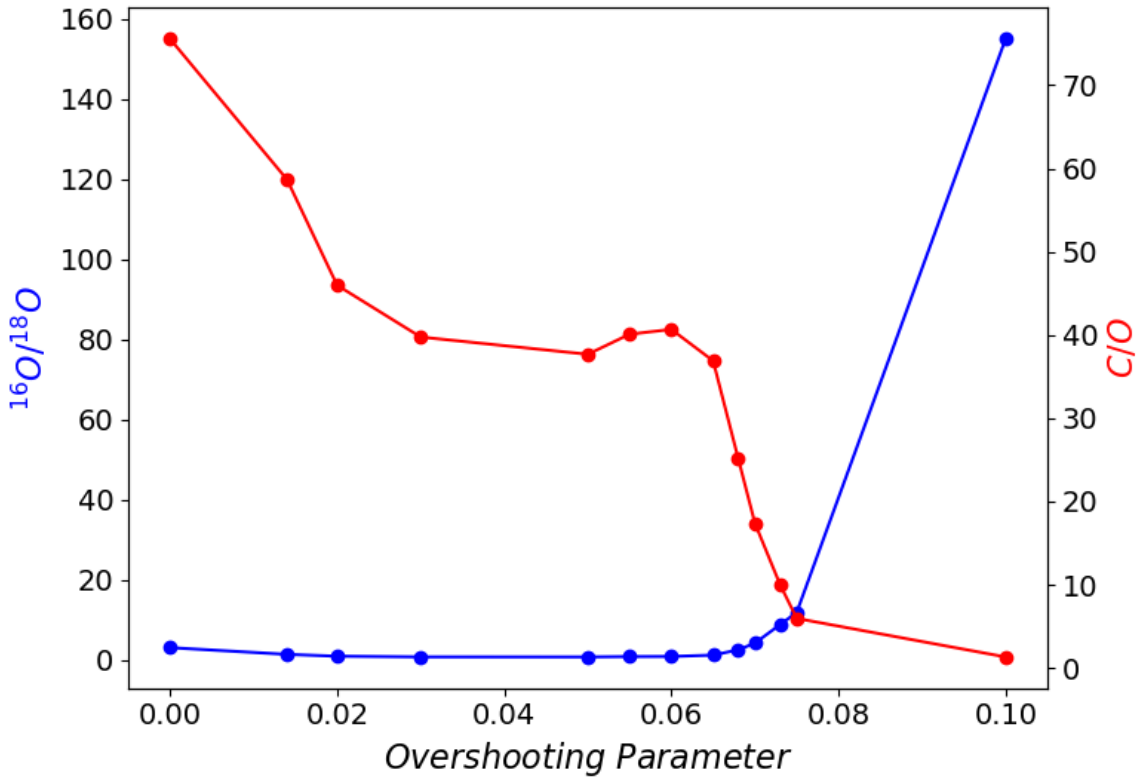

Figure 3.7. The change in ratios C/O and $^{16}O/^{18}O$ with changing overshooting parameter "`overshoot_f`". The model with `overshoot_f` of 0.14 is not shown here in order to maintain the scale, but the results can be found in Table 2.1 Model 20.

3.1.3 Initial Hydrogen Abundance

Zhang et al. (2014) point out the important role of the thin hydrogen envelope in the He WD component of the progenitor binary. They point out that if more of this hydrogen envelope were to survive, more ^{3}He would also survive. In our models, however, there is also a significant abundance of ^{7}Li that survives in the thin hydrogen envelope, which later affects the surface abundances during the RCB phase.

Because we mass average the entire He WD, these abundances in the thin hydrogen envelope have a noticeable effect on the initial uniform abundance of the post-merger He envelope. This is especially true for light elements that are otherwise uncommon in the He WD (^{1}H, ^{3}He and ^{7}Li, specifically). In order to study the effects of this process, we vary the initial hydrogen abundance in the He envelope while maintaining an `overshoot_f` value of 0. The results are shown in Figures 3.9 and 3.10. There are studies such as Staff et al. (2012) that show a relationship between He WD mass and the mass of the thin hydrogen envelope and would then set the mass fraction of hydrogen in the envelope of the RCB progenitor. However, we justify varying the initial hydrogen mass fraction because any hydrogen burning during the dynamical merger phase is not included in our simulations since *Octo-tiger* does

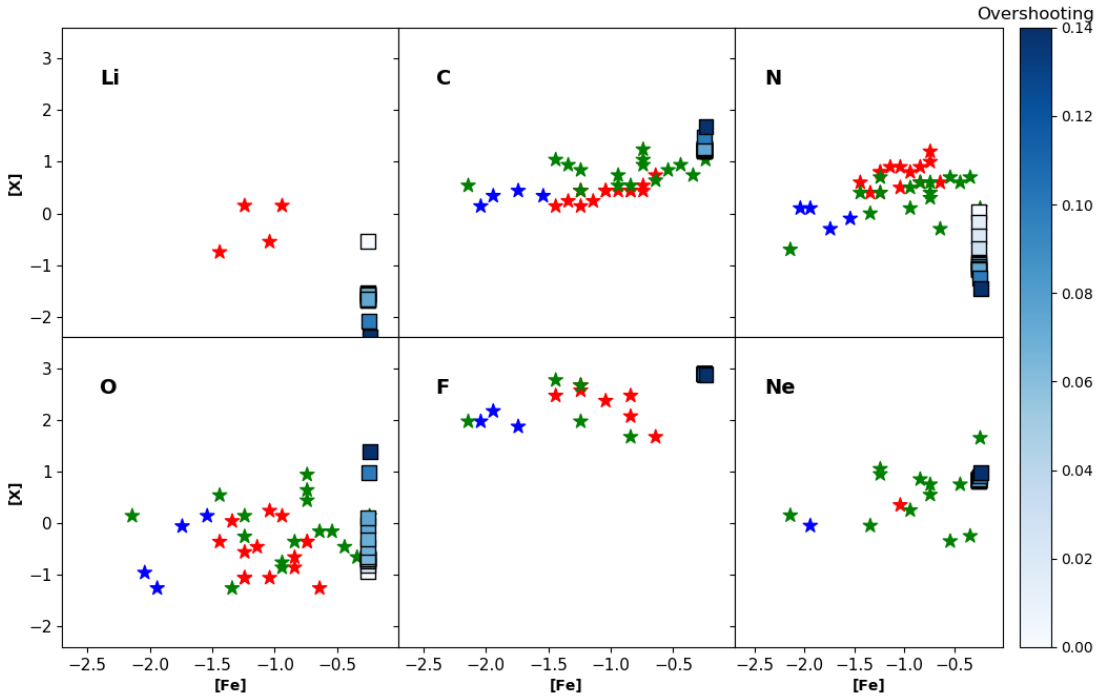

Figure 3.8. Change in some key surface elemental abundances with changing overshooting parameter "`overshoot_f`". The red stars are RCB majority observations (homogeneous in terms of chemical composition), the blue stars are RCB minority observations (diverse in terms of chemical composition), and the green stars are Extreme Helium star (EHe) observations. The units of composition are calculated using Equation 2.12.

not include nucleosynthesis. By varying this parameter, we are analyzing the effects of more or less hydrogen burning during the dynamical phase of the merger, assuming the energy generation does not significantly alter the structure of the star.

As expected, the surface abundance of ^{7}Li goes down with an increasing hydrogen abundance via $^{7}\mathrm{Li}(p,\alpha)^{4}\mathrm{He}$. Also, there is a large increase in ^{16}O accompanied by a significant decrease in ^{18}O between the models with initial H mass fractions of 10^{-4} and 10^{-3}. The decrease in ^{18}O can be attributed to the enhancement of proton capture reactions on both ^{14}N (slightly starving the α-capture reaction) and ^{18}O. The increase in ^{16}O is also due to the enhancement of the proton capture rate on ^{14}N. This is clear by the enhancement in ^{15}N in the burning region of the higher hydrogen abundance model, which indicates $^{14}\mathrm{N}(p,\gamma)^{15}\mathrm{O}(\beta^{+})^{15}\mathrm{N}$ is active. From there, the CNO cycle can branch into $^{15}\mathrm{N}(p,\gamma)^{16}\mathrm{O}$ or $^{15}\mathrm{N}(p,\alpha)^{12}\mathrm{C}$ (which can then α-capture or start another CNO cycle). The increase in ^{16}O and the decrease in ^{18}O explain the sudden decrease in ^{22}Ne, seen in Figure 3.10, as they starve the $^{14}\mathrm{N}(\alpha,\gamma)^{18}\mathrm{F}(\beta^{+})^{18}\mathrm{O}(\alpha,\gamma)^{22}\mathrm{Ne}$ reaction chain of the initial ^{14}N α-capture.

3.1.4 NuGrid Post-Processing

Finally, this section discusses post-processed nucleosynthesis on a much larger nuclear network containing 1093 isotopes and over 14,000 reactions. We chose two models, one with

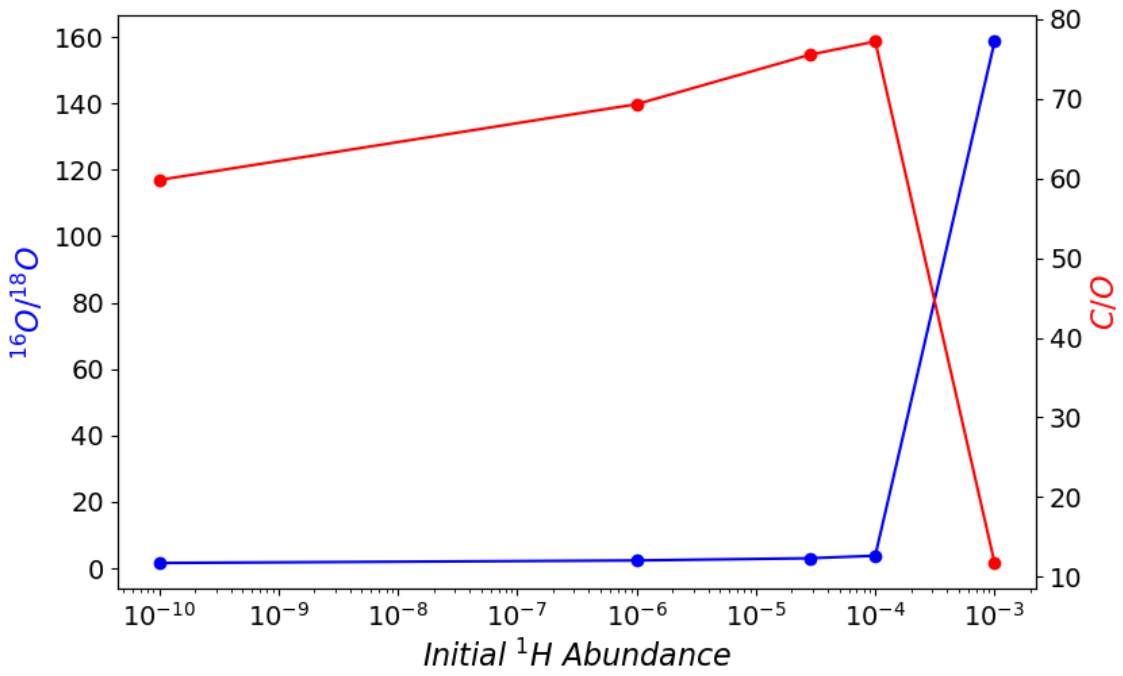

Figure 3.9. The change in isotopic ratios C/O and ^{16}O/^{18}O with changing initial hydrogen abundance in the He envelope. 10^{-99} and 10^{-20} are not shown here to maintain the scale on the x-axis. The results of those models are shown in Table 2.1.

solar and one with sub-solar metallicity, that are most consistent with previous stellar engineering attempts and observations (Models 17 and 31, respectively). Figure 3.11 shows the results of these models and the *MPPNP* post-processed results. Below we explain some of the differences between the *MESA* and *MPPNP* models, including surface Li, N, and s-process elements.

3.1.4.1 Lithium

The biggest difference between *MPPNP* and *MESA* surface abundances in Figure 3.11 is the surface abundance of ^{7}Li. This is observed in both the solar and sub-solar models. *MPPNP* burns about 6 orders of magnitude more ^{7}Li because it includes the $^{7}\mathrm{Li}(\alpha,\gamma)^{11}\mathrm{B}$ reaction while `mesa_75` does not. Typically, ^{7}Li would be burned immediately by proton capture reactions, but in both the solar and sub-solar models, there is very little initial hydrogen in the He envelope. This low amount of initial hydrogen causes other problems, specifically, in the sub-solar case where the initial hydrogen is 10^{-10} which is further discussed later.

It is important to note that in *MESA* version r12115, the default $^{7}\mathrm{Li}(p,\alpha)^{4}\mathrm{He}$ reaction has a sudden cutoff at a temperature of 10 MK. When simulating the He WD progenitor, this cutoff results in a fairly large amount of ^{7}Li in the hydrogen envelope which produces an unusually high initial abundance in the He envelope of the post-merger. In reality, the ^{7}Li should have likely been burned away during the evolution of the He WD or during the tidal disruption phase of the merger event. However, since *Octo-tiger* does not perform

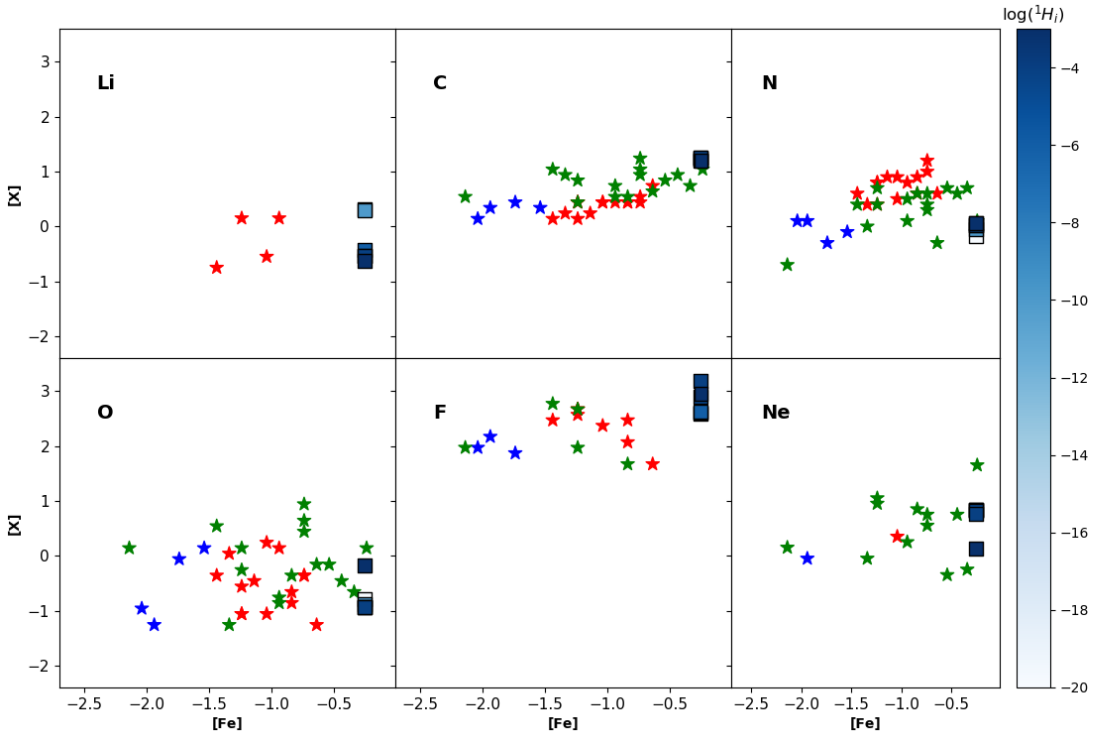

Figure 3.10. Change in some key surface elemental abundances with changing initial hydrogen abundance in the He envelope. The colored stars are explained in Figure 3.8.

nucleosynthesis or trace the species from each progenitor, the nuclear burning in the merger phase is not considered.

Given that the post-merger object in *MESA* is not burning ^{7}Li via α-capture and the initial ^{7}Li abundance should be much lower for the above reasons, we do not expect to see any measurable amount of ^{7}Li on the surface of our models. This is demonstrated by the results of the *MPPNP* post-processing and is in agreement with all but four RCB observations (Jeffery et al., 2011). It is still difficult to explain why ^{7}Li is abundant in these four observations given the expectation that it all be burned during the merger process (Clayton et al., 2007). This lithium problem is not discussed any further in this work as it is outside of our scope; however, it would be interesting for future studies to explore mechanisms that would result in a measurable abundance of ^{7}Li.

3.1.4.2 Nitrogen

The surface N abundances in *MPPNP* are consistently higher than in *MESA* and we attribute this to the burning of ^{7}Li via α-capture. ^{14}N can be created in *MPPNP* via the $^{7}\mathrm{Li}(\alpha,\gamma)^{11}\mathrm{B}(\alpha,n)^{14}\mathrm{N}$ reaction chain, while the `mesa_75` network does not contain ^{11}B. This is consistent with the fact that we see a larger enhancement of ^{14}N in the sub-solar case where there is more ^{7}Li to be burned.

It is worth mentioning that although all four models have lower surface N abundances than observations, this result is still consistent with the engineered models of Crawford

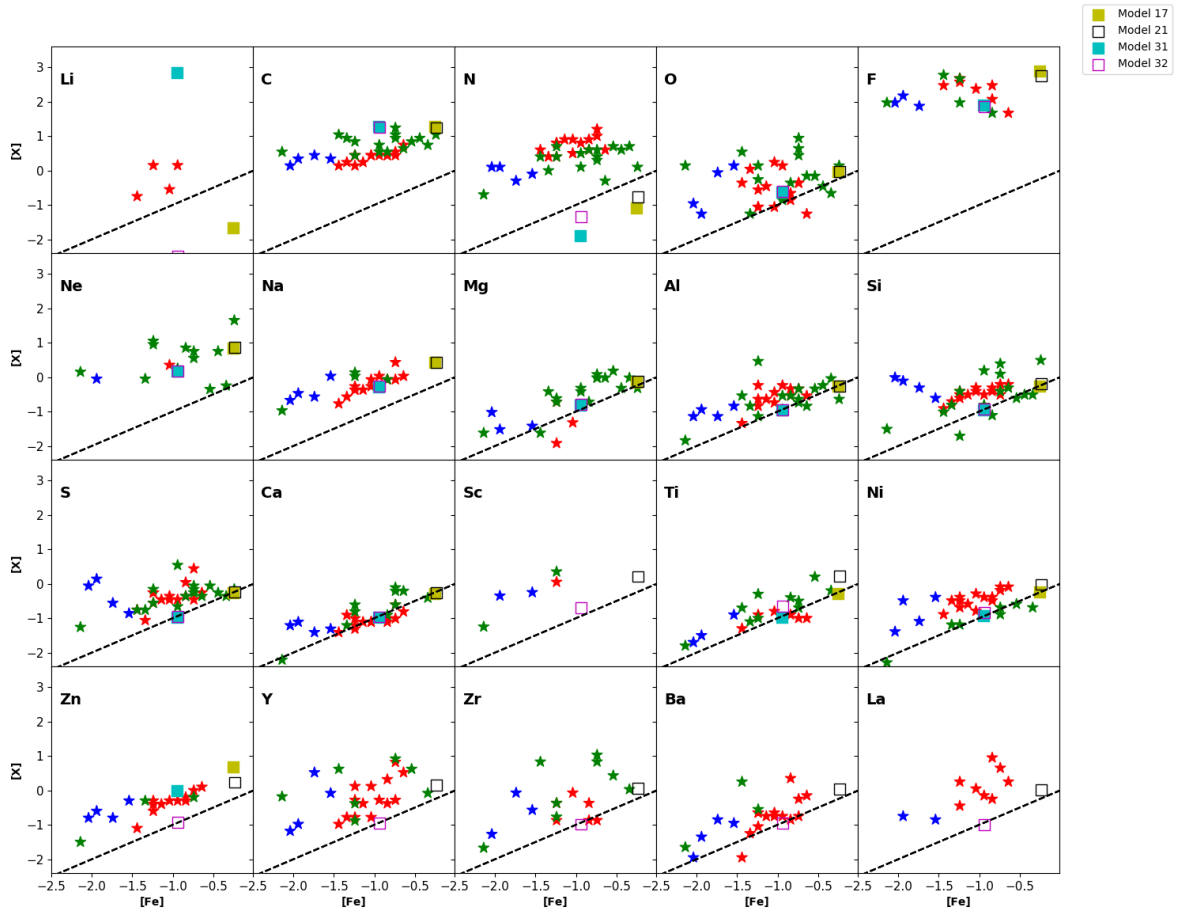

Figure 3.11. Surface Abundances calculated by *MESA* (filled in lime (solar metallicity) and cyan (sub-solar metallicity)) compared with the result post-processed by *MPPNP* (empty black (solar metallicity) and magenta (sub-solar metallicity)). The model numbers in the legend refer to the models presented in Table 2.1. The dashed black line represents scaled solar metallicities. The colored stars are explained in Figure 3.8.

et al. (2020). Their hot models (>320 MK) also show diminished ^{14}N and attribute that to enhanced α-capture. Our models reach a maximum temperature around 400 MK during the thermal adjustment of the envelope which coincides with the time where most of the nucleosynthesis takes place. This decrease in ^{14}N is also associated with a sudden burst of neutrons from the ^{22}Ne source, which becomes active above 250 MK (Käppeler et al., 2011). Following the neutron burst, ^{14}N then acts as a neutron poison and is rapidly burned by neutron capture reactions. Both enhancements in α-capture and n-capture reactions would then result in the observed enhancements of ^{18}O and ^{19}F via $^{14}\mathrm{N}(\alpha,\gamma)^{18}\mathrm{F}(\beta^+)^{18}\mathrm{O}$ and $^{14}\mathrm{N}(n,p)^{14}\mathrm{C}(p,\gamma)^{15}\mathrm{N}(\alpha,\gamma)^{19}\mathrm{F}$, respectively. ^{14}N can be replenished to observed levels by adding a higher initial hydrogen abundance to the He envelope, but as seen in Figure 3.9, this increases the oxygen isotopic ratio beyond the acceptable range.

Table 3.1. Isotopic results of all 32 models. The asterisk denotes models that were post-processed with the *MPPNP* code. Initial conditions can be found in Table 2.1.

Model	$^{16}O/^{18}O$	C/O
1	3.05	75.56
2	1.96	64.87
3	1.17	52.36
4	1.62	59.81
5	2.38	69.33
6	3.79	68.56
7	158.63	11.71
8	1.37	58.67
9	0.91	45.97
10	0.73	39.75
11	0.72	37.68
12	0.81	40.09
13	0.84	40.67
14	1.18	36.89
15	2.50	25.16
16	4.17	17.39
17	8.79	10.04
18	11.85	5.96
19	155.09	1.33
20	1444.50	4.00
21*	8.91	6.95
22	33.77	282.61
23	4.28	330.88
24	5.07	331.87
25	5.45	347.88
26	1.23	184.19
27	4.46	81.36
28	14.37	30.72
29	15.20	31.79
30	55.50	9.69
31	10.60	39.79
32*	12	26.91

3.1.4.3 s-process Elements

One characteristic of RCB stars is their enhancement in s-process elements on the surface (Jeffery et al., 2011). Previous studies in stellar engineering and our *MESA* models do not include s-process nucleosynthesis, but *MPPNP* does. Figure 3.11 shows that the solar case has a slight enhancement of s-process elements (Sc, Y, Zr, Ba, and La), but the sub-solar case does not see this enhancement. The reason we are not seeing s-process enhancement is because in both cases we have very little ^{13}C neutron source, which would be active above

a temperature of 100 MK (Käppeler et al., 2011). This is a direct result of having a lower initial hydrogen abundance as the ^{12}C being brought up from the core cannot proton capture to create ^{13}C via $^{12}\mathrm{C}(p,\gamma)^{13}\mathrm{N}(\beta^+)^{13}\mathrm{C}$. With a higher hydrogen abundance, we would expect to see more enhancement of s-process elements, but would also push the oxygen ratio outside the observed range (see Figure 3.9).

3.2 Stellar Engineering

The following section presents the resulting evolution and surface abundances of the models initialized by the stellar engineering method described in Section 2.1.2. The effects of varying the entropy transition, peak temperature, and overshooting are studied as well as post-processing models with good agreement with observations. A summary of these model parameters and results is shown in Tables 2.2 and 3.2.

3.2.1 Entropy Transition

In this parameter study, we adjust $M_{transition}$ (defined in Section 2.1.2) and observe the effects it has on surface abundances through nuclear burning or mixing efficiency. This is done by adjusting $M_{transition}$ and S_{high} such that T_{peak} remains constant and maintaining a constant initial composition. These models are labeled A1-A4 in Tables 2.2 and 3.2.

The thermal structure of these models also results in differently sized post-merger objects. Model A1 starts at a radius of about $1.02R_\odot$ while Model A4 starts off much more compact at a radius of about $0.22R_\odot$. Having both the S_{high} and $M_{transition}$ parameters allows us to effectively change either the initial radius or peak temperature while keeping the other constant. This differs from the procedure used in Lauer et al. (2019) or Crawford et al. (2020) where they only have the S_{high} parameter forcing the peak temperature and initial radius to remain coupled.

By increasing $M_{transition}$, the entropy transition happens over a larger shell as seen in the upper left panel in Figure 2.8. Furthermore, this has the effect of increasing the density of the He-burning region which results in more mass available for nuclear burning. Figure 3.12 shows the more massive He-burning region results in more nuclear energy being deposited into the envelope. This higher energy deposition results in a larger peak radius as inferred in Figure 3.13 by the virtually constant peak luminosity but decreasing effective temperatures.

The more massive SOF region also results in more nucleosynthesis processing before the material is dredged to the surface. Figure 3.14 shows the surface abundances for key elements during the RCB phase. It is clear from Figure 3.12 that in the case of $M_{transition} = 0.53M_\odot$ there is much less α-capture and thus the $^{14}\mathrm{N}(\alpha,\gamma)^{18}\mathrm{F}(\beta^+)^{18}\mathrm{O}(\alpha,\gamma)^{22}\mathrm{Ne}$ reaction chain is suppressed. By allowing for higher density material in the He-burning regime, we can enhance α-capture reactions at lower temperatures compared to what is observed in the temperature study done in Crawford et al. (2020).

The results from this study show that it is appropriate to have a steady transition from the low entropy core to the high entropy envelope. The denser He-burning region allows for more nucleosynthesis without increasing the initial temperature. This suggests that the SOF should be relatively thin while not causing too harsh of a temperature gradient as seen

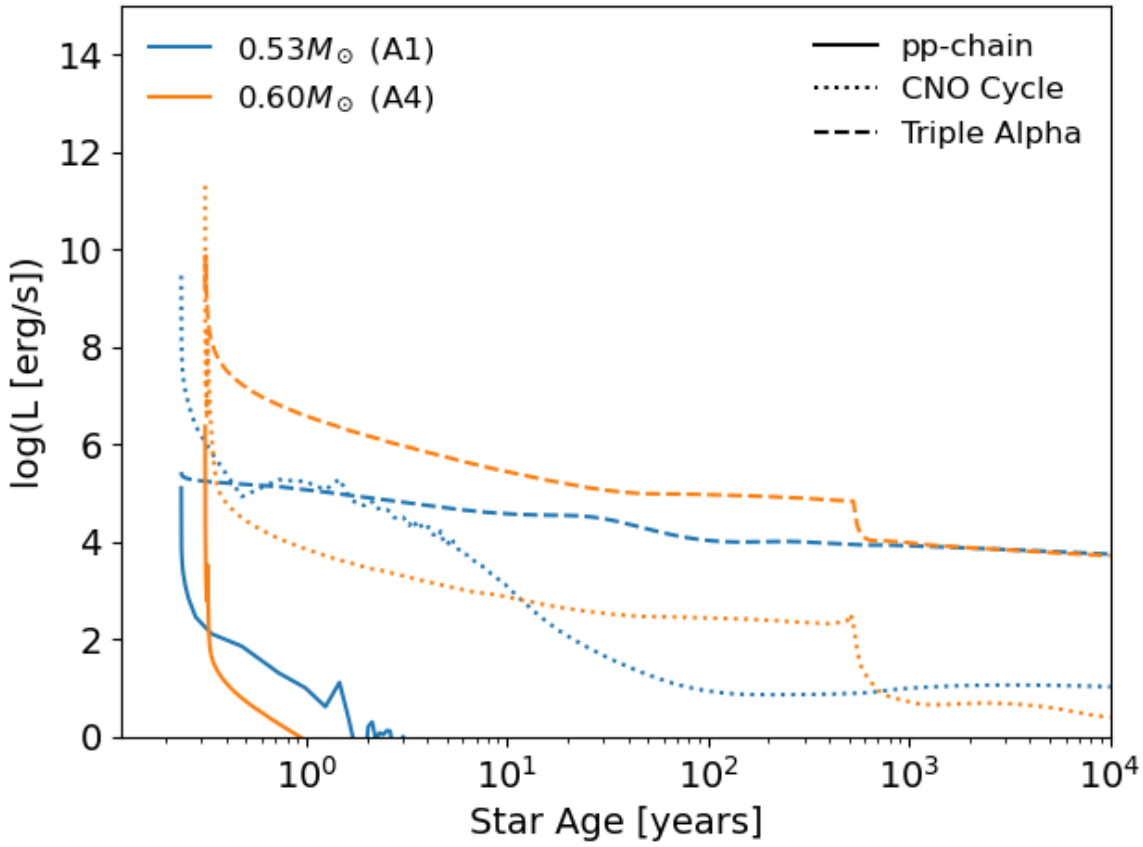

Figure 3.12. The total power output from different categories of nuclear burning for Models A1 and A4.

in Model A1. For the following parameter studies, we use $M_{transition} = 0.55M_\odot$ as it has the best agreement to observations of these four models.

3.2.2 Shell Temperature

Similar to the study done in Crawford et al. (2020), we also perform a temperature study by varying the peak temperature of Model A2 (shown in Models B1-B3). The results shown here are different from the results of Crawford et al. (2020) because of the smoother entropy transition and inclusion of material synthesized in the SOF.

The results of this study are similar to those of the entropy transition study. As the peak temperature is increased, there is a larger mass of material in the He-burning regime. However, the higher burning temperature will also cause much more rapid α-capture as well as a larger mass of burning material. This results in a much larger range of surface abundances seen in Figure 3.15. In the case of $T_{peak} = 181MK$ (Model B1), there are two contributing factors to the much higher oxygen isotopic ratio as seen in Table 2.2. First, the lower temperature makes the $^{14}\mathrm{N}(\alpha,\gamma)^{18}\mathrm{F}$ reaction roughly two orders of magnitude slower than in Model B2. Secondly, this lower peak temperature and the larger initial radius seen in Figure 2.9 causes a temperature gradient that is not quite sufficient near the shell to induce

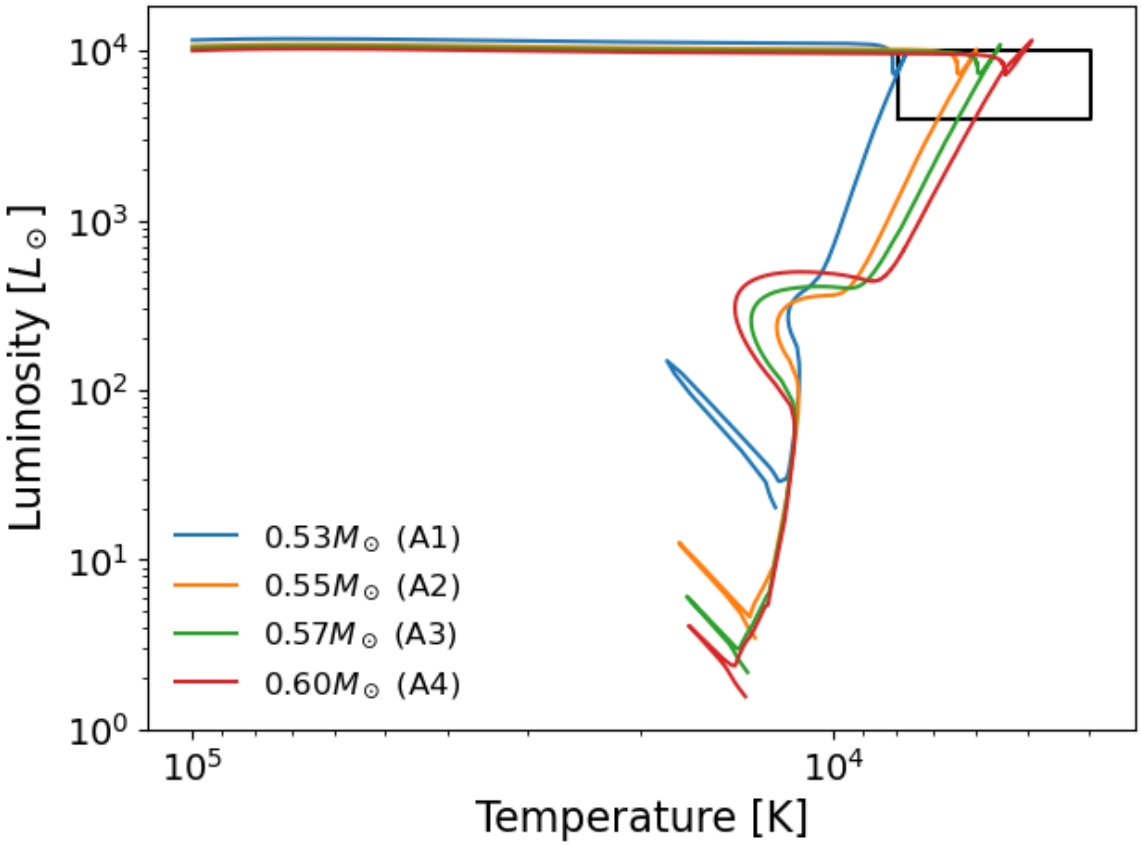

Figure 3.13. HRD for models with varying $M_{transition}$. The black box represents the range of surface luminosity and temperature measurements for observed RCB stars (Tisserand et al., 2009, 2011).

convective mixing to the surface as in the other models. Thus, the surface abundances remain relatively unchanged from that of the He-WD progenitor and there is no measurable presence of ^{18}O. This also allows for the initial abundance of ^{7}Li to remain at the level of the few observed outliers, but ultimately does not match the observations of most other heavier elements. Furthermore, the models with higher temperature have more nuclear energy input in the envelope and expand to larger radii during the RCB phase as inferred by Figure 3.16.

The results of this study show that a temperature of $T_{peak} = 253MK$ yields the best results for this method. This is lower than the subsolar metallicity model of Crawford et al. (2020), which has a best temperature of $T_{peak} = 302MK$. The reason for this is likely due to the higher density in our SOF. As shown in Figure 3.15, higher temperatures result in more α-capture from ^{14}N and ^{15}N. This is necessary for the synthesizing of ^{18}O and ^{19}F, which are both enhanced in RCB stars. However, if the shell temperature is too large, N begins to drop below observations. Thus, there is a balance between synthesizing enough N to enhance F and ^{18}O while not burning away too much N via α-capture. The models of Crawford et al. (2020) were not able to achieve this balance as their optimal model burns too much N. Although that balance was not achieved in this parameter study, we notice a higher

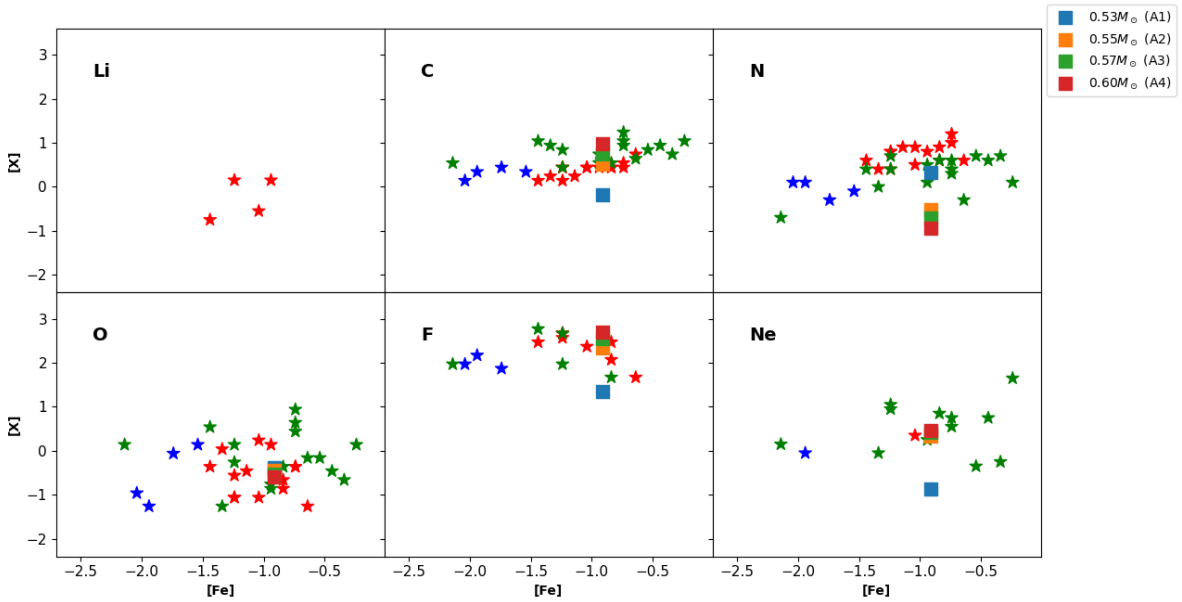

Figure 3.14. Surface abundances for models with varying $M_{transition}$ (Models A1-A4 in Table 2.2). The red stars are observed RCB majority stars (homogeneous chemical compositions), the blue stars are observed RCB minority stars (diverse chemical compositions), and the green stars are Extreme Helium star (EHe) observations. The units of composition are calculated using Equation 2.12.

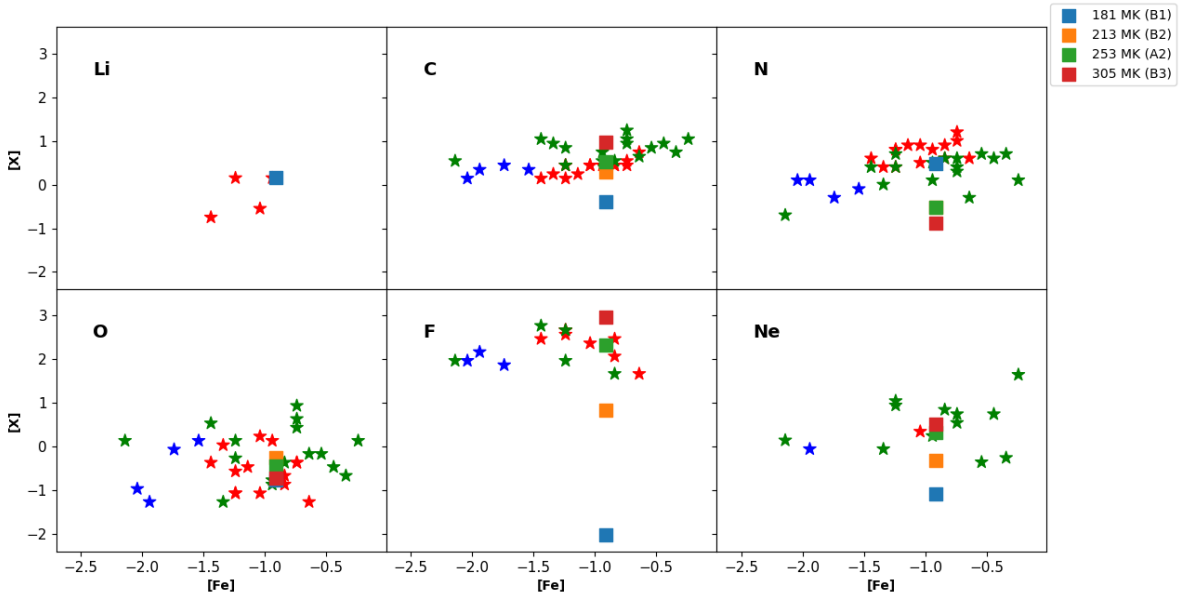

Figure 3.15. Surface abundances for models with varying T_{peak} (Models B1-B3 in Table 2.2). The data plotted with star symbols are explained in Figure 3.14.

amount of N on the surface during the RCB phase compared to the model of Crawford et al. (2020).

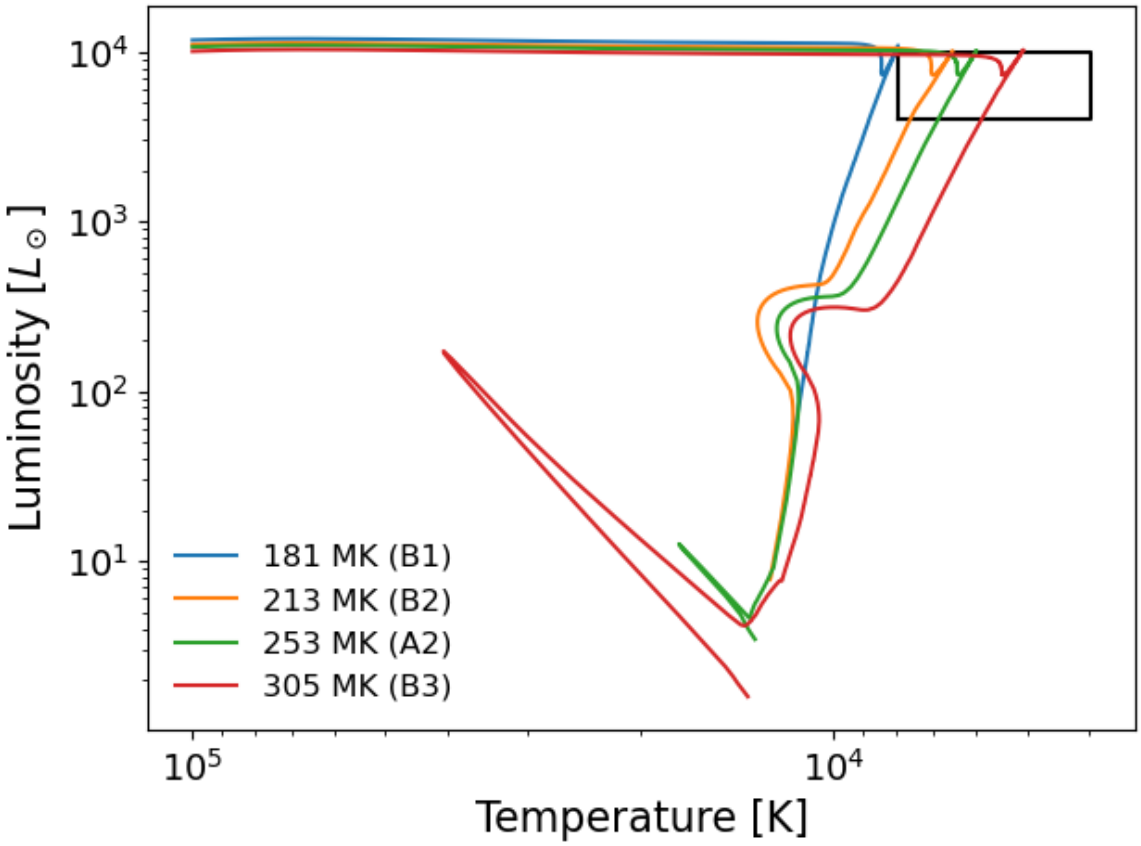

Figure 3.16. HRD for models with varying T_{peak}. The initial transient for the higher temperature cases is due to the reaction of the surface to the sudden input of nuclear energy when evolution begins and only lasts around 100 days.

3.2.3 Overshooting

Previous works have suggested that overshooting may need to be included in order to obtain results that match the s-process observed in AGB stellar evolution (Herwig et al., 2003). Although RCB evolution is slightly different, it still includes a He-burning shell above a region rich in ^{12}C. Overshooting and rotationally induced mixing become necessary components in order to bring free protons and ^{12}C together in the burning region, thus igniting the $^{12}\mathrm{C}(p,\gamma)^{13}\mathrm{N}(\beta^+)^{13}\mathrm{C}$ reaction chain. This will create the ^{13}C neutron source required for s-process in the burning region.

The mapped models in the previous section utilize overshooting as a means to change the surface abundances during the RCB phase. In those models, the change in the overshoot parameter in all regions causes a slightly lower level of N and ^{18}O as overshooting becomes more efficient. This is likely due to the bridging of the convective gap for longer periods of time causing more nucleosynthesis to occur before disconnecting the He-burning shell from the surface.

In this parameter study, we include overshooting beneath the He-burning shell and vary the strength of overshooting via the `overshoot_f` parameter included in *MESA* (values we

use can be found in Models C1-C3 in Table 2.2). We only consider overshooting beneath the He-burning region in the hopes of enhancing the s-process by bringing more ^{12}C and protons together in the burning region. As noted in the previous section, overshooting within a reasonable range does not appear to affect the nucleosynthesis of other elements to a large degree. We use the exponential overshoot scheme where `overshoot_f` is a parameter that controls the extent beyond the convective zone that overshooting will reach (Paxton et al., 2011).

The results in Figure 3.17 show that overshooting does not have a big impact on the surface abundances. However, when the overshooting begins to extend into the CO core, it will rapidly dredge up material rich in ^{12}C and ^{16}O. This has the effect of increasing the ^{16}O/^{18}O ratio to levels outside the range observed in RCB stars. Furthermore, Figure 3.18 shows that when the ^{12}C and ^{16}O rich material is dredged to the envelope, the star suddenly expands to a much larger radius than it would otherwise. This is due to the increased opacity in the envelope during the expansion phase.

Because we get sufficient ^{12}C and ^{13}C included in the envelope by inclusion of nucleosynthesis from the dynamical merger phase, overshooting is not required to enhance the surface abundances to be in agreement with observed levels. This happens because there is some fraction of material from the accretor in the SOF which is then fully mixed in the envelope after nuclear processing (More discussion on this later).

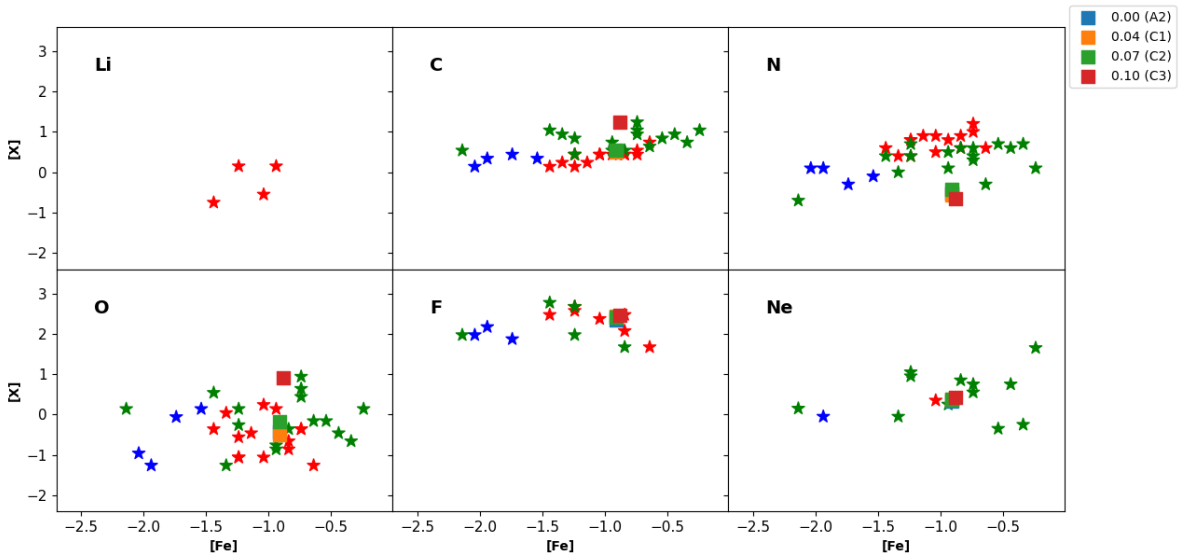

Figure 3.17. Surface abundances for models with varying `overshoot_f` (Models C1-C3 in Table 2.2). The data plotted with star symbols are explained in Figure 3.14.

3.2.4 MPPNP

After performing a range of studies on the free parameters available in these models, we follow up by choosing which models to post-process in MPPNP. A model is chosen based on how well the surface abundances match RCB observations and the neutron exposure in the SOF calculated using Equation 2.13 (See Section 2.3). Based on those criteria, Model A2 is

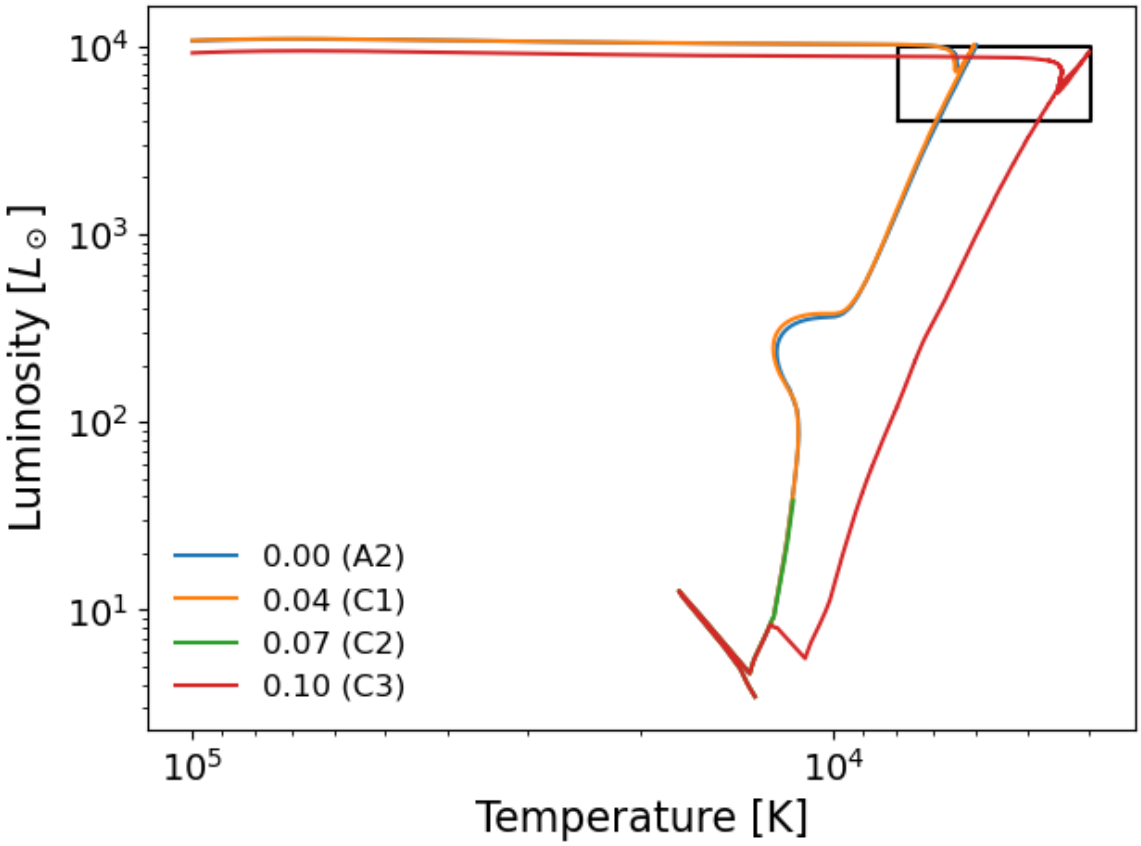

Figure 3.18. HRD for models with varying `overshoot_f`.

the best model to post-process in *MPPNP* because it agrees well with surface abundances (Figure 3.14), isotopic ratios (Table 2.2), and has a sufficiently high neutron exposure in the burning region (Figure 3.19).

After post-processing model A2, we get the surface abundances shown in Figure 3.20 and isotopic ratios shown in Table 2.2. We see good agreement in most surface abundances and isotopic ratios, but no enhancement in s-process elements. A closer look at the composition of Model A2 shows that the initial $^{13}C/^{14}N$ ratio is 0.001 after combining the SOF zone with the envelope. Most of the ^{13}C neutron source had been burned during the single zone nucleosynthesis, which resulted in a large initial density of neutrons in the *MESA* model. Those neutrons were then immediately absorbed by $^{14}N(n,p)^{14}C$ as well as any further neutrons generated during the post-merger evolution.

Staff et al. (2018) finds that for SPH simulations, the amount of accretor material dredged up during the merger is not as exaggerated as the grid based simulations. For their model with a mass ratio of 0.7, they calculate there is about 0.01-0.02$M_\odot$ of accretor material in the envelope. Furthermore, their earlier paper calculates the SOF has a total mass of roughly 0.1$M_\odot$ for a mass ratio of 0.7 (Staff et al., 2012). Therefore, we estimate that in the SPH calculations, there is roughly 10% accretor material in the SOF of a 0.7 mass ratio post-merger object. As shown in Table 2.2, Model A2 only had 4% accretor material in the

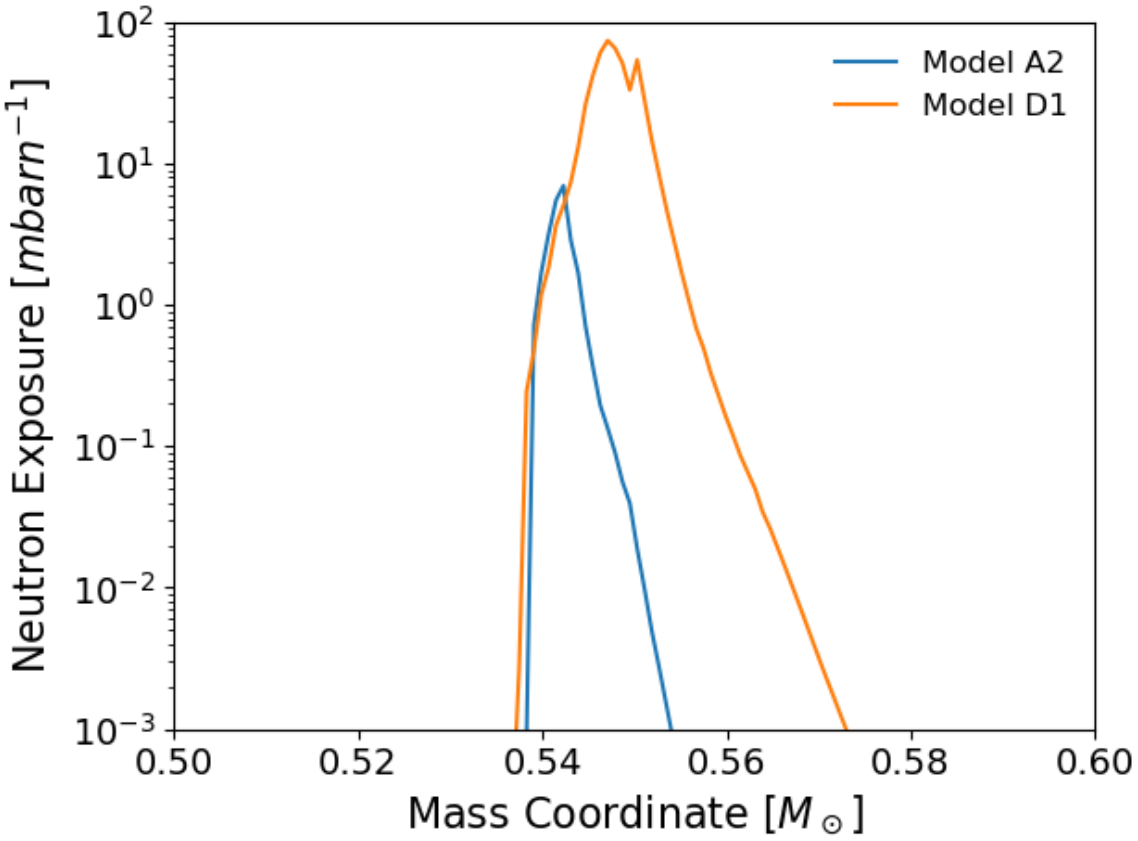

Figure 3.19. Neutron exposure (calculated using Equation 2.13) for the A2 and D1 models. The time integration is done from the start of the *MESA* simulation until the split of the convection zone.

envelope. In order to better match this rough estimate from the SPH simulation, we double the amount of accretor material in the SOF to 8% which is labeled Model D1 in Table 2.2. Including this larger source of ^{12}C in the SOF means the $^{12}\mathrm{C}(p,\gamma)^{13}\mathrm{N}(\beta^{+})^{13}\mathrm{C}$ reaction will absorb all of the protons before ^{13}C has a chance to capture the remaining protons during the single zone burner phase. This has the effect of raising the initial $^{13}\mathrm{C}/^{14}\mathrm{N}$ ratio in the envelope ($\simeq$0.82) and should allow for more s-process nucleosynthesis to take place.

The neutron exposure for Model D1 is shown in Figure 3.19. This neutron exposure is much higher than what is seen for Model A2 and appears much more representative of what one would expect from the i-process (Denissenkov et al., 2018). Furthermore, the initial neutron densities peak between 10^{14} and 10^{15} cm^{-3} which is also consistent with i-process nucleosynthesis. As expected, Figure 3.20 shows Model D1 has a large enhancement in s-process elements and agrees with observations in most other surface abundances and isotopic ratios. The level of s-process enhancement in this model seems higher than observations, but this can be reduced slightly by decreasing the amount of accretor material in the SOF.

We note that the ^{14}N surface abundance is a bit lower than observations suggest. However, a closer look at the surface abundances as a function of star age reveals an important feature

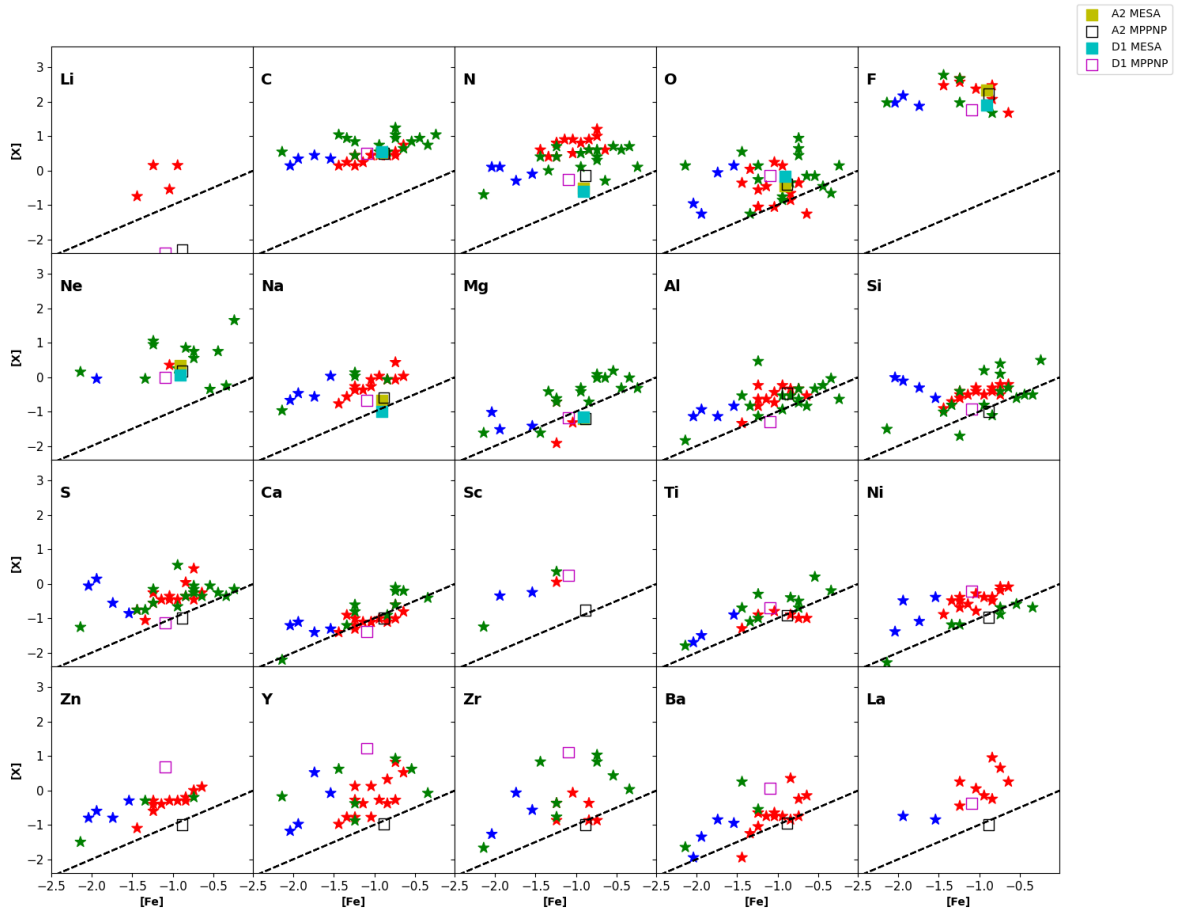

Figure 3.20. The surface abundances of Models A2 and D1 during the RCB phase along with the results from the *MPPNP* post-processing. The data plotted with star symbols are explained in Figure 3.14.

(Figure 3.21). Most ^{14}N that is burned via neutron capture will undergo the $^{14}\mathrm{N}(n,p)^{14}\mathrm{C}$ reaction. However, ^{14}C is unstable with a half-life of 5730±40 years and will beta decay back to ^{14}N (Godwin, 1962). Because the RCB phase at which we analyze the surface abundances of our models occurs after roughly 1000 years, most of the ^{14}C had not had sufficient time to decay. Given sufficient time, the ^{14}N grows by roughly one dex before leaving the RCB box after roughly 100,000 years. This increase in surface ^{14}N brings the model into agreement with observed values. Furthermore, we note that during this time the other isotopes remain virtually unchanged due to the gap in convective mixing between the He-burning region and the surface.

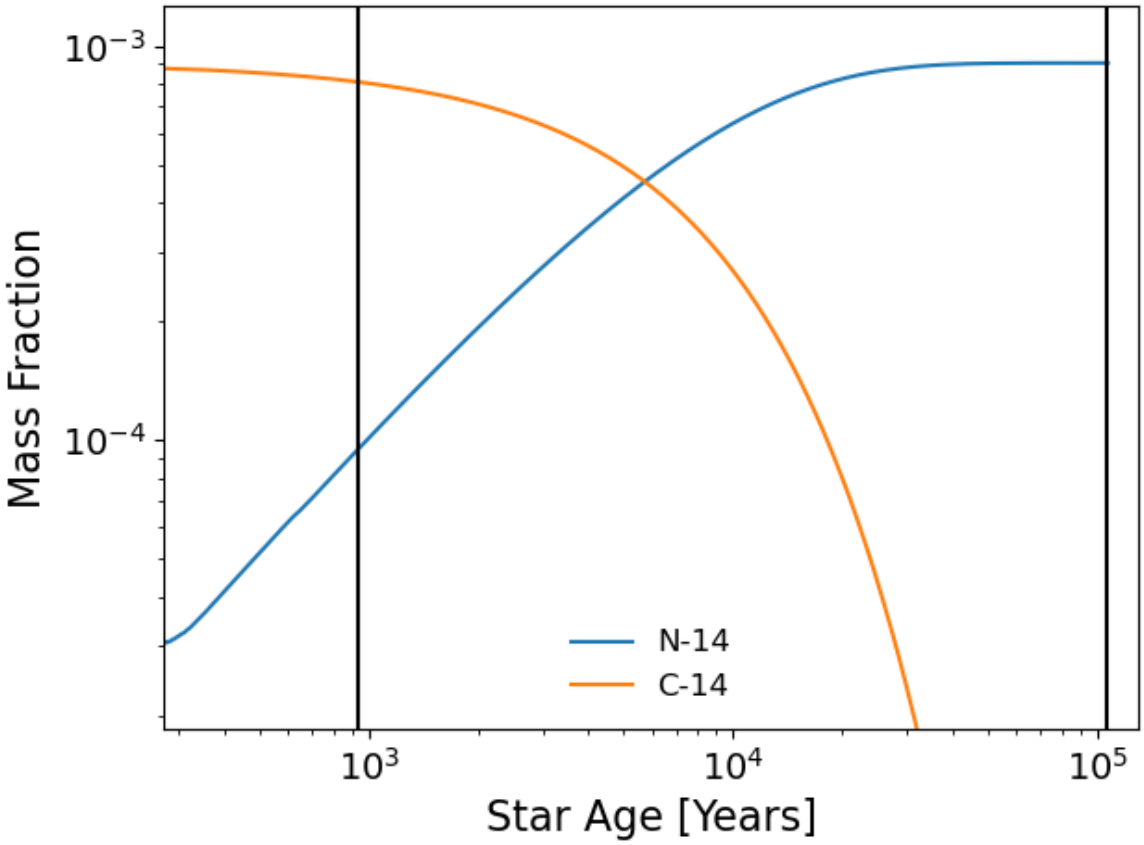

Figure 3.21. The mass fraction of ^{14}C and ^{14}N in the photosphere as a function of star age for Model D1. The vertical black lines represent when the star enters and then leaves the RCB box (seen in Figures 3.13, 3.16 and 3.18).

Table 3.2. The results of the parameter study performed on engineered models. Initial conditions can be found in Table 2.2.

Model	^{16}O/^{18}O	C/O
A1	1.17	0.78
A2	1.71	4.54
A2 MPPNP	1.22	2.95
A3	3.9	9.46
A4	8.89	17.92
B1	>1000	1.12
B2	1.09	1.73
B3	9.05	23.23
C1	2.57	5.05
C2	9.2	2.83
C3	185.35	1.03
D1	8.82	1.9
D1 MPPNP	6.32	1.64

CHAPTER 4.
EXTENDING THE FRAMEWORK: ANALYSIS OF BETELGEUSE

Chapter 2.1.1 introduces a framework for mapping the post-merger object of a 3D hydrodynamics code into a spherical stellar evolution code. This method is applied in the context of RCB stars and their surface properties are compared to observations as a test of validity of the proposed evolutionary channel. For RCB stars, the progenitor merger is between two white dwarf stars. However, *Octo-Tiger* is also capable of simulating mergers between main sequence and giant stars using (Marcello et al., 2016). Therefore, this 3D to 1D mapping method can be used to simulate the post-merger evolution of a wider variety of binary stars. In this chapter, we describe the use of this method in an attempt to reproduce the observed properties of the red supergiant, α Orionis (popularly known as Betelgeuse).

4.1 Background

Betelgeuse has been discussed as a star that has suffered a past merger, mainly due to its abnormally high surface rotation velocity. The surface rotation of Betelgeuse is measured to be between 5-15 km s^{-1} (Gilliland & Dupree, 1996; Uitenbroek et al., 1998), which is much higher than what would be reasonably expected from single star evolution on the red supergiant branch (RSB) (Wheeler et al., 2017). Wheeler et al. (2017) propose that this enhanced surface rotation may be a consequence of a merged binary system, which is supported by the estimate that roughly 19 percent of apparently single massive stars are actually the product of a merger event (de Mink et al., 2014). Chatzopoulos et al. (2020) further explore this possibility by using analytical expressions to perturb the envelope of a giant star within a parameter space and analyze the resulting evolution with *MESA*. Their grid of models explores the initial masses of the primary and secondary, the initial rotation rate of the primary, and the Roche-Lobe overflow radius of the primary. They find that within the parameter space they explored, most of their models reasonably match the surface rotation on the RSB observed for Betelgeuse. They also make note of another scenario in which the spin-up occurs due to an accretion phase of a more massive star onto a less massive star. Though they cannot rule this possibility out, we do not consider it here as it cannot be modeled with our current framework.

On top of an enhanced surface rotation, Betelgeuse also exhibits an enhancement in ^{14}N and a slight deficiency in ^{12}C compared to that of an unevolved star (Lambert et al., 1984). The specific values of ϵ_C, ϵ_N, and ϵ_O are 8.4, 8.6, and 8.8, respectively, with reported errors of about 0.15 dex (Lambert et al., 1984). These values are calculated by the typical formula:

$$\epsilon_i = \log(X_i/X_H\mu_i) + 12 \tag{4.15}$$

X_i is the mass fraction of element i, and μ_i is the mean molecular mass of element i. This is typically indicative of CN-processed material being dredged up to the surface through some enhanced interior mixing. Since Chatzopoulos et al. (2020) focus on the surface rotation, they do not analyze the surface abundances. However, they do make a comparison of composition to observations in a later conference (Chatzopoulos, 2020). Dolan et al. (2016) run models

constrained by the surface temperature, luminosity, and abundance as well as mass loss and analyze the surface abundaces, but do not focus on the rotation. Their nonrotating models see a good match to observations for a progenitor mass of around $20M_{\odot}$. Luo et al. (2022) explore models with varying initial masses, overshoot coefficients, and rotation rates. They focus on the surface composition and see a good match to observations for masses above $15M_{\odot}$ and relatively small overshooting. However, they find that their faster rotating models begin to have surface abundances that do not match observations and none of their models are able to sustain such a high rotation rate on the RSB. These findings further support the idea that Betelgeuse is unlikely to have evolved from a single star, but had some kind of binary interaction that spun up the surface as the primary was leaving the main sequence.

Following up on the models of Chatzopoulos et al. (2020), we present a model that starts with a binary system in *Octo-Tiger* and is then mapped into *MESA* using similar methods to those described in Chapter 2.1.1. In this study, we attempt to match the observed surface rotation as well as the surface abundances observed in Betelgeuse.

4.2 The Initial Model

4.2.1 The Binary

Since this work directly follows up on the work done in Chatzopoulos et al. (2020), we make use of the initial parameters in one of their models. This model is a $16{+}4M_{\odot}$ system containing a lower mass main sequence star and a higher mass star that is evolving off of the main sequence. The initial thermal structure of the primary in *Octo-Tiger* is initialized by evolving a $16M_{\odot}$ star in *MESA* and using a bipolytropic EoS in order to obtain a best fit of the temperature and density by varying the polytropic indices of the core and envelope. The comparison of the primary in *MESA* and *Octo-Tiger* can be seen in Figure 4.1.

The comparison in Figure 4.1 is made with a $16M_{\odot}$ *MESA* model that has left the main sequence and expanded to a radius of $50R_{\odot}$. This is the radius we are using for the primary Roche-Lobe when Roche-Lobe overflow is initiated. The majority of the envelope has a relatively good match despite the two codes using a differing EoS. However, because the core has very little resolution in *Octo-Tiger*, we see that both the density and temperature are about an order of magnitude lower than the central (core) regions in the original *MESA* model. Unfortunately, the differing scales of the size of the core compared to the envelope of the giant star makes it unfeasible to adequately resolve the core and run the binary merger model at the same time. This difference puts the core temperature of the *Octo-Tiger* model below the limit for He-burning, which is crucial to the post-merger evolution. Our solution to this problem will be explained later in this chapter.

The grid we use in *Octo-Tiger* starts with 64^3 cells and has a maximum of 9 further levels of refinement for the secondary and 7 levels of refinement for the primary. The reason for allowing more refinement of the secondary is because at this extreme mass ratio, we must adequately resolve the much smaller secondary without over-resolving the primary thus costing too much in computational resources. The initial separation is $100R_{\odot}$ and the initial orbital period is about 26 days and the total domain size of the simulation is about $4000R_{\odot}$. The primary is roughly 200 cells across and the secondary is roughly 33 cells across. Figure

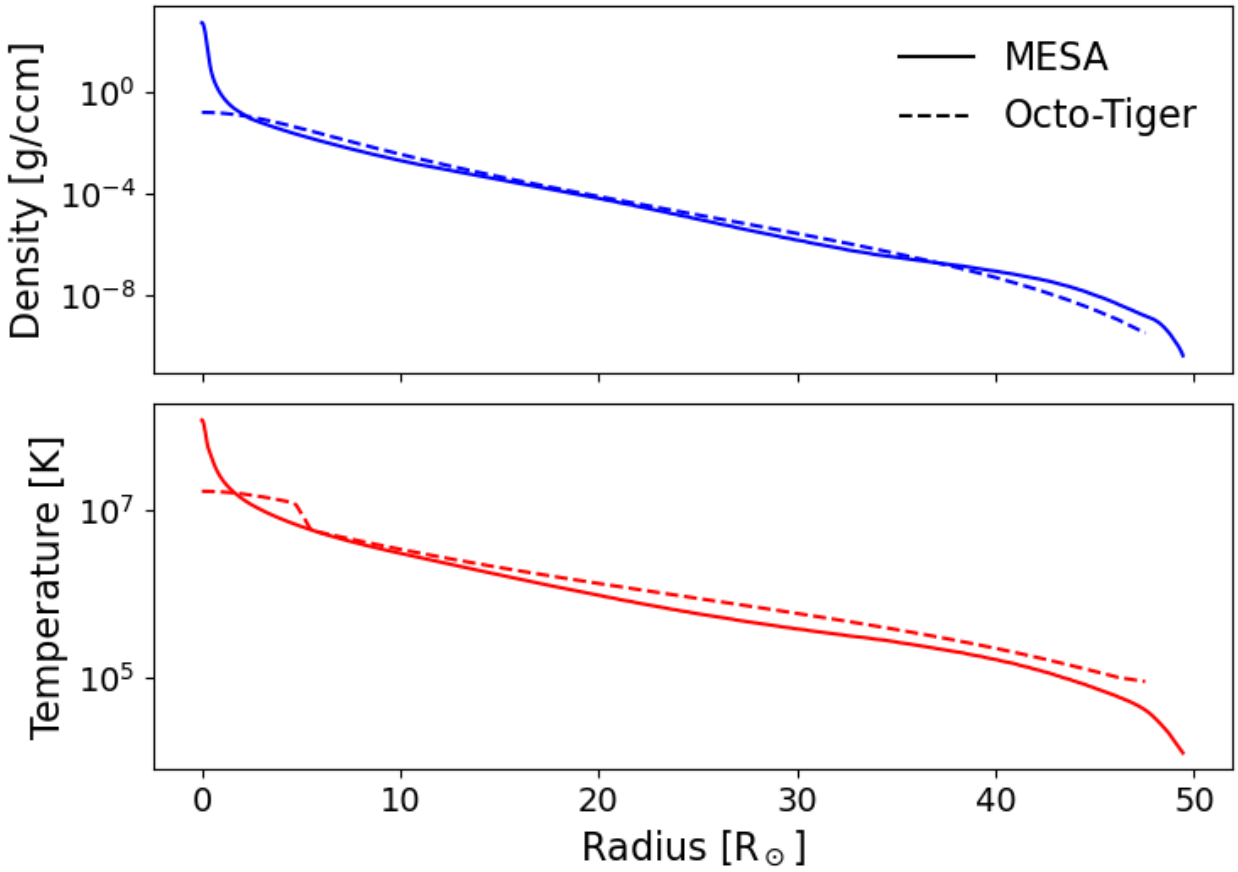

Figure 4.1. A comparison of the density (upper) and temperature (lower) profiles between the *MESA* primary (solid lines) and the spherically averaged *Octo-Tiger* primary (dashed lines).

4.2 shows a slice along the equatorial plane of the density at the initial state of the binary. In order to force this system to merge on a reasonable timescale, we implement a user defined angular momentum loss routine of 1 percent per orbit until the secondary becomes tidally disrupted and coalesces in the envelope of the primary (around 46 initial orbital periods) which uses about 5 million cpu hours. Although it is necessary to perform this driving, it does mean there will be a loss of about 37 percent of the total angular momentum just from this driving, some of which is expected in a merger due to effects such as magnetic braking and mass loss.

4.2.2 Relaxation Post-Merger

After 46 initial orbital periods with the user defined angular momentum removal, the two stars merge. By the time the merger occurs, there was a loss of nearly 50 percent of the original orbital angular momentum from driving, mass loss, and a small part being transferred to spin of the primary. There was also about $0.7 M_\odot$ of material lost from the grid during the transient outburst that resulted from the merger, although most of that was unbound from the post-merger object. We allow the star to evolve in *Octo-Tiger* for about 5 more

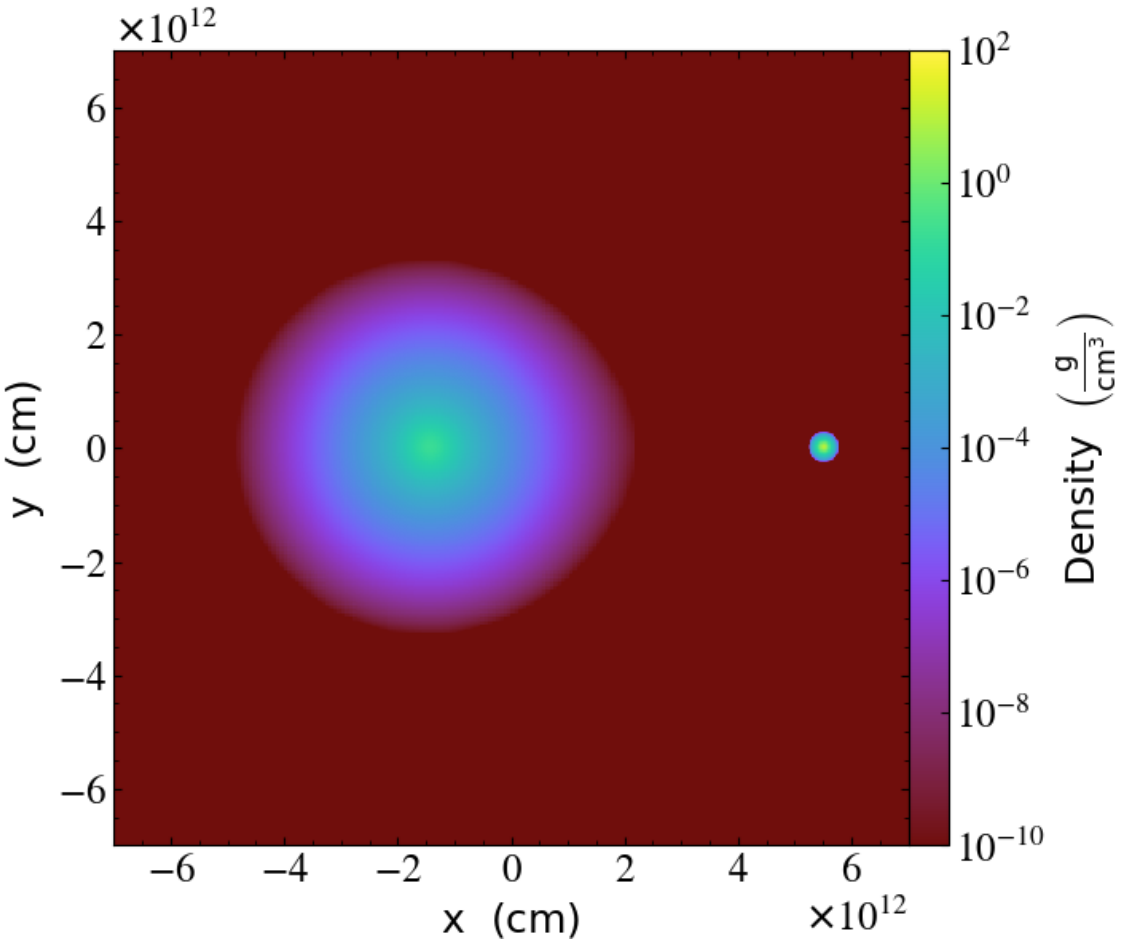

Figure 4.2. A slice plot of the initial *Octo-Tiger* density along the equatorial plane.

initial orbital periods (corresponding to 130 days) after the merger before mapping it into *MESA* in order to give the grid some time to settle. The density in the equatorial plane at this stage is shown in Figure 4.3.

As described in Chapter 2.1.1, *MESA* requires three profiles in order to initialize a star from the data obtained from *Octo-Tiger*. The first is the chemical composition, which is taken directly from the *MESA* evolved primary star used to initialize the *Octo-Tiger* thermal structure. We use the *MESA* data because *Octo-Tiger* is not designed to follow the chemical mixing and diffusion of individual species. This also builds in the assumption that the perturbation of the chemical composition in the envelope of the primary due to the merger is relatively small, which is reasonable since the secondary was a main sequence star with a similar abundance.

The second required profile is the angular momentum, which is taken directly from *Octo-Tiger* in cylindrical averages around the center of mass using equations 2.7 and 2.9. The method is described in more detail in Chapter 2.1.1. It is worth noting here that the input angular momentum profile could vary within a factor of two due to the necessary angular momentum driving and mass loss from the grid. Also, the distribution of angular momentum

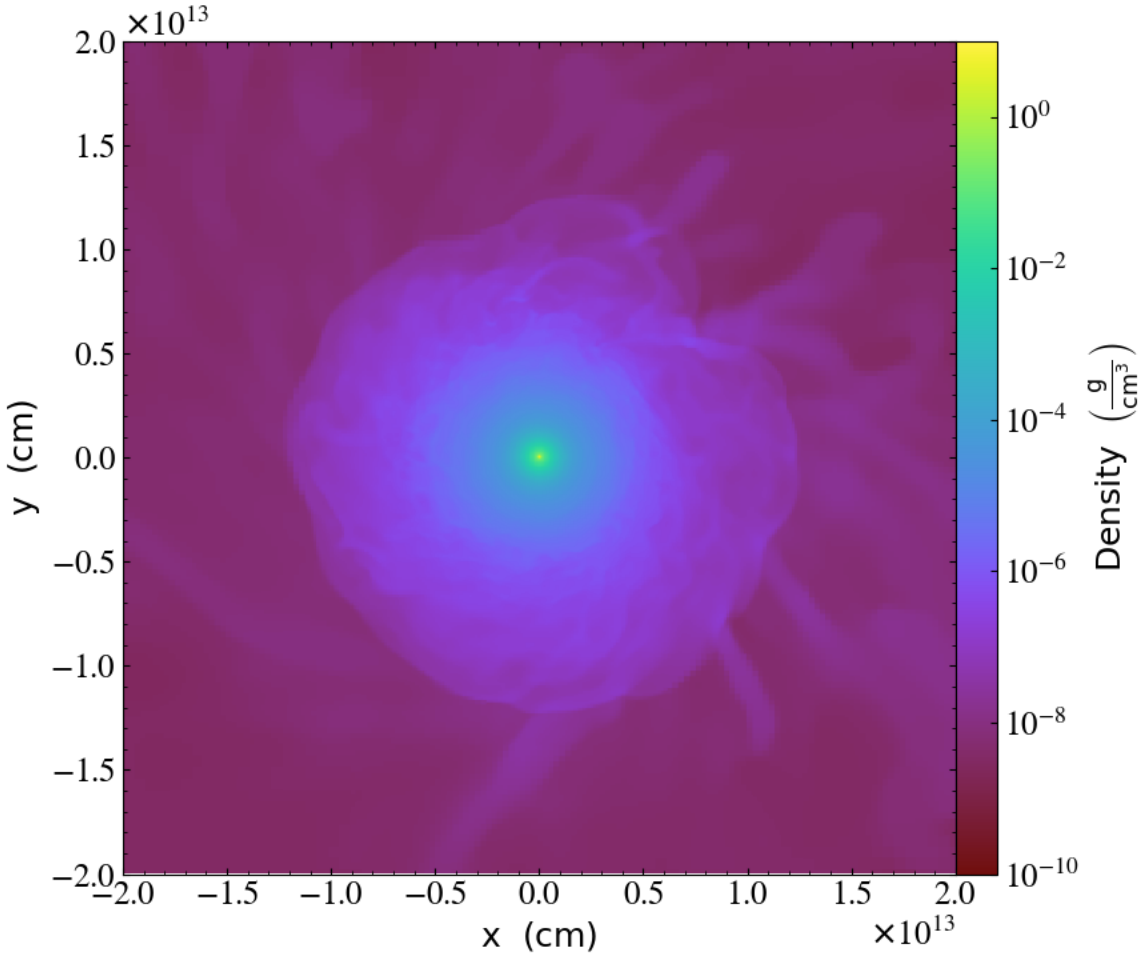

Figure 4.3. An equatorial slice of the post-merger 5 initial orbits after the dynamical merger event.

would be mostly concentrated near the equator from the merger, however since *MESA* is a 1D code, the total angular momentum at each radius is instead spread over an entire shell.

The last required profile is the entropy, which was calculated during the *MESA* relaxation based on the temperature and density in Chapter 2.1.1. However, as previously noted, the temperature of the core is unreliable in *Octo-Tiger* and is even insufficient for He-burning. Figure 4.1 shows the order of magnitude difference in the core temperature and density of the primary between *Octo-Tiger* and *MESA*. However, for the purposes of this study, it is important to retrieve information about the perturbation of the thermal profile in the envelope due to the merger event in order to track its evolution. Therefore, we calculate the entropy of the spherically averaged *Octo-Tiger* post-merger using the Helmholtz EoS with the internal energy, mass density, and an assumed mean molecular weight of 0.6, which is the mean molecular weight of a solar composition. This calculated entropy for the envelope is then combined with the *MESA* evolved entropy for the core of the primary to obtain an entropy profile with an unperturbed core and a perturbed envelope due to the merger. This combination of entropy profiles can be seen in Figure 4.4. The transition between the core

and envelope is chosen around a normalized exterior mass coordinate (q) of 0.5 because it is the outermost large composition gradient as indicated by the vertical portions of the orange line.

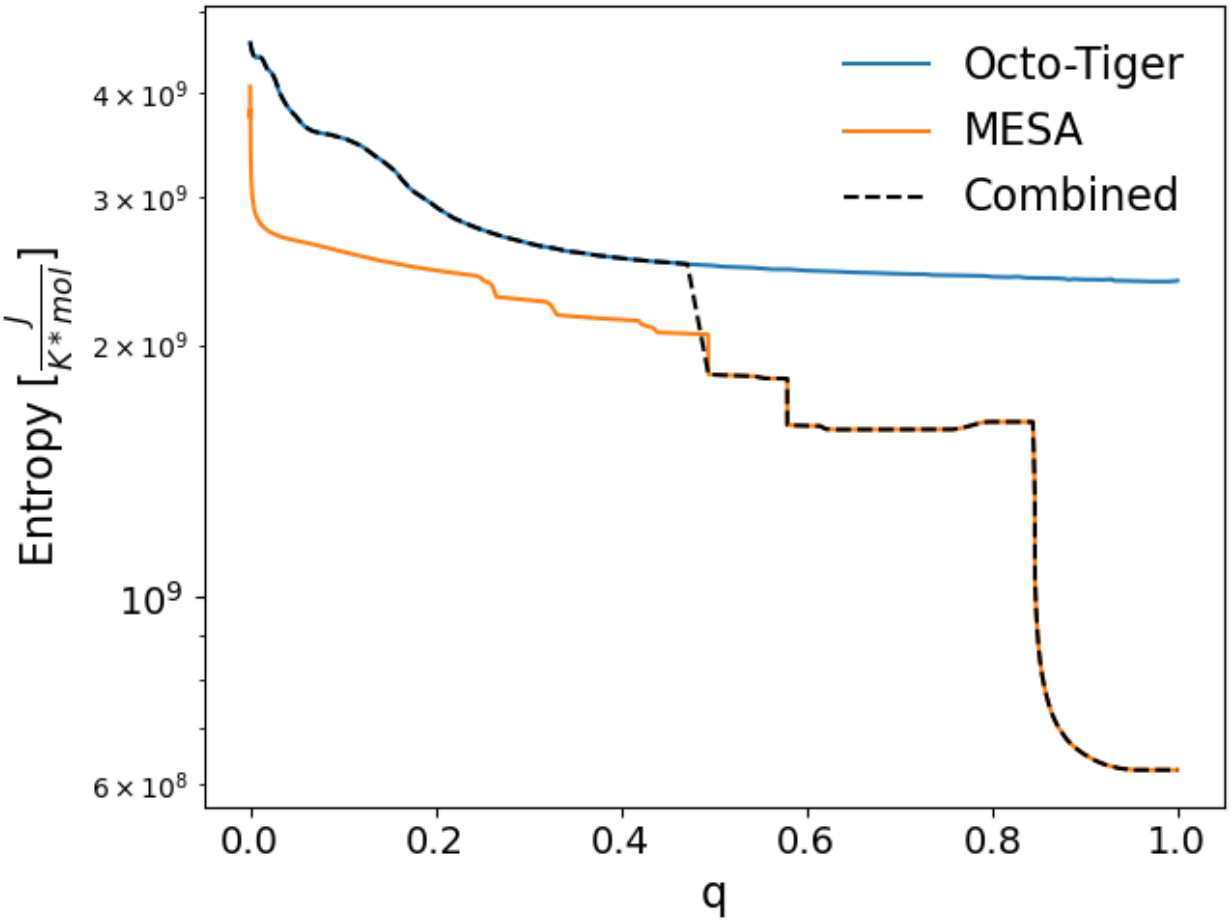

Figure 4.4. An entropy profile showing the entropy of the post-merger object calculated in *Octo-Tiger* (blue solid line) and the primary evolved in *MESA* (orange solid line) and the combination of the *MESA* core and *Octo-Tiger* envelope (black dashed line). The x-axis variable "q" is the normalized exterior mass coordinate.

Once we calculate the three necessary profiles, we can use the relaxation procedures in *MESA* to create a single star with the same structure as our post-merger object. Figure 4.5 shows the comparison of our input data and the output relaxed structure. All three profiles relax to a state that matches the input structure to a high degree. However, it is worth noting that the same entropy profile in *MESA* will result in an entirely different temperature and density profile than *Octo-Tiger* because of the differing EoS and the necessity for HSE in *MESA*. Furthermore, because *MESA* includes radiation effects and tabulated opacity, the relaxed structure is much bigger than the post-merger seen in *Octo-Tiger*. The difference in the density and temperature profiles can be seen in Figure 4.6. As pointed out earlier, the *Octo-Tiger* core does not have a sufficient temperature for He-burning, while the *MESA* profile suggests that the primary should be He-burning. We note that while the post-merger

also has a core that is too cool for He-burning, the structure has not yet settled after being disrupted and the star will begin to contract, making the core hotter.

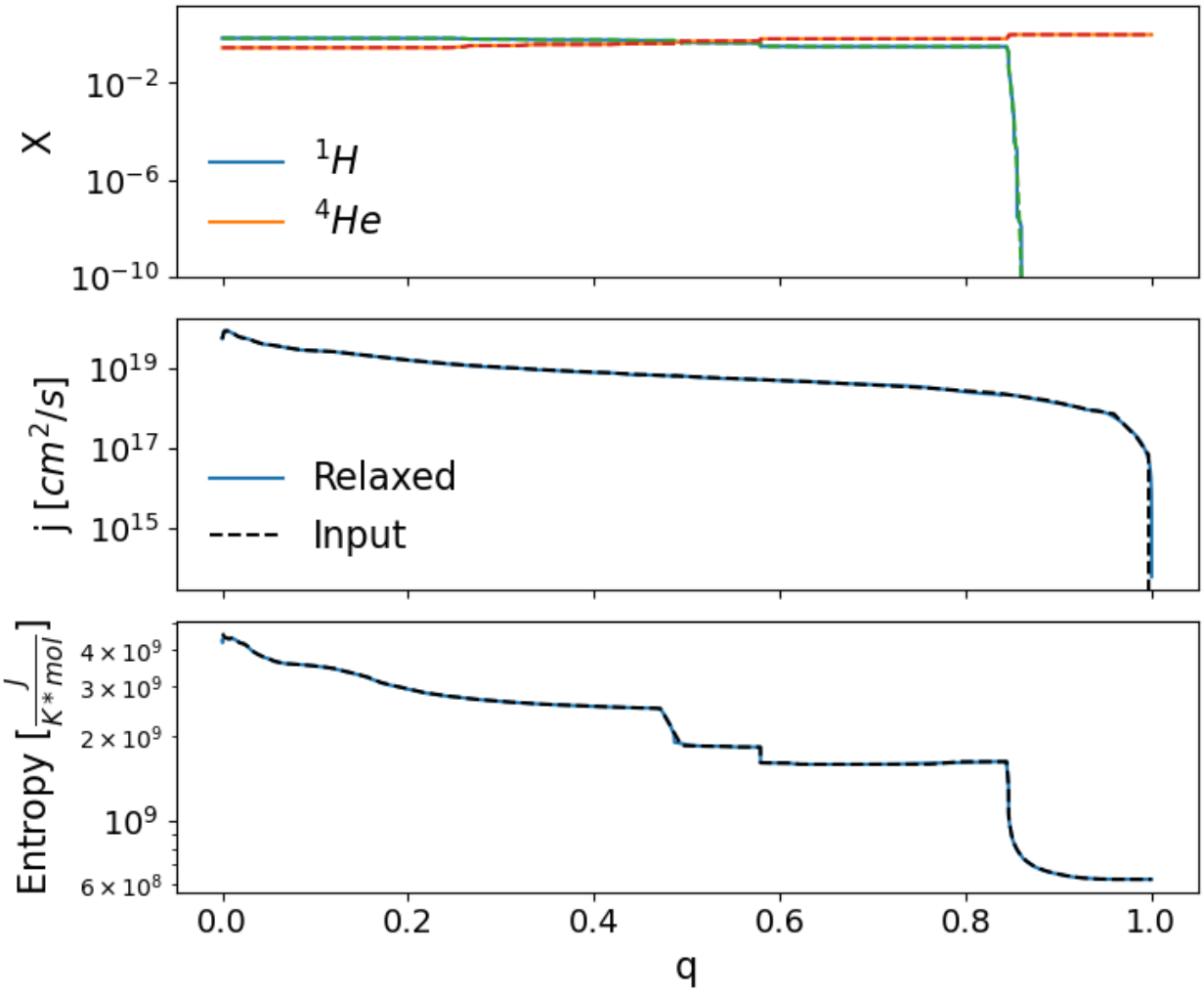

Figure 4.5. A comparison of the input profiles to the output *MESA* relaxed profiles. The dashed lines are the input data and the solid lines are the output data from the relaxation procedure.

4.3 Evolving the Post-Merger

4.3.1 Parameters used for Evolution

After relaxing the post-merger into *MESA*, we allow the star to settle and evolve. During the evolution we use the `Dutch` wind prescription, which uses the `de Jegar` prescription for effective temperatures less than 8000K (de Jager et al., 1988), and the `Vink` wind prescription for higher effective temperatures (Vink et al., 2001). Typically, for non-rotating models, a standard value of the wind scaling factor is 0.8. This could be lower for rotating models so we use a value of 0.4 which is used in the test suite models for rotating stars in *MESA*. Heger

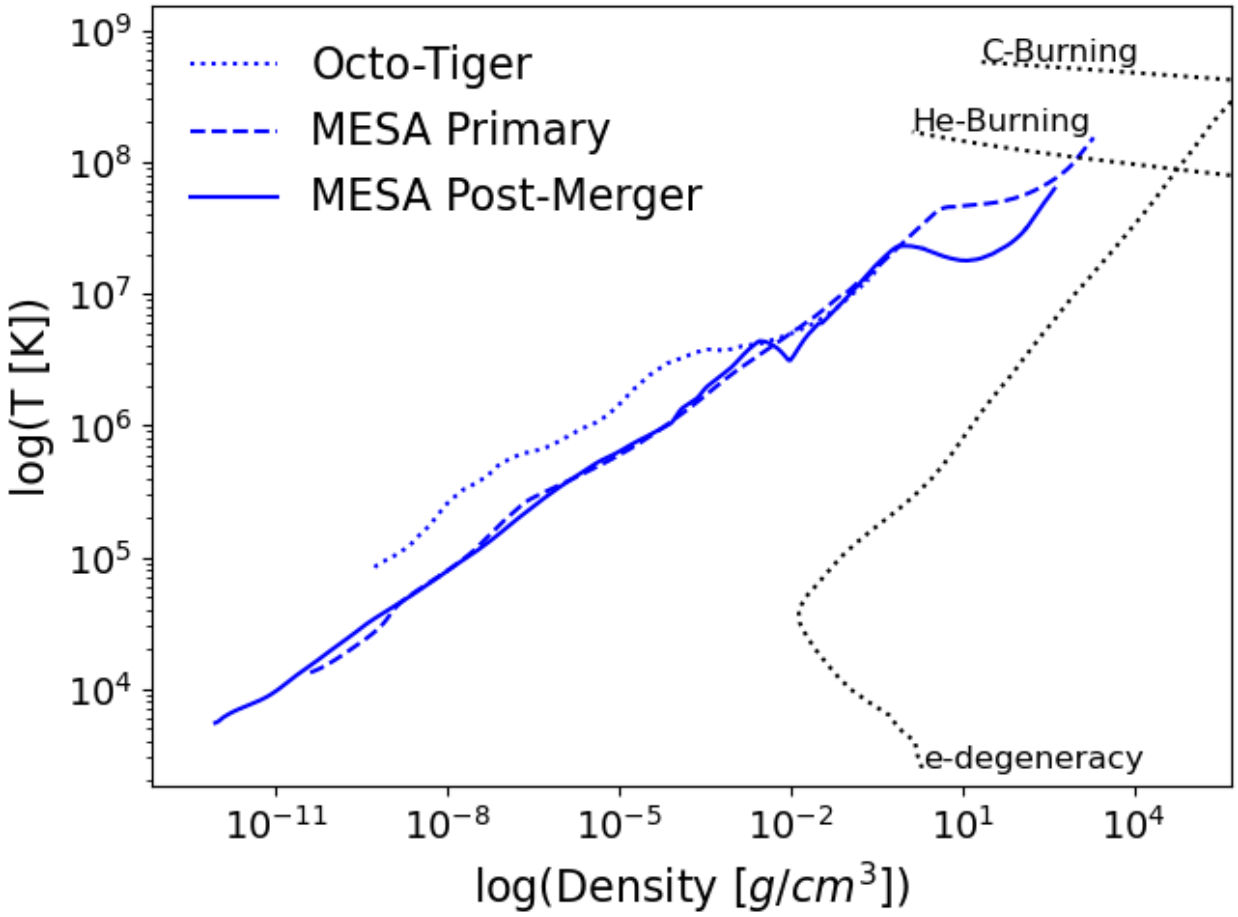

Figure 4.6. A comparison of the density-temperature structure for the *MESA* evolved primary star (dashed blue line), the *Octo-Tiger* evolved post-merger (dotted blue line), and the relaxed object using the *MESA* core entropy and *Octo-Tiger* envelope entropy (solid blue line).

et al. (2000) give an analytical expression for enhanced mass loss due to rotation, which is utilized by default in *MESA* version r21.12.1, of the following form:

$$\dot{M} = \dot{M}_0 \left[\frac{1}{1 - v/v_{crit}} \right]^{\xi} \tag{4.16}$$

Where $\dot{M}_0$ is the mass loss without rotation, v is the surface rotation, v_{crit} is the critical surface rotation, and ξ is the power factor (the default value is 0.43).

Following some of the parameters used for the *MESA* test suite options, we use the `Cox` MLT option (Cox & Giuli, 1968). We include the Ledoux criterion and use a mixing length parameter of 1.6. We also include the effects of semiconvection and thermohaline mixing, but do not focus on overshooting.

Some of the most important set of parameters for this study are the effects of rotationally induced mixing for both chemical mixing and angular momentum diffusion. Because the surface of the star is spun up due to the coalescence of the secondary into the envelope of the

primary, it is important that not too much angular momentum is diffused downward toward the core. The types of rotationally induced mixing we use are Solberg Hoiland (SH), Secular Shear Instability (SSI), Eddington-Sweet Circulation (ES), and Goldreich-Schubert-Fricke Instability (GSF) which are all described in Heger et al. (2000). We also use Spruit-Taylor dynamo action (ST) of Heger et al. (2005) which includes the effects of magnetic fields, but we note that there is a lot of uncertainty regarding the strength and effect of magnetic fields for giant stars. Finally, the overall coefficient which is multiplied by the sum of the diffusion due to all of the above mixing effects is set to 1/30 according to the recommendation of Heger et al. (2000).

4.3.2 Analysis of the Evolution

When evolving the post-merger in *MESA*, we vary the efficiency of rotationally induced diffusion. The reason for this is these effects are inherently 3-dimensional, and their use in *MESA* is based on the work of Heger et al. (2000), who approximated 1D diffusion coefficients for each process. The efficiency factors we vary are used in order to account for the uncertainty of the effectiveness of diffusion for each of these coefficients. This method of simulating mixing is known as the diffusion approximation and Paxton et al. (2013) note that there is another method they refer to as the diffusion-advection approach. While these two methods have nearly identical chemical mixing, the transport of angular momentum can vary significantly. More details regarding this other method of angular momentum diffusion can be found in Maeder & Zahn (1998) and Zahn (1992). A summary of our model parameters, the results, and Betelgeuse observations are shown in Table 4.1.

We find that the parameters that mostly affect the post-merger evolution are the viscosity coefficients from the ST and the ES methods. These methods are dominant in the outer parts of the post-merger star's envelope and can quickly transport excess angular momentum to inner regions thereby significantly slowing-down the equatorial rotation rate of the star. We do, however, have a motivation to assume low efficiency for the ST and ES processes because of the non-spherically symmetric angular momentum deposition during the realistic 3D common envelope phase. High rotation is confined around the equator and not deposited in the high azimuth layers of the model suppressing the efficiency of the ES mechanism. In addition, as we disussed earlier, the driving of angular momentum loss during the merger phase in *Octo-Tiger* may lead to an under-estimate of the actual angular momentum that would have been deposited due to drag forces driving the in-spiraling phase alone. These uncertainties justify our choice of lower efficiencies for the ES, ST mechanisms.

After the relaxation, the post-merger first goes through a contraction phase as it settles from the initial structure of the merger. This contraction phase lasts until the core becomes hot enough for He-burning, on the order of 10^4 years. This is indicated by the dotted line in Figure 4.7. The evolution we are interested in is during the He-burning phase and later, which takes place for another 10^6 years and is indicated by the blue solid line in Figure 4.7. During this phase, the star evolves into the box representing the observed surface temperature and luminosity range of Betelgeuse. This is the phase where we analyze the surface composition and rotation rate.

In order to compare our results to the observations of Betelgeuse, we plot the evolution of the surface composition and velocity and use a box that represents the target values from

Table 4.1. A summary of our model parameters and results for eight different models. BG refers to observed surface values of Betelgeuse taken from Lambert et al. (1984). Columns 2 through 6 are the efficiency factors used for each diffusion mechanism. v_{surf} is the equatorial surface velocity as calculated in *MESA* averaged over the time spent in the HR diagram box. ϵ_i is the surface value of element i calculated with Equation 4.15.

Model	ST	SH	GSF	ES	SSI	v_{surf} (km/s)	ϵ_C	ϵ_N	ϵ_O
1	1	1	1	1	1	0.036	8.48	8.62	8.90
2	0	1	1	1	1	0.29	8.46	8.74	8.89
3	1	1	1	0	1	0.041	8.48	8.63	8.90
4	0.1	1	1	0.1	1	0.063	8.48	8.65	8.90
5	0.01	1	1	0.01	1	0.12	8.48	8.64	8.90
6	0.001	1	1	0.001	1	0.23	8.48	8.65	8.90
7	10^{-7}	1	1	10^{-7}	1	1.9	8.48	8.65	8.90
8	0	1	1	0	1	5.8	8.32	8.55	8.74
BG						5-15	8.25-8.55	8.45-8.75	8.65-8.95

observations. The top and bottom edges of the box represent the range of acceptable values from observations taken from Lambert et al. (1984), while the left and right edges represent the time when the star is in the HR diagram box. Figure 4.8 shows this analysis for Model 1. We can see from the upper left panel that the surface rotational velocity decreases rapidly by nearly three orders of magnitude. The primary reason for such a decrease in surface rotation is the diffusion of angular momentum towards the core. This is supported by Figure 4.9, which shows the diffusion coefficients of Model 1 at the surface during the rapid drop in surface velocity. Furthermore, we see that the strongest contributors are specifically the ST and ES diffusion coefficients with ST being about an order of magnitude stronger. This is further supported by Models 2 and 3 in Table 4.1 by the much larger increase in average surface velocity when ST is turned off compared to when ES is turned off.

After identifying the two biggest contributors to the loss of surface rotation, we ran Models 4-8 in order to explore the effects of decreasing the efficiency of ST and ES diffusion. The results of this experiment are shown in Figure 4.10. We note that while the range of efficiency factors we explored do not have a significant effect on the surface composition, the less efficient diffusion of angular momentum is critical to the evolution of the surface rotation. We find for our models, we do not see a sufficiently fast rotation rate unless the efficiency is reduced by a factor of 10^{-7} or more. We also note that as the efficiency is reduced and angular momentum cannot diffuse towards the core as rapidly, the model becomes more unstable during the contraction phase as shown by the jaggedness of Models 7 and 8 in Figure 4.11.

4.4 Discussion

We present the first models to analyze both the surface composition and rotation rate for Betelgeuse. As is suggested in previous papers, we explore the theory that Betelgeuse is the product of an extreme mass ratio binary merger (Chatzopoulos et al., 2020; Wheeler et al.,

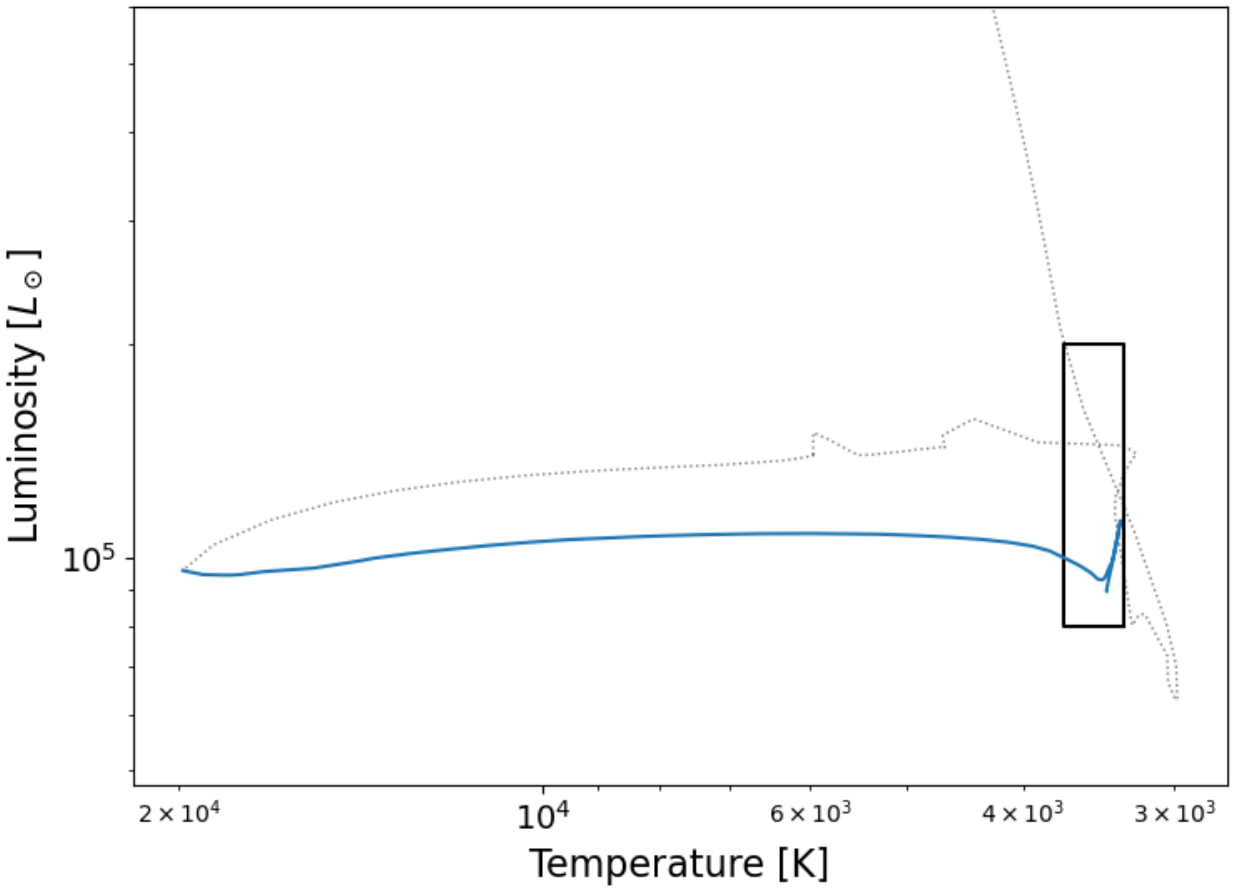

Figure 4.7. An HR diagram for the evolution of Model 1 as defined in Table 4.1. The dotted line indicates the settling phase as the star contracts. He-burning starts on the blue line. The black box represents the observed range of effective temperature and luminosity values for Betelgeuse.

2017). To do this, we map a $16{+}4M_\odot$ merged binary from *Octo-Tiger* into *MESA*. After mapping the post-merger into *MESA*, we perform a series of tests by changing the efficiency of diffusion by ST and ES instabilities.

Of the models we have presented, we find that Models 7 and 8 best agree with the observed surface rotation and composition of Betelgeuse. We note, however, that in order to obtain this agreement, we needed to reduce the efficiency of diffusion due to ST and ES effects at least seven orders of magnitude. We note that the effects and strength of magnetic fields are not well understood for giant stars, and it is uncertain whether or not this efficiency for ST is unreasonable on the surface. Furthermore, the derivations of the diffusion approximation in Heger et al. (2000) were assumed for single rotating stars. In our case, the structure of the primary envelope is perturbed by the coalescence of the secondary and its effect on the efficiency for angular momentum diffusion is unknown.

Future studies could explore the effects of overshooting, as is done in Luo et al. (2022), but with the assumption of a post-merger progenitor. Furthermore, Chatzopoulos et al. (2020) created models with three different mass ratios for their analysis, and it is possible

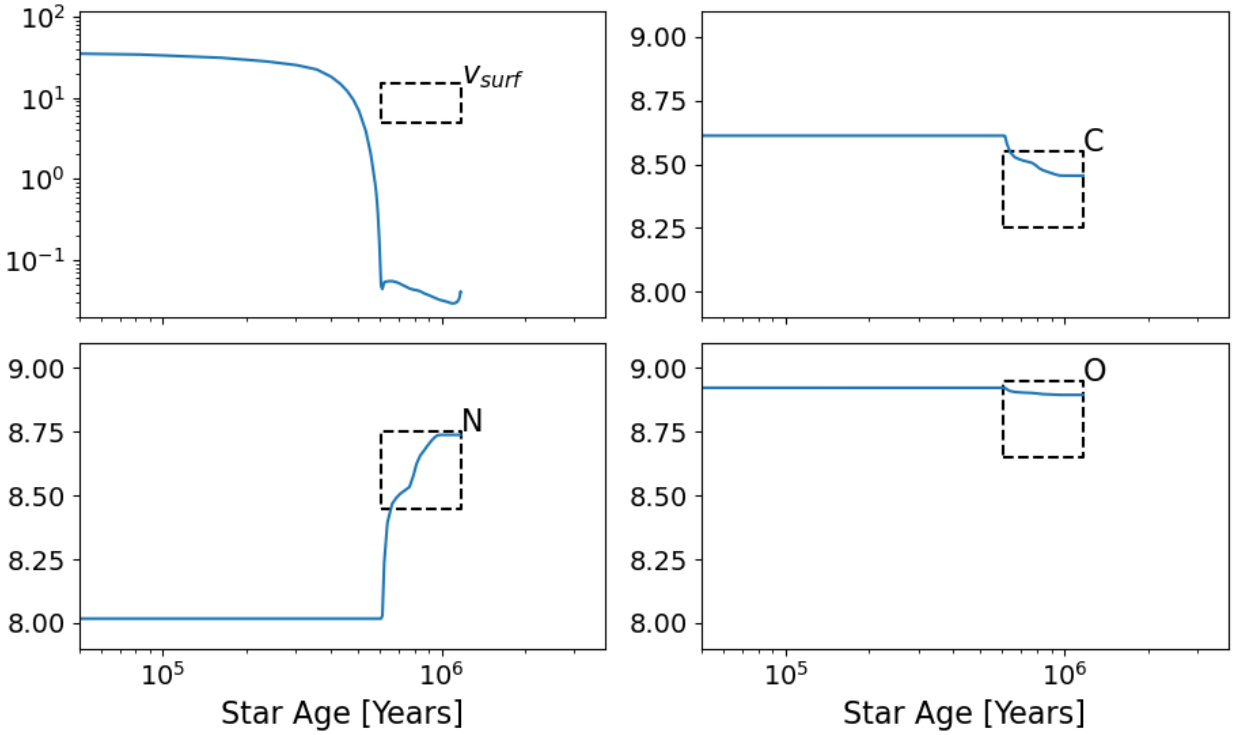

Figure 4.8. The surface values of Model 1 as a function of time. The upper left panel shows the equatorial surface velocity in km/s, the upper right, lower left, and lower right show C, N, and O relative surface abundances computed by Equation 4.15, respectively. The dashed boxes represent the observed values of Betelgeuse (upper and lower edges) and age corresponding to the evolution into the HR box (left and right edges).

that a more extreme mass ratio would have a dramatic effect on our results. Unfortunately, more extreme mass ratios would require a point-mass implementation for the primary core in order to run in a reasonable amount of time in *Octo-Tiger*. This is due to the amount of resolution that would be necessary to sufficiently resolve the compact core without over resolving the envelope.

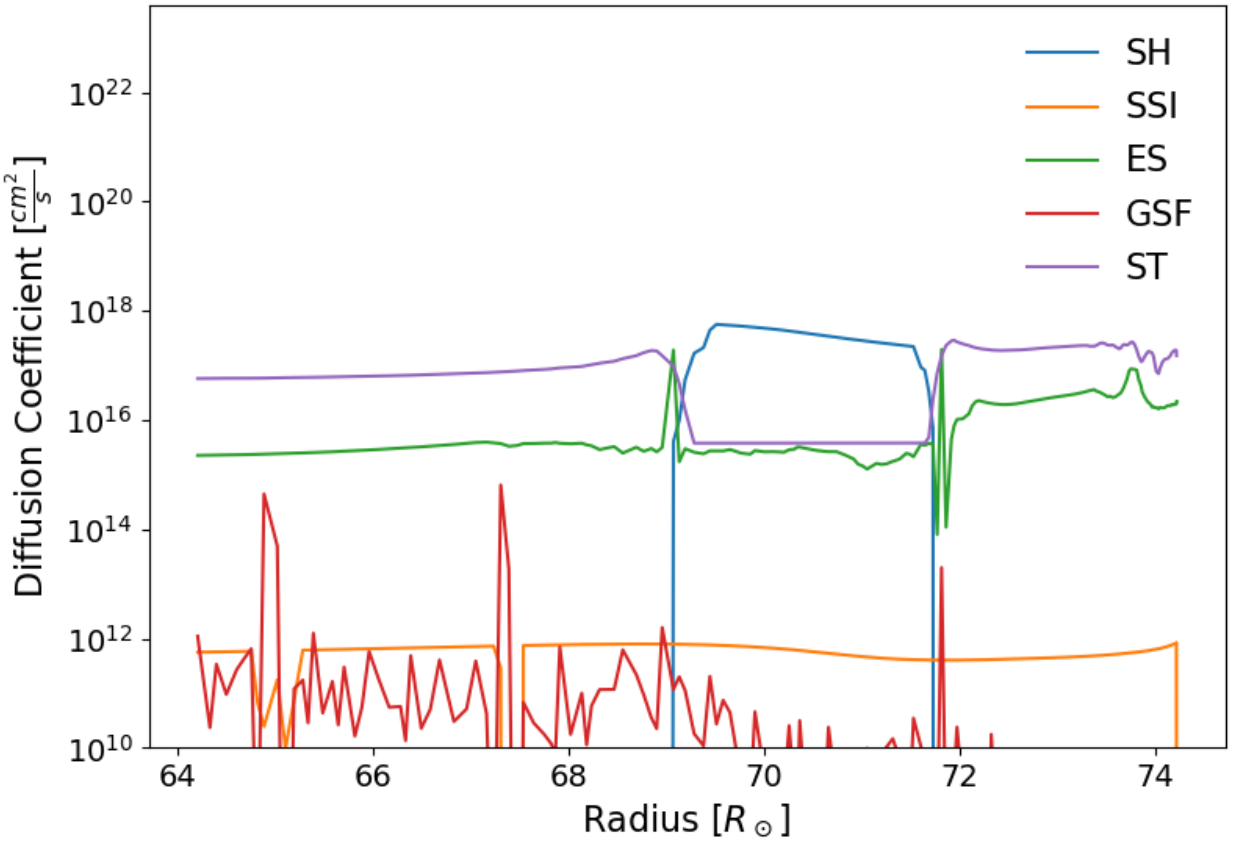

Figure 4.9. A profile of rotationally induced diffusion coefficients for the outer envelope of Model 1. This profile is taken when the surface velocity begins to fall off (around 240,000 years after the merger) and the diffusion coefficients reach a maximum at the surface.

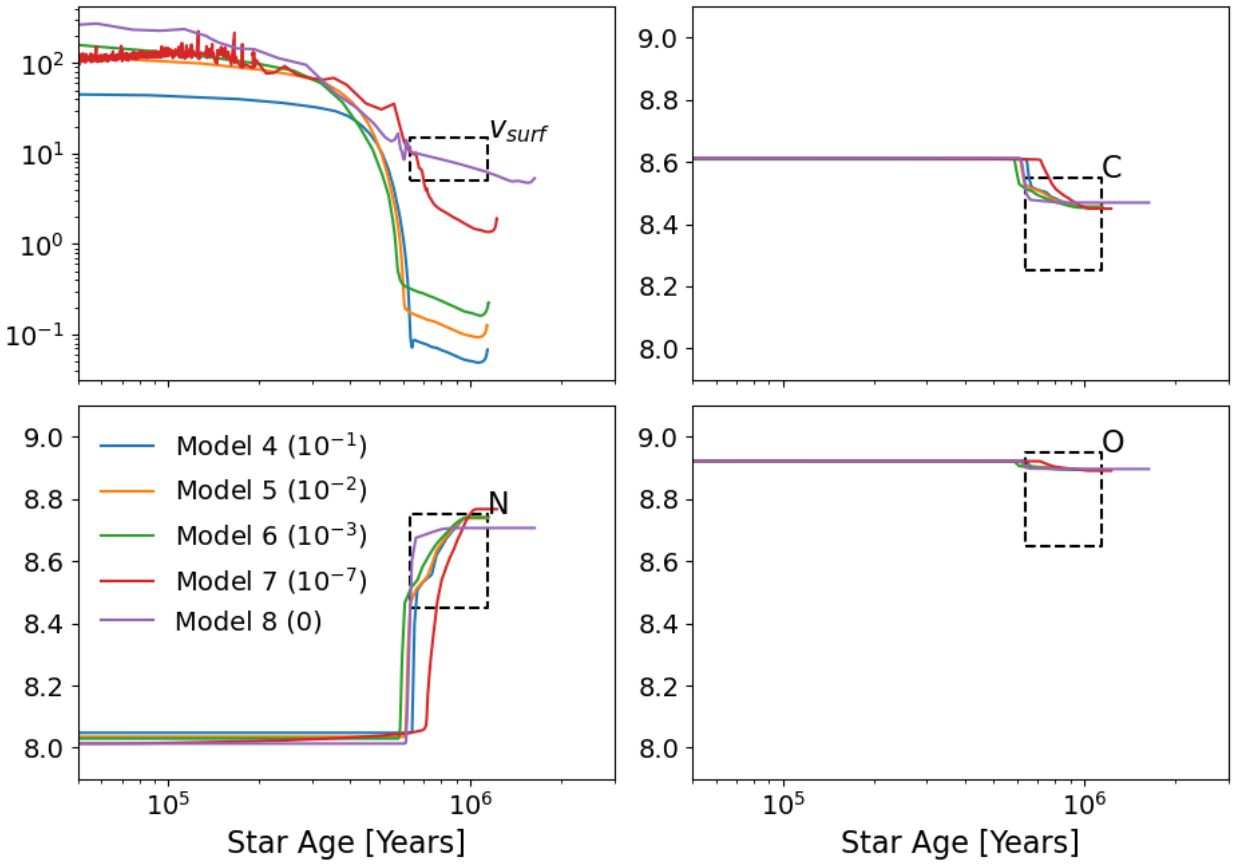

Figure 4.10. The surface values for Models 4-8 with the ST and ES efficiency factors in parentheses. The dashed boxes represent the average range of time that the models are in the box on the HR box and the observations of that parameter for Betelgeuse.

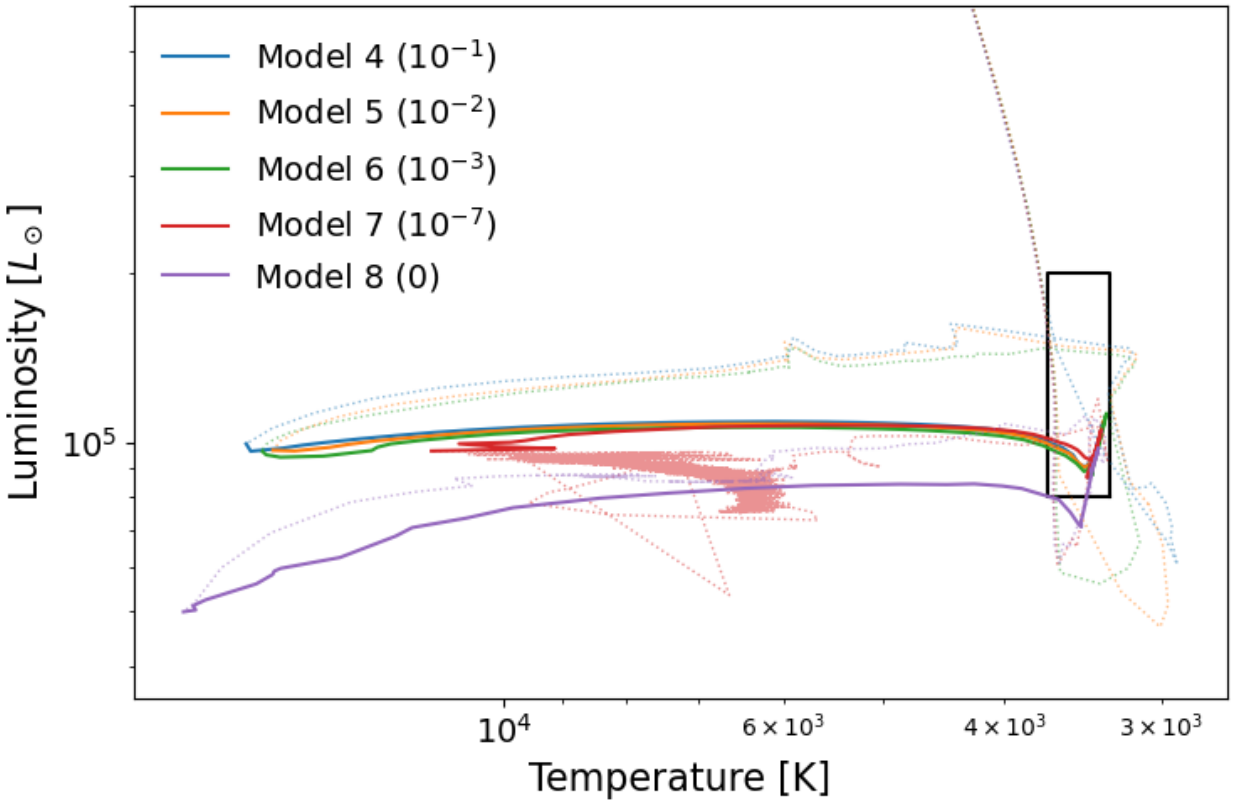

Figure 4.11. The HR diagram for Models 4-8 with ES and ST diffusion coefficients in parentheses, which are set to the same value. The dashed boxes represent the observed values of Betelgeuse (upper and lower edges) and age corresponding to the evolution into the HR box (left and right edges).

CHAPTER 5.
CONCLUSIONS

5.1 Overview

5.1.1 3D to 1D Procedure

Section 3.1 presents the first attempt to reproduce RCB star surface abundances (including s-process elements) starting from a 3D hydrodynamics merger simulation. While this attempt is not complete and negates some potentially important phases of nuclear burning (namely, during the merger process), it establishes a mechanism for bringing models from a 3D merger simulation to a 1D stellar evolution simulation and a full scale 1093 isotope post-processing nuclear network. Our models show strong similarities to the stellar engineering models of Crawford et al. (2020) and Lauer et al. (2019) in terms of evolution, mixing, and most surface abundances. Our models also have difficulties in matching ^{14}N to observations (similar to Crawford et al. (2020)) and generating s-process elements.

Our early stage evolution strongly resembles those of Lauer et al. (2019), Schwab (2019), and Crawford et al. (2020). This is because the stellar engineering process is informed by 3D hydrodynamics models, but does not evolve directly from the results of those models. The differences between those models and the He star model of Weiss (1987) and Menon et al. (2013, 2019) are mostly due to how the initial state of the envelope reacts to the input luminosity of the He-burning shell.

While overshooting was necessary in order to match the isotopic ratios, it is a realistic physical phenomenon expected to occur in stars where convection operates and should be included by default in stellar models. Overshooting was not previously studied in the context of RCB stars, but Stancliffe et al. (2015) use models with parameters in the same range as our overshoot parameters. The parameter space of overshoot coefficients could be further constrained by 3D models with realistic mixing procedures, but the adopted MLT prescription in *MESA* is currently the best available option. We find that, for our mapped models, an overshooting parameter of 0.073 and 0.068 for the solar and sub-solar metallicity models, respectively, yield reasonable agreement to observations and previous studies in surface composition. Lower values tend to increase C/O outside the acceptable range while higher values tend to increase ^{18}O/^{16}O and decrease surface N outside the acceptable range. There are, however, many other parameters to study that will change the surface composition.

This study also explores the effects of changing the initial hydrogen abundance. The initial hydrogen abundance may change based on how much of the hydrogen shell of the He WD progenitor survives during the merger process. While studies such as Staff et al. (2012) or Driebe et al. (1998) constrain the mass of the hydrogen envelope to values much higher than our models, we note that *Octo-tiger* does not perform nucleosynthesis during the dynamical merger phase, which may burn a significant fraction of the initial hydrogen. Of course, with too little initial hydrogen (our sub-solar model, for instance) the He-burning shell cannot create a sustainable ^{13}C neutron source. Additionally, there are common envelope phases before the WD merger that are not simulated in this study but will affect the progenitor composition. The complexities of the complete RCB evolution necessitates a wider parameter space study of the initial post-merger composition. Future studies which pursue the 3D

simulation of the merger being mapped into 1D nuclear lifetime evolutionary codes like *MESA* should include a basic nuclear network that accounts for most pp chain and CNO cycle elements during the merger phase. Being able to trace and burn isotopes during the merger will give improved compositional profiles to be mapped into a 1D evolution code and we demonstrate the necessity of this in Section 3.2.

Section 4.2 demonstrates how we can extend this mapping method to apply outside of just DWD mergers. We show that we are also able to map the merger of a giant and main sequence star in order to reproduce the curious surface parameters seen on Betelgeuse. The possibility for Betelgeuse to be the result of a merger scenario are discussed in previous works such as Wheeler et al. (2017), Chatzopoulos et al. (2020), and Luo et al. (2022) and we are able to support such arguments using our mapping method.

The framework for simulating 3D mergers and their 1D post-merger evolution presented here is a necessary step to perform a full simulation starting from the short timescale dynamical merger to the long timescale thermal and nuclear evolution for many multiple types of merger scenarios.

5.1.2 Stellar Engineering Procedure

Section 3.2 presents a parameter study of RCB models using an improved stellar engineering method first utilized by Lauer et al. (2019). The improvements we make include a smooth core to envelope entropy transition, inclusion of the effects of nucleosynthesis during the merger event, and post-processing with a larger nuclear network for s-process analysis. We use a range of parameters informed by the 3D hydrodynamics model presented in Section 2.1.1 and explore the effects of the steepness of the entropy transition, the shell burning temperature, and overshooting. This method allows for a computationally inexpensive exploration of the associated parameter space and impact on observables without relying on more expensive 3D simulations.

We show the effects of changing the entropy transition and peak temperature independently in our models. Both parameters can increase or decrease the amount of nuclear burning present in the He-burning region. This has noticeable effects on the surface abundances and the final size of the star during the RCB phase. We also find that the inclusion of overshooting in these models does not have a dramatic effect on the surface abundances unless overshooting becomes efficient enough to dredge up material from the CO core.

We find that Model D1 is our optimal model from this parameter study and shows good agreement with observed surface abundances. This model shows a large enhancement in s-process elements and, interestingly, has a neutron exposure and density in the burning region on the level expected for i-process nucleosynthesis (Denissenkov et al., 2018). This level of neutron exposure is necessary because of the convective gap that forms only 20-50 years after the merger event, meaning that neutron capture on heavy elements needs to happen relatively fast to achieve the enhancement seen in observations of RCB surface abundances.

5.2 Future Work

5.2.1 RCB Stars

Although we present a model that has good agreement to all relevant observed surface abundances (Model D1 in Section 3.1), this model is a result of stellar engineering and does not directly utilize the profiles calculated from a spherically averaged 3D hydrodynamics simulation. It remains to be seen if models initialized from the 3D to 1D procedure can also yield results in agreement with observations. Although the 3D models we presented in Chapter 3.2 matched for most surface abundances, we were not able to produce the elevated s-process elements nor the ^{14}N abundance.

The high neutron exposure in Model D1 clearly shows that in order to obtain the level of enhancement of neutron capture elements, one needs a large and steady abundance of ^{13}C neutron source. The only way we are able to achieve such an abundance is by including the effects of nucleosynthesis during the merger. In Section 3.2, this is done via a single zone nucleosynthesis calculation over a short duration in order to mimic the effects of any burning in the SOF during the merger phase. However, if one were to adopt a small nuclear network in *Octo-Tiger*, it is possible to achieve the same goal. Unfortunately, further steps must be taken to reduce the level of diffusion, which is likely overestimated due to the grid-based structure as suggested in Staff et al. (2018). Overall, a more careful analysis of the amount of material dredged up from the CO core is a necessary step in order to limit the amount of core material synthesized in the SOF and brought into the envelope.

Aside from adding a small nuclear network, there are other improvements that could be made to *Octo-Tiger* that may aid in future RCB and general merger studies. As discussed in Section 2.1.1, there is a discrepancy between the EoS used in *Octo-tiger* and *MESA*. *MESA* uses an entire table of different EoS options and uses the appropriate EoS or a blend of two in order to calculate the thermodynamic variables in a cell. This sophistication is not feasible in *Octo-tiger* because of computational constraints when simulating in three dimensions. Instead, it would be more reasonable to utilize one EoS that will be reliable in the regions of the star which are important for our analysis. In the case of RCB progenitors, the Helmholtz EoS would be most appropriate for most of the envelope of the RCB, including the He-burning region (Timmes & Swesty, 2000). Although the difference between this and the ideal gas EoS currently used in *Octo-tiger* may only result in a temperature change of a few factors at most, this will significantly change the nucleosynthesis that occurs within the He-burning region. This implementation may be relatively straightforward to implement into *Octo-tiger* as Timmes & Swesty (2000) have already created open source packages in Fortran that calculate the thermodynamic variables using the Helmholtz EoS.

The other improvement that could be made to *Octo-Tiger* is implementing a mechanism for angular momentum diffusion. As shown in the work of Schwab et al. (2012), it is expected that the post-merger object should become spherical on a timescale of a few hours, but *Octo-tiger* does not currently have a prescription for viscosity. In principle, one could add terms for the shear tensor and a coefficient for shear viscosity to the hydrodynamic equations solved by *Octo-tiger*. A similar implementation is used in the *ZEUS* code of Clarke (2010), but would have to be implemented in a rotating reference frame.

http://cococubed.asu.edu/code_pages/eos.shtml

5.2.2 Extending this Framework

The framework presented thus far has only been utilized in the context of RCB stars and Betelgeuse. However, as it stands, it can also be applied to other low mass degenerate mergers, for instance, CO+CO and He+He WD mergers as well as other mergers between giant and main sequence stars. *Octo-tiger* already contains prescriptions for a bi-polytropic EoS so that giant or main sequence stars where the core and envelope have a differing EoS may be simulated. These types of simulations are important in understanding massive stellar evolution and the origin of extreme circumstellar environments around massive stars. Recent studies have shown that the majority of massive stars are currently, or have been, involved in a binary system (Dunstall et al., 2015). The extension of this framework is a necessary step for understanding how a companion star changes the evolution of massive stars and can be applied to many different kinds of binary mergers.

5.3 Summary and Concluding Thoughts

The framework presented here is a necessary tool for a holistic study of mergers consisting of compact, main sequence and/or giant stars. This includes a simulation of the merger event, a 1D simulation of the long term post-merger evolution and post-processing with an expansive nuclear network to study high mass nucleosynthesis. A framework expanded beyond what is presented in this work would allow for some of the most extensive studies of binary mergers of both similar masses and extreme mass ratios.

In this work, we present the problem of simulating the formation and evolution of RCB stars through many relevant timescales: a dynamical merger, a viscous phase to become spherical, a thermal expansion, and nuclear evolution as well as white dwarf cooling. While the dynamical and viscous phase are short and require multi-dimensional simulations to accurately model the event, the thermal and nuclear timescales are too long to be simulated in multi-dimensional codes. Thus, we demonstrate two techniques to simulate RCB progenitor evolution: a spherical averaging technique to import the 3D hydrodynamics model from *Octo-tiger* into the 1D stellar evolution code, *MESA*, and a stellar engineering technique that solely uses *MESA* in order to "engineer" a structure informed by 3D hydrodynamics results. Post-processing is performed to analyze the surface abundances for comparison against observed RCB stars. *MPPNP* is used to further analyze the heavy element nucleosynthesis including s-process elements. We find we are able to reproduce all of the relevant surface abundances using the stellar engineering method. Although the results of the mapping method do not perfectly match observations, it presents a robust framework which demonstrates key features such as a He-burning shell, partial mixing to the surface, and HR tracks that match approaches done using stellar engineering and other 3D averaged models. Furthermore, we are able to use the 3D to 1D mapping technique to simulate a possible progenitor of the star α Orionis (popularly known as Betelgeuse) by extending the framework to be applied to giant and main sequence mergers.

There are a number of ways in which one can improve upon the *Octo-tiger* code and the initialization of the post-merger models. This includes adding features such as a Helmholtz EoS (which is currently implemented and needs testing), a prescription for viscosity, and a small nuclear network in order to create a more realistic post-merger object. Other ongoing

developments with *Octo-Tiger* are implementing the ability to directly map a star from *MESA*, point-mass implementation to avoid issues of resolution and long compute times, and radiation transport. The presented framework can be further extended to evolve many kinds of post-merger objects. The inclusion of different types of mergers will expand the framework to cover a much wider breadth of mergers and potential outcomes for evolution. Finally, we have experimented with adding in other third-party codes (like SuperNu (Wollaeger et al., 2013)) to this framework to perform radiation transport and calculate pseudo-bolometric lightcurves and spectra from outbursts. This type of extension would allow for comparison of our models directly to observations of lightcurves and spectra for objects of interest.

APPENDIX A.
CONSTRAINT ON RCB PROGENITOR MASS RATIO

We can demonstrate the constraint on the mass ratio by starting with the equation for angular momentum (J) where M_i is the stellar mass, a_i is the distance from the center of mass of the binary to the center of mass of the individual star, and ω is the orbital velocity.

$$J = (M_1 a_1^2 + M_2 a_2^2)\omega \tag{17}$$

We can rewrite a_i in terms of the total separation between the two stars (a) and the masses in the following way:

$$a_1 = a\frac{M_2}{M_1 + M_2} \tag{18}$$

$$a_2 = a\frac{M_1}{M_1 + M_2} \tag{19}$$

Using Kepler's third law (Equation 20) to substitute the angular velocity, we can rewrite Equation 17 into Equation 21 where a is the separation distance.

$$\omega^2 = \frac{a^3}{G(M_1 + M_2)} \tag{20}$$

$$J = M_1 M_2 \sqrt{\frac{Ga}{M_1 + M_2}} \tag{21}$$

Taking a logarithmic time derivative and rearranging Equation 21 yields the following equation:

$$\frac{\dot{a}}{a} = \frac{2\dot{J}}{J} - \frac{2\dot{M}_2}{M_2}(1 - q) \tag{22}$$

In order to shrink the Roche lobe around the donor and initiate mass transfer, the separation must be decreased. According to Equation 22, before the binary is in contact and mass transfer is initiated, angular momentum must be lost in order to decrease the separation. For this system, the dominant mechanism for angular momentum loss will be gravitational radiation which can be expressed in the following way (Landau & Lifshitz, 1967):

$$\begin{aligned}\frac{\dot{J}}{J} &= \frac{-32G^3}{5c^5}\frac{M_1 M_2 (M_1 + M_2)}{a^4} \\ &= -8.32 \times 10^{-10}\left(\frac{M_1}{M_\odot}\right)\left(\frac{M_2}{M_\odot}\right)\left(\frac{M_1 + M_2}{M_\odot}\right)\left(\frac{a}{R_\odot}\right)^{-4}\end{aligned} \tag{23}$$

As the separation of the binary decreases, the Roche lobe around M_2 will also begin to decrease until it is equivalent to the stellar radius. We can estimate the average radius of the Roche lobe with an expression given by Paczyński (1971).

$$\frac{R_{L_2}}{a} = \frac{2}{3^{4/3}} \left[\frac{M_2}{M_1 + M_2} \right]^{1/3} \tag{24}$$

Taking a logarithmic time derivative of Equation 24 yields the following equation:

$$\frac{\dot{R_{L_2}}}{R_{L_2}} - \frac{\dot{a}}{a} = \frac{1}{3} \frac{\dot{M_2}}{M_2} \tag{25}$$

Combining Equations 22 and 25 and rearranging gives us the following expression where $\zeta_L = -2(\frac{5}{6} - q)$ is the response of the Roche lobe to a change in mass:

$$\frac{\dot{R_{L_2}}}{R_{L_2}} = \frac{2\dot{J}}{J} + \zeta_L \frac{\dot{M_2}}{M_2} \tag{26}$$

Looking at Equation 26, one can see that if $q > \frac{5}{6}$, then the Roche lobe will shrink as M_2 loses mass. This means that unless R_2 shrinks faster than the Roche lobe, this process will become dynamically unstable. Therefore, it is important to consider the response of R_2 to mass loss. In fact, the mass-radius relationship for WDs is well known to be $R \propto M^{-1/3}$. Taking the logarithmic time derivative of this relationship yields the following expression:

$$\frac{\dot{R}_2}{R_2} = -\frac{1}{3} \frac{\dot{M}_2}{M_2} + \left(\frac{\dot{R}_2}{R_2} \right)_{nuc} \tag{27}$$

The last term refers to the response of R_2 to nuclear evolution. Finally, if we consider the very moment where M_2 fills its Roche lobe and begins mass transfer, then we know $R_{L_2} \simeq R_2$ and can substitute Equation 27 into Equation 26 and obtain our final expression.

$$\frac{\dot{M}_2}{M_2} = \frac{\frac{2\dot{J}}{J} - \left(\frac{\dot{R}_2}{R_2} \right)_{nuc}}{-\frac{1}{3} - \zeta_L} \tag{28}$$

If we once again consider the Roche lobe response to mass loss (ζ_L), but this time also account for the stellar response to mass loss ($\zeta = -\frac{1}{3}$), we notice that if $\zeta < \zeta_L$, the Roche lobe response to mass loss is faster and will therefore result in a dynamically unstable mass transfer. These considerations lead to a new constraint of $q > 2/3$.

APPENDIX B.
RCB CUSTOM NUCLEAR NETWORK

Table 1. The isotopes in the 40-isotope custom nuclear network used for some models in this work.

1	Neutrons	11	B11	21	O16	31	Ne22
2	H1	12	C11	22	O17	32	Na21
3	H2	13	C12	23	O18	33	Na22
4	He3	14	C13	24	F17	34	Na23
5	He4	15	C14	25	F18	35	Na24
6	Li7	16	N13	26	F19	36	Mg23
7	Be7	17	N14	27	Ne18	37	Mg24
8	Be9	18	N15	28	Ne19	38	Mg25
9	Be10	19	O14	29	Ne20	39	Mg26
10	B8	20	O15	30	Ne21	40	Fe56

APPENDIX C.
COPYRIGHT INFORMATION

Parts of Chapters 2 and 3 were taken and modified from the paper "R Coronae Borealis Star Evolution: Simulating 3D Merger Events to 1D Stellar Evolution Including Large-scale Nucleosynthesis" Munson et al. (2021). The copyright is held by AAS, but reproduction rights are granted to the first author by AAS.

The Astrophysical Journal, 911:103 (15pp), 2021 April 20 https://doi.org/10.3847/1538-4357/abeb6c

CrossMark

R Coronae Borealis Star Evolution: Simulating 3D Merger Events to 1D Stellar Evolution Including Large-scale Nucleosynthesis

Bradley Munson[1], Emmanouil Chatzopoulos[1], Juhan Frank[1], Geoffrey C. Clayton[1], Courtney L. Crawford[1], Pavel A. Denissenkov[2], and Falk Herwig[2]
[1] Dept. of Physics and Astronomy, Louisiana State University, Baton Rouge, LA 70803, USA
[2] Dept. of Physics and Astronomy, University of Victoria, Victoria, BC V8P5C2, Canada
Received 2020 December 11; revised 2021 February 25; accepted 2021 March 1; published 2021 April 22

Abstract

R Coronae Borealis (RCB) stars are rare hydrogen-deficient carbon-rich variable supergiants thought to be the result of dynamically unstable white dwarf mergers. We attempt to model RCB stars through all the relevant timescales by simulating a merger event in *Octo-tiger*, a 3D adaptive mesh refinement (AMR) hydrodynamics code, and mapping the post-merger object into MESA, a 1D stellar evolution code. We then post-process the nucleosynthesis on a much larger nuclear reaction network to study the enhancement of *s*-process elements. We present models that match observations or previous studies in most surface abundances, isotopic ratios, early evolution, and lifetimes. We also observe similar mixing behavior to previous modeling attempts that result in the partial He-burning products visible on the surface in observations. However, we do note that our subsolar models lack any enhancement in *s*-process elements, which we attribute to a lack of hydrogen in the envelope. We also find that the $^{16}O/^{18}O$ isotopic ratio is very sensitive to initial hydrogen abundance and increases outside of the acceptable range with a hydrogen mass fraction greater than 10^{-4}.

Unified Astronomy Thesaurus concepts: Close binary stars (254); Stellar mergers (2157); Stellar evolutionary models (2046); Stellar nucleosynthesis (1616); Hydrodynamics (1963); White dwarf stars (1799); R Coronae Borealis variable stars (1327); Abundance ratios (11)

Figure 1. Snapshot of Munson et al. (2021) Publication used in Chapters 2 and 3.

Figure 2. Snapshot of AAS Author reproduction rights

Parts of Chapters 2 and 3 were taken and modified from the paper "Improved Models of R Coronae Borealis Stars" Munson et al. (2022). This paper is published under open-access and copyright is held by The Author(s).

The Astrophysical Journal, 939:45 (12pp), 2022 November 1 https://doi.org/10.3847/1538-4357/ac9476

Improved Models of R Coronae Borealis Stars

Bradley Munson[1], Emmanouil Chatzopoulos[1,2], and Pavel A. Denissenkov[3,4,5]
[1] Dept. of Physics and Astronomy, Louisiana State University, Baton Rouge, LA 70803, USA; bmunso2@lsu.edu
[2] Institute of Astrophysics, Foundation for Research and Technology-Hellas, 70013, Heraklion, Greece
[3] Department of Physics & Astronomy, University of Victoria, Victoria, BC V8W 2Y2, Canada
[4] Joint Institute for Nuclear Astrophysics, Center for the Evolution of the Elements, Michigan State University, 640 South Shaw Lane, East Lansing, MI 48824, USA
Received 2022 May 20; revised 2022 September 16; accepted 2022 September 21; published 2022 November 2

Abstract

We present an improved numerical method to model subsolar He+CO-WD merger progenitors of R Corona Borealis stars that builds on our previous work. These improvements include a smooth entropy transition from the core to the envelope of the post-merger, inclusion of single-zone nucleosynthesis to mimic the effects of burning during the merger event, and post-processing the models with a larger nuclear network for analysis of *s*-process nucleosynthesis. We perform a parameter study to understand the effects of the entropy transition, peak temperature, and overshooting on our models. The models that best agree with observations of R Corona Borealis stars are processed with a much larger nuclear network to investigate *s*-process nucleosynthesis and the dredge-up of *s*-process products into the outer envelope in detail. We present a model with a significant enhancement in *s*-process elements, which also agrees with observed surface abundances and isotopic ratios of $^{16}O/^{16}O$ and C/O between 1 and 10. Finally, we find that the neutron exposure and initial neutron densities this model requires to obtain such an enhancement are much more consistent with *i*-process nucleosynthesis.

Unified Astronomy Thesaurus concepts: Stellar mergers (2157); Close binary stars (254); Stellar abundances (1577); Stellar evolution (1599); White dwarf stars (1799); Nucleosynthesis (1131)

Figure 3. Snapshot of Munson et al. (2022) Publication used in Chapters 2 and 3.

WORKS CITED

Asplund, M., Gustafsson, B., Lambert, D. L., & Rao, N. K. (2000). The R Coronae Borealis stars - atmospheres and abundances. *A&A*, *353*, 287–310.

Benz, W., Bowers, R. L., Cameron, A. G. W., & Press, W. H. . (1990). Dynamic Mass Exchange in Doubly Degenerate Binaries. I. 0.9 and 1.2 M_{sun} Stars. *ApJ*, *348*, 647.

Chatzopoulos, E. (2020). Is Betelgeuse the Outcome of a Past Merger? In *American Astronomical Society Meeting Abstracts #235*, vol. 235 of *American Astronomical Society Meeting Abstracts*, (p. 131.06).

Chatzopoulos, E., Frank, J., Marcello, D. C., & Clayton, G. C. (2020). Is Betelgeuse the Outcome of a Past Merger? *ApJ*, *896*(1), 50.

Clarke, D. A. (2010). On the Reliability of ZEUS-3D. *ApJS*, *187*(1), 119–134.

Clayton, G. C. (1996). The R Coronae Borealis Stars. *PASP*, *108*, 225.

Clayton, G. C. (2012). What Are the R Coronae Borealis Stars? *Journal of the American Association of Variable Star Observers (JAAVSO)*, *40*(1), 539.

Clayton, G. C., Geballe, T. R., Herwig, F., Fryer, C., & Asplund, M. (2007). Uniquely Large Excesses of 18O in HdC and RCB Stars: Evidence for White Dwarf Mergers. In *Asymmetrical Planetary Nebulae IV*, (p. 83).

Cox, J. P., & Giuli, R. T. (1968). *Principles of stellar structure*. Gordon and Breach.

Crawford, C. L., Clayton, G. C., Munson, B., Chatzopoulos, E., & Frank, J. (2020). Modelling R Coronae Borealis stars: effects of He-burning shell temperature and metallicity. *MNRAS*, *498*(2), 2912–2924.

Dan, M., Rosswog, S., Guillochon, J., & Ramirez-Ruiz, E. (2011). Prelude to A Double Degenerate Merger: The Onset of Mass Transfer and Its Impact on Gravitational Waves and Surface Detonations. *ApJ*, *737*(2), 89.

de Jager, C., Nieuwenhuijzen, H., & van der Hucht, K. A. (1988). Mass loss rates in the Hertzsprung-Russell diagram. *A&AS*, *72*, 259–289.

de Mink, S. E., Sana, H., Langer, N., Izzard, R. G., & Schneider, F. R. N. (2014). The Incidence of Stellar Mergers and Mass Gainers among Massive Stars. *ApJ*, *782*(1), 7.

Denissenkov, P., Perdikakis, G., Herwig, F., Schatz, H., Ritter, C., Pignatari, M., Jones, S., Nikas, S., & Spyrou, A. (2018). The impact of (n, γ) reaction rate uncertainties of unstable isotopes near N = 50 on the i-process nucleosynthesis in He-shell flash white dwarfs. *Journal of Physics G Nuclear Physics*, *45*(5), 055203.

Dolan, M. M., Mathews, G. J., Lam, D. D., Quynh Lan, N., Herczeg, G. J., & Dearborn, D. S. P. (2016). Evolutionary Tracks for Betelgeuse. *ApJ*, *819*(1), 7.

Driebe, T., Schoenberner, D., Bloecker, T., & Herwig, F. (1998). The evolution of helium white dwarfs. I. The companion of the millisecond pulsar PSR J1012+5307. *A&A*, *339*, 123–133.

Dunstall, P. R., Dufton, P. L., Sana, H., Evans, C. J., Howarth, I. D., Simón-Díaz, S., de Mink, S. E., Langer, N., Maíz Apellániz, J., & Taylor, W. D. (2015). The VLT-FLAMES Tarantula Survey. XXII. Multiplicity properties of the B-type stars. *A&A*, *580*, A93.

Endal, A. S., & Sofia, S. (1976). The evolution of rotating stars. I. Method and exploratory calculations for a 7 M sun star. *ApJ*, *210*, 184–198.

Frank, J., King, A., & Raine, D. (2002). *Accretion Power in Astrophysics*. The Edinburgh Building, Cambridge, United Kingdom: Cambridge University Press, third ed.

Fujimoto, M. Y. (1977). On the Origin of R-Type Carbon Stars: Possibility of Hydrogen Mixing during Helium Flicker. *PASJ*, *29*, 331–350.

Gilliland, R. L., & Dupree, A. K. (1996). First Image of the Surface of a Star with the Hubble Space Telescope. *ApJL*, *463*, L29.

Godwin, H. (1962). Half-life of Radiocarbon. *Nature*, *195*(4845), 984.

Grevesse, N., & Sauval, A. J. (1998). Standard Solar Composition. *SSRv*, *85*, 161–174.

Guerrero, J., García-Berro, E., & Isern, J. (2004). Smoothed Particle Hydrodynamics simulations of merging white dwarfs. *A&A*, *413*, 257–272.

Heger, A., Langer, N., & Woosley, S. E. (2000). Presupernova Evolution of Rotating Massive Stars. I. Numerical Method and Evolution of the Internal Stellar Structure. *ApJ*, *528*(1), 368–396.

Heger, A., Woosley, S. E., & Spruit, H. C. (2005). Presupernova Evolution of Differentially Rotating Massive Stars Including Magnetic Fields. *ApJ*, *626*(1), 350–363.

Herwig, F., Diehl, S., Fryer, C. L., Hirschi, R., Hungerford, A., Magkotsios, G., Pignatari, M., Rockefeller, G., Timmes, F. X., Young, P., & Bennet, M. E. (2008). Nucleosynthesis simulations for a wide range of nuclear production sites from NuGrid. In *Nuclei in the Cosmos (NIC X)*, (p. E23).

Herwig, F., Langer, N., & Lugaro, M. (2003). The s-Process in Rotating Asymptotic Giant Branch Stars. *ApJ*, *593*(2), 1056–1073.

Iben, J., Icko (1990). On the Consequences of Low-Mass White Dwarf Mergers. *ApJ*, *353*, 215.

Jeffery, C. S., Karakas, A. I., & Saio, H. (2011). Double white dwarf mergers and elemental surface abundances in extreme helium and R Coronae Borealis stars. *MNRAS*, *414*(4), 3599–3616.

Käppeler, F., Gallino, R., Bisterzo, S., & Aoki, W. (2011). The s process: Nuclear physics, stellar models, and observations. *Reviews of Modern Physics*, *83*(1), 157–194.

Lambert, D. L., Brown, J. A., Hinkle, K. H., & Johnson, H. R. (1984). Carbon, nitrogen and oxygen abundances in Betelgeuse. *ApJ*, *284*, 223–237.

Landau, L. D., & Lifshitz, E. M. (1967). *The Classical Theory of Fields*. Headington Hill Hall, Oxford: Pergamon Press, third ed.

Lauer, A., Chatzopoulos, E., Clayton, G. C., Frank, J., & Marcello, D. C. (2019). Evolving R Coronae Borealis stars with MESA. *MNRAS*, *488*(1), 438–450.

Lodders, K. (2003). Solar System Abundances and Condensation Temperatures of the Elements. *ApJ*, *591*(2), 1220–1247.

Longland, R., Lorén-Aguilar, P., José, J., García-Berro, E., Althaus, L. G., & Isern, J. (2011). Nucleosynthesis during the Merger of White Dwarfs and the Origin of R Coronae Borealis Stars. *ApJL*, *737*(2), L34.

Lorén-Aguilar, P., Isern, J., & García-Berro, E. (2009). High-resolution smoothed particle hydrodynamics simulations of the merger of binary white dwarfs. *A&A*, *500*(3), 1193–1205.

Lorén-Aguilar, P., Isern, J., & García-Berro, E. (2010). Smoothed particle hydrodynamics simulations of white dwarf collisions and close encounters. *MNRAS*, *406*(4), 2749–2763.

Loreta, E. (1935). Nota sulle stelle variabili R Coronidi. *Astronomische Nachrichten*, *254*, 151.

Luo, T., Umeda, H., Yoshida, T., & Takahashi, K. (2022). Stellar Models of Betelgeuse Constrained Using Observed Surface Conditions. *ApJ*, *927*(1), 115.

Maeder, A., & Zahn, J.-P. (1998). Stellar evolution with rotation. III. Meridional circulation with MU -gradients and non-stationarity. *A&A*, *334*, 1000–1006.

Marcello, D., Kadam, K., Clayton, G. C., Frank, J., Kaisar, H., & Motl, P. (2016). Introducing Octo-tiger/HPX: Simulating Interacting Binaries with Adaptive Mesh Refinement and the Fast Multipole Method. In *Accretion Processes in Cosmic Sources*, (p. 55).

Menon, A., Herwig, F., Denissenkov, P. A., Clayton, G. C., Staff, J., Pignatari, M., & Paxton, B. (2013). Reproducing the Observed Abundances in RCB and HdC Stars with Post-double-degenerate Merger Models—Constraints on Merger and Post-merger Simulations and Physics Processes. *ApJ*, *772*(1), 59.

Menon, A., Karakas, A. I., Lugaro, M., Doherty, C. L., & Ritter, C. (2019). Low-metallicity CO + He WD post-merger models for RCB stars as a source of pre-solar graphite grains. *MNRAS*, *482*(2), 2320–2335.

Munson, B., Chatzopoulos, E., & Denissenkov, P. A. (2022). Improved Models of R Coronae Borealis Stars. *ApJ*, *939*(1), 45.

Munson, B., Chatzopoulos, E., Frank, J., Clayton, G. C., Crawford, C. L., Denissenkov, P. A., & Herwig, F. (2021). R Coronae Borealis Star Evolution: Simulating 3D Merger Events to 1D Stellar Evolution Including Large-scale Nucleosynthesis. *ApJ*, *911*(2), 103.

O'Keefe, J. A. (1939). Remarks on Loreta's Hypothesis Concerning R Coronae Borealis. *ApJ*, *90*, 294.

Paczyński, B. (1971). Evolutionary Processes in Close Binary Systems. *ARA&A*, *9*, 183.

Paxton, B., Bildsten, L., Dotter, A., Herwig, F., Lesaffre, P., & Timmes, F. (2011). Modules for Experiments in Stellar Astrophysics (MESA). *ApJS*, *192*, 3.

Paxton, B., Cantiello, M., Arras, P., Bildsten, L., Brown, E. F., Dotter, A., Mankovich, C., Montgomery, M. H., Stello, D., Timmes, F. X., & Townsend, R. (2013). Modules for Experiments in Stellar Astrophysics (MESA): Planets, Oscillations, Rotation, and Massive Stars. *ApJS*, *208*, 4.

Paxton, B., Marchant, P., Schwab, J., Bauer, E. B., Bildsten, L., Cantiello, M., Dessart, L., Farmer, R., Hu, H., Langer, N., Townsend, R. H. D., Townsley, D. M., & Timmes, F. X. (2015). Modules for Experiments in Stellar Astrophysics (MESA): Binaries, Pulsations, and Explosions. *ApJS*, *220*, 15.

Paxton, B., Schwab, J., Bauer, E. B., Bildsten, L., Blinnikov, S., Duffell, P., Farmer, R., Goldberg, J. A., Marchant, P., Sorokina, E., Thoul, A., Townsend, R. H. D., & Timmes, F. X. (2018). Modules for Experiments in Stellar Astrophysics (MESA): Convective Boundaries, Element Diffusion, and Massive Star Explosions. *ApJS*, *234*, 34.

Paxton, B., Smolec, R., Schwab, J., Gautschy, A., Bildsten, L., Cantiello, M., Dotter, A., Farmer, R., Goldberg, J. A., Jermyn, A. S., Kanbur, S. M., Marchant, P., Thoul, A., Townsend, R. H. D., Wolf, W. M., Zhang, M., & Timmes, F. X. (2019). Modules for Experiments in Stellar Astrophysics (MESA): Pulsating Variable Stars, Rotation, Convective Boundaries, and Energy Conservation. *ApJS*, *243*(1), 10.

Pigott, E., & Englefield, H. C. (1797). On the Periodical Changes of Brightness of Two Fixed Stars. By Edward Pigott, Esq. Communicated by Sir Henry C. Englefield, Bart. F. R. S. *Philosophical Transactions of the Royal Society of London Series I*, *87*, 133–141.

Schwab, J. (2019). Evolutionary Models for R Coronae Borealis Stars. *ApJ*, *885*(1), 27.

Schwab, J. (2021). Evolutionary Models for the Remnant of the Merger of Two Carbon-Oxygen Core White Dwarfs. *ApJ*, *906*(1), 53.

Schwab, J., Shen, K. J., Quataert, E., Dan, M., & Rosswog, S. (2012). The viscous evolution of white dwarf merger remnants. *MNRAS*, *427*(1), 190–203.

Shen, K. J., Bildsten, L., Kasen, D., & Quataert, E. (2012). The Long-term Evolution of Double White Dwarf Mergers. *ApJ*, *748*(1), 35.

Staff, J. E., Menon, A., Herwig, F., Even, W., Fryer, C. L., Motl, P. M., Geballe, T., Pignatari, M., Clayton, G. C., & Tohline, J. E. (2012). Do R Coronae Borealis Stars Form from Double White Dwarf Mergers? *ApJ*, *757*(1), 76.

Staff, J. E., Wiggins, B., Marcello, D., Motl, P. M., Even, W., Fryer, C. L., Raskin, C., Clayton, G. C., & Frank, J. (2018). The Role of Dredge-up in Double White Dwarf Mergers. *ApJ*, *862*(1), 74.

Stancliffe, R. J., Fossati, L., Passy, J. C., & Schneider, F. R. N. (2015). Confronting uncertainties in stellar physics: calibrating convective overshooting with eclipsing binaries. *A&A*, *575*, A117.

Timmes, F. X., & Swesty, F. D. (2000). The Accuracy, Consistency, and Speed of an Electron-Positron Equation of State Based on Table Interpolation of the Helmholtz Free Energy. *ApJS*, *126*(2), 501–516.

Tisserand, P., Wood, P. R., Marquette, J. B., Afonso, C., Albert, J. N., Andersen, J., Ansari, R., Aubourg, É., Bareyre, P., Beaulieu, J. P., Charlot, X., Coutures, C., Ferlet, R., Fouqué, P., Glicenstein, J. F., Goldman, B., Gould, A., Gros, M., de Kat, J., Lesquoy, É., Loup, C., Magneville, C., Maurice, É., Maury, A., Milsztajn, A., Moniez, M., Palanque-Delabrouille, N., Perdereau, O., Rich, J., Schwemling, P., Spiro, M., & Vidal-Madjar, A. (2009). New Magellanic Cloud R Coronae Borealis and DY Persei type stars from the EROS-2 database: the connection between RCBs, DYPers, and ordinary carbon stars. *A&A*, *501*(3), 985–998.

Tisserand, P., Wyrzykowski, L., Wood, P. R., Udalski, A., Szymański, M. K., Kubiak, M., Pietrzyński, G., Soszyński, I., Szewczyk, O., Ulaczyk, K., & Poleski, R. (2011). New R Coronae Borealis stars discovered in OGLE-III Galactic bulge fields from their mid- and near-infrared properties. *A&A*, *529*, A118.

Uitenbroek, H., Dupree, A. K., & Gilliland, R. L. (1998). Spatially Resolved Hubble Space Telescope Spectra of the Chromosphere of alpha Orionis. *AJ*, *116*(5), 2501–2512.

Vink, J. S., de Koter, A., & Lamers, H. J. G. L. M. (2001). Mass-loss predictions for O and B stars as a function of metallicity. *A&A*, *369*, 574–588.

Webbink, R. F. (1984). Double white dwarfs as progenitors of R Coronae Borealis stars and type I supernovae. *ApJ*, *277*, 355–360.

Weiss, A. (1987). Evolutionary models for R CrB stars. *A&A*, *185*, 165–177.

Wheeler, J. C., Nance, S., Diaz, M., Smith, S. G., Hickey, J., Zhou, L., Koutoulaki, M., Sullivan, J. M., & Fowler, J. M. (2017). The Betelgeuse Project: constraints from rotation. *MNRAS*, *465*(3), 2654–2661.

Wollaeger, R. T., van Rossum, D. R., Graziani, C., Couch, S. M., Jordan, I., George C., Lamb, D. Q., & Moses, G. A. (2013). Radiation Transport for Explosive Outflows: A Multigroup Hybrid Monte Carlo Method. *ApJS*, *209*(2), 36.

Zahn, J. P. (1992). Circulation and turbulence in rotating stars. *A&A*, *265*, 115–132.

Zhang, X., Jeffery, C. S., Chen, X., & Han, Z. (2014). Post-merger evolution of carbon-oxygen + helium white dwarf binaries and the origin of R Coronae Borealis and extreme helium stars. *MNRAS*, *445*(1), 660–673.

VITA

Bradley Munson grew up in Lindenhurst, Illinois and attended Grayslake North High School where he was first exposed to physics and developed an interest in the field. He received his Bachelor's degree in physics in 2017 from North Central College, where he did a number of research projects including constructing a small radio telescope and creating an economic model of small modular reactors, which eventually turned into a thesis for the honors program. He then attended Louisiana State University for his doctoral program where he did research in computational modeling of binary stars and the evolution of resulting post-merger objects. He expects to graduate in May of 2023 and then work for White Sands Missile Range as part of the DOD sponsored SMART program.